Dissertation

submitted to the

Combined Faculty of Natural Sciences and Mathematics

of the Ruperto Carola University Heidelberg, Germany

for the degree of

Doctor of Natural Sciences

Presented by

M.Sc. Andre Schwarz

born in: Villingen-Schwenningen, Germany

Oral examination: 13.05.2020

nucleoporin mRNA localization and Annulate Lamellae biosynthesis during *Drosophila melanogaster* oogenesis

Referees: Dr. Judith Zaugg

Prof. Dr. Bernd Bukau

Acknowledgement

First and foremost I want to thank Martin Beck for agreeing to supervise me throughout my PhD. He is a fantastic scientist with a sharp mind and infectious curiosity, and he instills confidence in the people he interacts with. I learned an immeasurable amount from him and am definitely a different person because of it. Plus he is actually quite a funny person to be around. I also want to thank my co-author throughout this work, Bernhard Hampölz, for teaching me a tremendous amount about cell biology and overall scientific thinking. Without him this work would look much different today. Likewise I would thank Paolo Ronchi for all the work he did with me on this and other projects, and for being a fun conversation partner. Particularly during the start, Imre Gáspár was absolutely instrumental in introducing me to smFISH and by teaching me both probe synthesis and image processing, and I would like to express my gratitude for that to him as well. I also want to thank Dimitri Kromm for trying out my egg chambers on his lightsheet microscope with me.

My thanks extends to past and present members of the Beck Laboratory for helpful input, particularly my former student Marta Kubanska for a lot of work on projects not covered in this thesis, and Shyamal Mosalaganti for the same reason, and for numerous coffee and pool breaks that made life at EMBL much mure fun. The overall scientific environment at EMBL is something I could've only dreamed of and that I will miss dearly.

Finally I want to thank Friedhilde and Armin Schwarz for continuous support in whatever I wanted to pursue in life and for always being available, even on short notice.

Thank you all!

Abstract

Nuclear pore complexes (NPCs) are large protein assemblies that connect the eukaryotic nucleus with the cytoplasm, thus facilitating all transport between them. Besides the nuclear envelope (NE), NPCs also occur in parallel stacks of cytoplasmic membranes called Annulate Lamellae (AL) that can serve as storage, facilitating rapid nuclear growth via NE insertion during fruit fly embryogenesis. How and when AL are assembled is largely unknown. In this work, I established that AL are already abundant in late stage oocytes, and progressively accumulate throughout oogenesis specifically in the oocyte. By screening the localization of 39 *nucleoporin* and related mRNAs, I detected the specific enrichment of two *nucleoporin* and three *importin* encoding transcripts to AL, the NE, and previously unidentified nucleoporin granules throughout the egg chamber. Perturbation experiments revealed a dependence on active translation, but independence of an intact microtubule network on mRNA localization. Generation of *GFP::Nup358* transgenic flies revealed granules with distinct partial nucleoporin contents, that are subject to microtubule-dependent transport and interactions among them. Their spatiotemporal abundance distribution is indicative of NPC precursors, and they contain partial accumulations of pore complexes within internal membranes. These granules further displayed characteristics of biomolecular condensates, including fast intra-granule dynamics, exclusion of cytoplasmic constituents, and sensitivity to 1,6-hexanediol. Both condensation state and AL assembly were dependent on Ran, a protein also fundamental for NPC assembly at the NE. Its nucleotide status throughout this is likely controlled by differential localization of its modulators RanGAP and Rcc1 to granules and cytoplasm respectively. This work thus established a molecular framework and basic sequence of events that leads to the assembly of AL, which are crucial during early development, and might have broader implications for NPC assembly also at the NE.

Zusammenfassung

Kernporen sind große Proteinkomplexe die den eukaryotischen Zellkern mit dem Zytoplasma verbinden und dadurch sämtlichen Transport dazwischen ermöglichen. Neben der Kernhülle weisen auch gewisse parallele Membranstapel Kernporen auf, die als Annulate Lamellae (AL) bezeichnet werden und als Speicher dienen. Indem sie in die Kernmembran eingebaut werden, ermöglichen diese das schnelle Kernwachstum während der Embryogenese von Fruchtfliegen. Wie und wann AL aufgebaut werden ist nicht genau bekannt. In dieser Arbeit zeige ich, dass AL bereits in späten Oocyten in großer Menge vorhanden sind und sich während der Oogenese speziell in der Oocyte zunehmend anreichern. Durch die Überprüfung von 39 *nukleoporin* und verwandten mRNAs konnte ich die spezifische Anreicherung von zwei *nukleoporin-* und drei *importin-*codierenden Transkripten um AL, die Kernhülle, und um zuvor nicht indentifizierte Nukleoporin-Körnchen nachweisen. Dies konnte in der gesamten Eikammer beobachtet werden. Weitere Untersuchungen zeigten, dass die mRNA-Anreicherung abhängig von aktiver Translation war, aber unabhängig von einem intakten Mikrotubuli-Netzwerk. Experimente mit Fliegen mit dem Transgen *GFP::Nup358* offenbarten Körnchen mit verschiedenen Anteilen von Nukleoporinen, die Mikrotubuli-abhängigem Transport und gegenseitigen Interaktionen unterlagen. Ihre zeitliche und räumliche Mengenverteilung wies darauf hin, dass es sich bei ihnen um Kernporenvorläufer handelt. Diese beinhalteten teilweise Anhäufungen von Poren in internen Membranen. Die Körnchen zeigten weiterhin charakteristische Anzeichen von biomolekularen Kondensaten, inklusive schneller Dynamik innerhalb der Körnchen, dem Ausschluss von cytoplasmatischen Bestandteilen, sowie Sensitivität gegenüber 1,6-Hexandiol. Sowohl der Kondensationsstatus, als auch der Aufbau von AL waren abhängig von Ran, einem Protein was auch fundamental im Kernporenaufbau an der Kernhülle ist. Sein Nukleotidstatus wird dabei wahrscheinlich durch seine Modulatoren RanGAP und Rcc1 kontrolliert, die an Körnchen, beziehungsweise im Cytosol sitzen. Diese Arbeit hat einen

molekularen Rahmen sowie eine grundlegende Abfolge etabliert die zum Aufbau von AL führen, welche bedeutend für die frühe Entwicklusmng sind, und darüber hinaus umfassendere Implikationen auch für den Kernporenaufbau an der Kernhülle hat.

List of Abbreviations

NPC	Nuclear Pore Complex
AL	Annulate Lamellum (/Lamellae)
D.m.	*Drosophila melanogaster*
NE	Nuclear Envelope
CR	Cytoplasmic Ring
IR	Inner Ring
NR	Nucleoplasmic Ring
SLiM	Short Linear Motif
WGA	Wheat Germ Agglutinin
NTR	Nuclear Transport Receptor
LLPS	Liquid-Liquid Phase Separation
IDP	Intrinsically Disordered Protein
RBD	RNA-Binding Domain
MT	Microtubule
GEF	Guanine Nucleotide Exchange Factor
GAP	GTPase Activating Protein
NLS	Nuclear Localization Signal
IBB	Importin ß Binding Domain
NES	Nuclear Export Signal
PP1	Protein Phosphatase 1
ER	Endoplasmic Reticulum

INM	Inner Nuclear Membrane
ONM	Outer Nuclear Membrane
ALPC	Annulate Lamellae Nuclear Pore Complex
EM	Electron Microscopy
CLEM	Correlative Light and Electron Microscopy
ISH	*In Situ* Hybridization
RBP	RNA-Binding Protein
RNP	Ribonucleoprotein Complex
RNC	Ribosome-Nascent Chain complex
rER	rough Endoplasmic Reticulum
SRP	Signal Recognition Particle
ATI	A-Type Inclusions
PCM	Pericentriolar Matrix
CDS	(Protein) Coding Sequence
UTR	Untranslated Region
EMCF	EMBL Electron Microscopy Core Facility
TEM	Transmission Electron Microscopy
FIB-SEM	Focused Ion Beam milling and Scanning Electron Microscopy
smFISH	single molecule Fluorescence *In Situ* Hybridization
CHX	Cycloheximide
HHT	Homoharringtonine

STED	Stimulated Emission Depletion (Microscopy)
N.D.	Not Defined
SPIM	Selective Plane Illumination Microscopy

Table of contents

1 Introduction

All life identified so far consists of cells. Named after their superficial resemblance to small monastic chambers [1], they essentially constitute small, enclosed reaction vessels that allow reactions to occur outside a global equilibrium [2]. Within, molecules are transported from one place to another, pumped across a gradient or membrane, chemicals converted, and polymers assembled [3]. The little 'machines' that perform all these tasks are overwhelmingly composed of strings of amino acids called proteins. For proteins, function generally follows form. Coordinating the right set of amino acid side chains in space allows the formation of specific interfaces and pockets to perform the function they are intended to. But proteins don't always work as single entities. Analogous to human-made machines, proteins are often merely parts – like valves and pistons that constitute a motor – that have to come together in a precise spatiotemporal order to form functional groups, or complexes. This modularity has many proposed advantages including more genetic and functional flexibility and structural stability [4]. But dividing large molecular machines into individual smaller subunits also comes with the cost of assembly, a non-trivial process that led to the evolution of an elaborate cellular assembly system [5].

In this chapter I will introduce one of the largest such protein complexes known to date, the Nuclear Pore Complex (NPC), and discuss our current understanding of its architecture, function, and assembly. I will further describe a special NPC-containing organelle that consists of cytoplasmic membrane stacks called Annulate Lamellae (AL). Finally I will introduce the concept of RNA localization and how it might contribute to efficient protein complex assembly, what we currently understand about its mechanisms, and describe a cellular system where all these aspects are of particular importance: The early development of the fruit fly *Drosophila melanogaster (D.m.)*.

1.1 The Nuclear Pore Complex

With a mass of ~110 MDa [6,7], the NPC is certainly amongst the largest protein complexes within eukaryotic cells. It is embedded deep within the double layered nuclear envelope (NE), and acts as the sole direct connection between cytoplasm and nucleus. This places it at a pivotal point within the central dogma by mediating all RNA transport out of and protein transport into the nucleus, and makes it a defining feature of eukaryotes.

Apart from its canonical function, the NPC is further involved in many other cellular processes such as chromatin organization [8,9], DNA repair [10], gene expression [11,12], and as a connector to the cytoskeleton [13].

1.1.1 The architecture of the NPC

Nuclear pores, as the name suggests, ultrastructurally resemble round pores permeating the nucleus, and were first identified as such in the early 1950s in frog oocytes [14]. Further studies first determined the now characteristic eight-fold rotational symmetry [15] in the membrane plane, and later a layered (pseudo) two-fold symmetric organization across the membrane into two rings and a so-called spoke between them [16]. This rough organization has in fact remained largely unchanged in the decades since and was merely further refined. Perhaps due to its massive dimensions and numbers of subunits, the NPC displays remarkable modularity at several levels of organization. In humans, the core symmetric scaffold consists of a cytoplasmic ring (CR), an inner ring (IR, or spoke ring), and a nucleoplasmic ring (NR) (Figure 1-1A). The CR and NR are themselves composed of two concentric rings of eight so-called Y-complexes, each arranged in a head to tail fashion and dimerized with a slight rotational shift (Figure 1-1A) [17]. Located between them, the IR also displays an internal two-fold symmetry composed of four copies of the inner ring complex (or Nup93 complex) per asymmetric unit. These are arranged in one inner and one outer copy, with a similar rotational shift as in the outer rings, and mirrored at an angle across the membrane plane (Figure 1-1A) [18]. Attached to these core scaffold rings are more peripheral asymmetric subcomplexes; the so-called Nup214 and Nup358 complexes (collectively called cytoplasmic filaments) on the cytoplasmic side, the Nup62 (or central channel Nups) complex on the inner ring, and the nuclear basket on the nucleoplasmic side (Figure 1-1B).

On a molecular level, the NPC across many species is composed of ~30 different proteins [19–22] called nucleoporins or Nups (Figure 1-1B). These assemble in multiples of eight, totaling roughly 1,000 proteins for the human NPC. These proteins have been structurally and functionally classified into stable, folded, scaffold nucleoporins, and more dynamic, often largely disordered, FG-nucleoporins. While this classic division is a little simplistic and many nucleoporins contain characteristics of both classes, it is still a useful mnemonic to represent the two core functions of the NPC: Opening and stabilizing the membrane, and regulating passage.

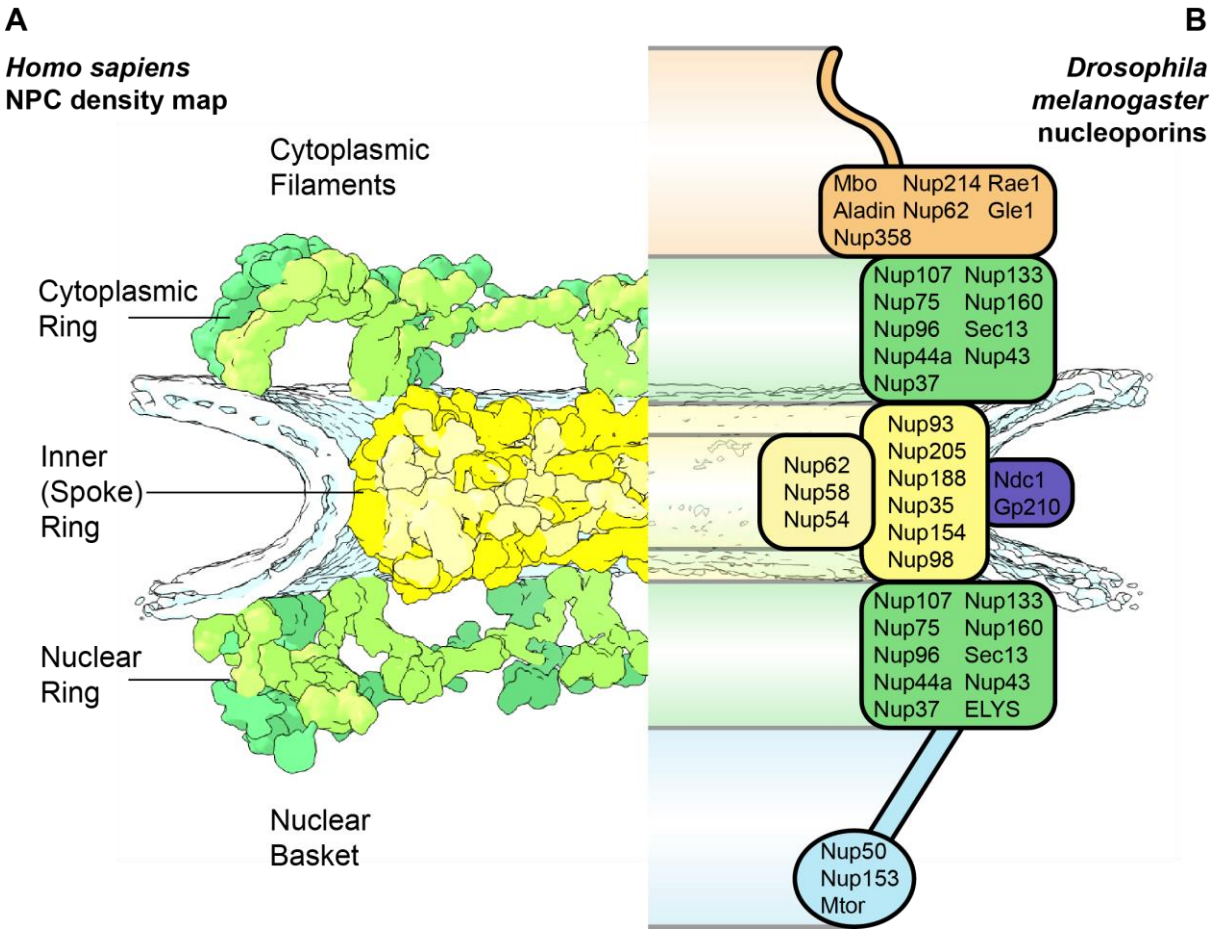

Figure 1-1: Nuclear pore complex architecture and nucleoporin arrangement
(A) Electron density map of the *Homo sapiens* (*H.s.*) NPC core scaffold, determined by cryo electron tomography [23]. Individual rings are pseudo-colored based on their corresponding sub-complexes. The cytoplasmic and nuclear rings consist of two concentric rings of Y-complexes each (light green and dark green) and are arranged in a head-to-tail orientation and dimerized with a rotational shift. The inner ring is composed of a total of four inner ring (IR) subcomplex modules that are oligomerized in a head-to-tail fashion, dimerized with a rotational shift, and mirrored across the membrane plane. Peripheral subcomplexes such as the cytoplasmic filaments, nuclear basket and transmembrane Nups remain unresolved and are thus absent from the depicted electron density map. The NPC is arranged on top of the double layered nuclear membrane depicted in light blue. **(B)** *Drosophila melanogaster* (*D.m.*) nucleoporins and their assumed arrangement across the NPC. Nucleoporins are divided into sub-complexes including cytoplasmic filament Nups (orange), nuclear basket Nups (blue), central channel nucleoporins (light yellow), transmembrane nucleoporins (purple), as well as scaffold Nups including Y-complex members (green) and IR-complex members (dark yellow). Certain nucleoporins act as linker Nups, connecting several subunits including Nup98, Nup93 and Nup35, and others serve as members of several complexes, such as Nup62 (member of central channel Nups and cytoplasmic filaments). ELYS is considered to be part of the Y-complex but only to be present at the nucleoplasmic side. Visualization is based on [EMDB: 3103] [23] and inventory of *D.m.* nucleoporins is based on [Flybase.org: FBgg0000146].

Scaffold nucleoporins

The large scale architecture of the NPC described above is largely constructed of scaffold nucleoporins. Amongst them, another layer of the aforementioned modularity is reflected in the clear recycling of a set of structurally related protein domains. The repeated usage

of N-terminal ß-propellers and C-terminal α-solenoids is highly similar to the COPI, COPII, and clathrin machineries [24]. In all cases, this protein domain architecture is used to stabilize membrane curvature and its evolutionary relationship has been delineated in the protocoatamer hypothesis ([24], updated in [25]). Scaffold nucleoporins are connected to the nuclear membrane by a set of two to four transmembrane nucleoporins (Figure 1-1B) [26,27] with variable degrees of conservation and essentiality [22]. In addition, several nucleoporins that are distributed throughout the scaffold subcomplexes carry membrane-binding motifs, such as amphipathic helices, that provide anchoring stability [28–31].

Holding the pore together are classical protein-protein interactions via folded domains on the one hand, and a large number of short linear motifs (SLiMs) that are often located within intrinsically disordered domains on the other hand. These SLiMs are concentrated on a few key nucleoporins that are placed at strategic points between subcomplexes [32–35]. Interestingly, these sites are among the first to be phosphorylated when the NPC is disassembled in organisms with open mitosis [36]. Such a flexible connection of more or less rigid parts has also been proposed to allow dynamic dilation and shrinkage [33], possibly explaining the varying NPC diameters that were observed in different species and conditions [37,38]. Similarly, unfolded FG-repeat domains have been shown to fulfill a similar role in connecting subcomplexes [39].

FG-nucleoporins

It has been noted early on that many identified nucleoporins displayed a remarkable sequence bias towards phenylalanine and glycine residues, mostly arranged in FxFG or GLFG motifs [40–42]. Isolated via reactivity to antibodies such as mAb414 and the lectin wheat germ agglutinin (WGA, reactivity due to N-acetylglucosamine modification), it was quickly apparent that these Nups were crucial for nuclear pore function, as depletion resulted in nuclei with impaired nuclear transport [43,44]. FG-repeat regions were found to be natively unfolded [45], which is why they are generally averaged out in all current structural models of the NPC (Figure 1-1A) ([18,35,37,46], reviewed in [47]).

From this disordered state of central FG-Nups, many models emerged that try to reconcile the fast yet selective transport of some, and exclusion of other macromolecules (reviewed in [48]). Some of these models rely on coordinated conformational rearrangements [49], others propose an entropic barrier via non-interacting FG-domains dependent on [50] or independent of [51] nuclear transport receptors (NTRs), or entirely NTR-centric models

that are largely independent of FG-Nups [52]. Yet others emphasize the cohesive properties of certain FG repeats and propose that the NPC consists of different regions of dense cohesive domains and loose non-cohesive domains, where all transport takes place [53]. Lastly, focusing on the material properties that arise from alternating cohesive and non-cohesive FG-domains, the pore interior is described as a single coherent 3D meshwork [54]. In this 'selective phase' framework, an analogy is drawn to the lipid bilayer that displays similar properties of selective permeability – here allowing passage of lipophilic, and repelling charged molecules. Effectively assuming the material properties of a 'semi-liquid phase' [54], the multiple weakly interacting hydrophobic FG clusters, separated by evolutionarily conserved hydrophilic spacers [55], are proposed to form a dynamic mesh that passively excludes molecules exceeding its size limit. NTRs would ferry cargo into the central channel by increasing their 'solubility' within this phase as opposed to the generally aqueous cytoplasm, thereby effectively becoming part of the different phase [54].

Though formulated nearly 20 years ago, this is highly reminiscent of the phenomenon of biological liquid-liquid phase separation (LLPS) that has gained a lot of recent attraction [56]. In particular, it describes the archetypical components of the 'sticker and spacer' framework [57], with FG-repeats as stickers and hydrophilic regions as spacers, which postulates a theory explaining network formation and phase separation of polymers. The 'selective phase' model further describes the relationship between FG-Nups and NTRs in now well-recognized functional categories of phase separation, where FG-Nups act as scaffolds[1] of the phase and NTRs (+ cargo) as so-called clients [58]. In this, scaffolds are critical for establishing the phase separation behavior, whereas clients are merely attracted to it and are dispensable for its existence. When purified, FG-Nups quickly form solid fibers [59,60] or gels [61,62] that reproduce the permeability properties of NPCs ([62,63], reviewed in [48]). In polymer physics terms, gelation of polymers such as natively unfolded FG-Nups can occur with or without prior liquid-liquid phase separation [64]. Yet for FG-nucleoporins, a recent study used very fast mixing and imaging via microfluidics to capture a liquid state with similar permeability properties as the gel state, thus arguing for the former [65]. Further prerequisites for spontaneous phase separation are the local concentration of scaffold components to a high extent and the multivalence of interaction domains. Both criteria are certainly fulfilled for FG-nucleoporins, as their grafting concentration within the central channel has been estimated to be in the millimolar range [55], and individual FG-domains carry up to 50 FG-motifs, totaling >5,000 FG motifs per

[1] Note that the term 'scaffold' is used here in a phase separation context, and is different than in the structural context of 'scaffold nucleoporins' mentioned earlier.

NPC [55]. The chemical properties of phenylalanine and glycine, as well as the FG-favoring characteristics of arginine [66], point to hydrophobic, π-π and cation-π interactions as the driving forces involved in FG phase separation [66,67]. This is in line with its sensitivity towards hexanediols, compounds known to disrupt hydrophobic interactions, both *in vitro* and *in vivo* [68,69]. This is quite unusual for biological condensates based on intrinsically disordered proteins (IDPs). Whereas the typical IDP carries few hydrophobic residues but is rich in charged amino acids [70], FG-Nups display the opposite composition [48]. Despite this, FG-Nups have been shown to be recruited to several other known membraneless organelles such as P-granules [71] and stress granules [72] both in health and disease, potentially pointing at a shared underlying phase separation chemistry for these diverse assemblies. What exact functional state nucleoporins assume *in vivo*, both when grafted onto the NPC and prior between synthesis and assembly, has so far not been addressed.

Nup358

Nup358, also known as RanBP2, is special amongst nucleoporins in several regards. First, it is by far the largest with a mass of 358 kDa in humans. Second, it only has known homologs across metazoans [73]. Third, apart from its function within the nuclear pore, it has been found to participate in a vast variety of cellular processes. These include but are not limited to RNA interference [74,75], translational regulation [76], cell polarization [77,78], SUMOylation [74,78,79], and viral infection [80,81]. Outside the NPC, Nup358 also localizes to the axon initial segment [82], kinetochores [83], actin microridges [78], and AL [84].

Within the NPC, Nup358 is asymmetrically located at the cytoplasmic side bound to the cytoplasmic ring [23] and/or the Nup214 complex (Figure 1-1B) [85]. With its C-terminus emanating towards the cytoplasm [86], it is thought to be the main contributor to the cytoplasmic filaments [86]. Its N-terminus is speculated but not proven to bind to the interface between the two Y-complexes that are dimerized at the cytoplasmic outer ring (Figure 1-1B). Depletion of Nup358 leads to loss of the outer cytoplasmic Y ring [23], thus revealing an unexpected role of Nup358 as structural component dictating the higher order stoichiometry of the NPC. Whether there is a corresponding nucleoporin that ensures Y ring dimerization on the nucleoplasmic side is currently unknown. The earlier described architecture of the NPC is not universally conserved across eukaryotes. While the inner ring of all organisms probed thus far has largely proven identical, both the

diameter and the stoichiometry of the outer rings was subject to change during evolution. As described, the human NPC is composed of two Y-complex rings on either side with eight copies each, amounting to 32 copies total (Figure 1-1A) [17]. This is markedly different in both green algae [37] and budding yeast [46], which possess two nuclear and one cytosolic (= 24 Y-complexes) and one nuclear and one cytosolic (= 16 Y-complexes) ring respectively. Perhaps not by coincidence, these organisms do not possess an obvious homolog of Nup358.

Nup358 is a good example where the simplified classification into scaffold and FG-nucleoporins is inadequate. While it contains a fair number of FG-repeats and disordered regions distributed throughout its length (Figure 1-2A), it also contains many structured domains, some of which are essential for its scaffold function. For the human protein, its already mentioned N-terminus consists of the NPC typical α-helical domain rich in leucine residues and TPR repeats, followed by an unstructured region and four Ran-binding domains (RBDs) (Figure 1-2A) [47]. Between the first and second RBD, there is a total of eight Ran-binding zinc-finger domains (Figure 1-2A) that are shared with Nup153 on the nucleoplasmic side [87]. Between the third and fourth RBD, the only known enzymatic activity within the NPC is situated in form of a bitartite, natively unfolded, SUMO E3 ligase domain (Figure 1-1A) [88]. Tightly bound in a complex with the E2 conjugating protein Ubc9 and SUMO1-conjugated RanGAP1 [88–92], this multi-subunit ligase localizes both SUMOylation and RanGAP activity towards the NE. At the very C-terminus, a cyclophilin homology domain houses a weak peptidyl-prolyl isomerase activity (Figure 1-2A) [93], that can theoretically act as a protein folding chaperone. In addition to these annotated domains, Nup358 further contains binding sites for the NTRs NXF1 [94], exportin 1 (Crm1) [95] and importin ß [96], several proteasome subunits [97], the dynein-adapter BicD2 [98,99], several kinesin isoforms [99,100], and others. The simultaneous connection to the opposing microtubule (MT)-associated motors kinesin and dynein apppears to result in a tug of war between them to position the nucleus during spindle assembly [98,99].

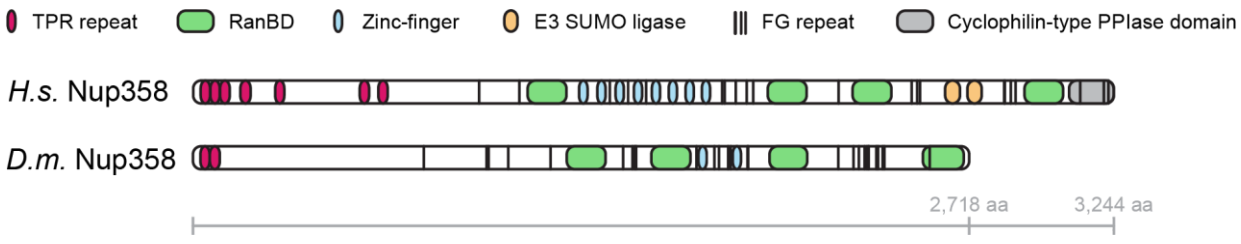

Figure 1-2: Domain architecture of Nup358 (RanBP2)

Schematic representation of *Homo sapiens* (*H.s.*) and *Drosophila melanogaster* (*D.m.*) Nup358 domain architecture. The two internal repeat SUMO E3 ligase domain, as well as the cyclophilin-type PPIase domain are absent from *D.m.* Nup358. *D.m.* Nup358 also carries a reduced number of TPR repeats and zinc-finger domains. Schematic is drawn to scale according to [Uniprot: P49792] and [Uniprot: A0A0B4K7J2].

Interestingly, the second tethering function of Nup358, that of RanGAP to the NE, is absent in fungi [101] and works independently of Nup358 in plants [102]. It is therefore unclear how important NE localization of RanGAP activity is. While the interaction in vertebrates is dependent on SUMOylation [92], plants utilize an N-terminal NE targeting domain [102]. Like in other animals, *Dm*RanGAP of *Drosophila melanogaster*, the model system of this study, is located at the NE [103]. However, the annotated E3 ligase domain that also serves as binding site for Ubc9 and SUMOylated RanGAP in humans [88], is absent in *D.m.* (Figure 1-2B) (Uniprot: A0A0B4K7J2). It is therefore currently not obvious how this tethering is achieved in *Drosophila*.

1.1.2 Nucleocytoplasmic transport and the Ran cycle

A single NPC allows combined cargo on the order of its own mass (~100 MDa) to cross its barrier each second [54]. This translates to a rough estimated rate of 1,000 molecules per NPC per second, and a residence time of ~10 milliseconds for model cargoes [54,104], although this is dependent on the type of NTR, cargo, and their concentration [105].

It is generally stated that macromolecules smaller than ~30 - 40 kDa can passively diffuse through the NPC, whereas larger molecules require active shuttling via NTRs. However by now, it has gained acceptance that a) this is not a hard cut-off but rather a gradually increasing energetic barrier, and b) this barrier depends not strictly on size, but the combined physiochemical properties of the cargo (i.e. hydrodynamic properties, surface chemistry, etc.) [66,106]. Illustrating this, it is possible by protein engineering to change a generally inert cargo protein such as GFP that would usually be excluded from the NPC, to either behave like a putative NTR and rapidly enter the pore or to be excluded a lot more effectively [66]. General rules that govern this behavior are the FG-favoring effects of hydrophobic (W, Y, I, F, M, H) residues and cysteine/arginine (R presumably due to cation-π interactions, C possibly due to favorable packing with hydrophobic residues), and the FG-repelling effects of other charged (E, D, K) amino acids [66]. This both gives insights about the molecular grammar of the NPC permeability barrier, and to a degree reflects the properties of naturally evolved NTRs. They are amongst the most hydrophobic soluble proteins within cells [68] and contain a large number of both arginines and

cysteines on their surface [66]. On the other hand, they also display a lot of surface-exposed negative charges which would lower their FG partitioning [107], presumably to counteract the increased aggregation propensity due to their hydrophobicity [66]. When bound to a substrate, NTRs shield the less FG-favorable cargo surface with its own more optimal one – although it was recently shown that this has limits and can fail for highly unfavorable cargoes [66]. On their convex surface, NTRs indeed carry many discrete characterized FG binding patches [108,109], each only transiently associating. These so-called 'fuzzy' interactions result in a highly dynamic system [110] – a prerequisite to achieve the staggering translocation speed of the NPC.

With this current description of multivalent FG-favoring interactions of NTRs within the pore, how does this result in directional transport across, rather than accumulation within the pore? Due to the extremely high on and off rates of FG-NTR*cargo binding events, the specific release or retention on one side effectively results in fast directional movement. This was shown biochemically by placing phenyl-sepharose beads with high affinity towards importin ß on the edge of an importin ß*cargo-soaked FG-hydrogel. The importin ß*cargo complexes quickly exited the gel and accumulated on the beads [62]. A similar effect can be achieved via addition of the small GTPase Ran in its GTP-bound state (RanGTP) both in the FG-hydrogel setting [62] and in permeabilized HeLa cells [111]. Within the cell, likely both the biased dissociation of importin*cargo complexes [112] and lowered affinity of NTRs towards nucleoplasmic FG domains by RanGTP [113] contribute to this effect.

The required underlying localization of RanGTP to the nucleus and RanGDP to the cytosol is called the Ran gradient and it is largely attributable to asymmetric localization of two converting enzymes: The RanGEF (guanine nucleotide exchange factor) RCC1, which is bound to chromatin (Figure 1-3A) and stimulates exchange of GTP for GDP, and the aforementioned RanGAP (GTPase-activating proteins), which is tethered to Nup358 on the cytoplasmic face of the NE (Figure 1-3A). As the binding of cargo and shuttling into the NPC by NTRs does not require energy, the Ran GTPase cycle is considered the sole energy source of active nuclear transport [114].

After importin*cargo complexes cross the NPC, interaction with RanGTP induces a conformational change of the importin that results in dissociation from the cargo (Figure 1-3A) [115]. The resulting RanGTP-importin complex then crosses the NPC with help of an export factor called CAS, where it gets dissociated by cytoplasmic Ran-binding proteins [116]. Following GTP-hydrolysis by RanGAP, RanGDP is then recycled back to the nucleus via NTF2 [117,118]. Importin ß follows the same recycling pathway back to the

cytoplasm in complex with RanGTP, but requires no additional factors to do so. For nuclear export, cargoes carrying NESs are recognized by exportins in the presence of RanGTP [119] (Figure 1-3A). The resulting complex crosses the nuclear pore, where it is also disassembled by Ran-binding proteins and GTP hydrolysis via RanGAP [120] (Figure 1-3A). Lastly, the nuclear export of RNA is Ran-independent [121] and mediated by a heteromeric complex of NXT1 and NXF1 [122].

Nuclear transport receptors

The human genome encodes for at least twenty importin ß family NTRs, seven importin α family NTRs, and four NTRs with different folds [123], whereas the *Drosophila* genome encodes four importin α and eleven importin ß family members (Flybase.org: FBgg0000703). Importin α family members often but not always function in combination with importin ß family members by acting as cargo-binding adaptors for importin ß. All importin α proteins consist of multiple repeats of the classic armadillo fold, each composed of three α-helices, that mediate nuclear localization signal (NLS)-based substrate binding (reviewed in [124]). At the N-terminus, the importin ß binding domain (IBB) is required for association with importin ß. Importin ß family members on the other hand consist of 18-20 so-called HEAT repeats, each containing two antiparallel α-helices (reviewed in [125]). This fold is strikingly similar to the alpha-helical domains of certain nucleoporins, and has prompted speculation about a shared evolutionary origin, where initially static NPC components gradually evolved to become the soluble component of nucleocytoplasmic transport [126,127]. These HEAT repeats arrange in a superhelical fashion, with substrate or IBB binding on its inner concave surface and FG-binding on its outer convex surface (reviewed in [125]). Depending on their transport directionality into or out of the nucleus, they are commonly divided into importins or exportins, but NTRs facilitating both directions also exist [128]. In broad terms, NTRs recognize cargoes carrying short signal peptides: A nuclear localization signal (NLS) for import or a nuclear export signal (NES) for export. NTRs display both functional redundancy and family member-specific differences in cargo spectra [123].

Classical nucleocytoplasmic transport is assumed to rely on diffusion. However, certain importin ß family members have previously been found to bind microtubules and molecular motors ([129], reviewed in [130]). This was shown to be involved in the nuclear import of several viruses (reviewed in [131]), cancer regulatory proteins [132], and in retrograde signaling in neurons [133,134]. In their function as cargo binders, NTRs not

only transport proteins but can also chaperone them [135], thereby both shielding aggregation-prone proteins and regulating the interactome of their substrates. This is employed both in spindle and NPC assembly (Figure 1-3B). During mitosis, importin α and ß bind and thereby inhibit so-called spindle assembly factors everywhere in the cytosol except at chromosomes, where high RanGTP releases them. This results in local MT assembly (reviewed in [136]). Similary, Nups are chaperones by NTRs during mitosis and locally released upon certain spatial and temporal cues [137]. Outside of mitosis, NTRs can also dissolve molecular aggregates and phase separated assemblies built from their cargoes [138–140]. It is thus becoming increasingly obvious that in addition to nucleocytoplasmic transport, NTR-mediated chaperoning has many other important cellular functions.

1.1.3 NPC assembly

How does the cell know where and when to build nuclear pores? And how is it then mechanistically ensured that assembly only occurs at the specified time and place?

For the assembly of most large and complicated macromolecular complexes, such as proteasomes or ribosomes, there is a set of proteins that ensure its function, and a separate set a of proteins that ensure its assembly. Taking proteasomes as an example, there is a set of well-characterized, specialized assembly factors that mediate its construction in ordered steps (reviewed in [141]). In addition, there is a set of auxiliary proteins such as ubiquitin and the ubiquitination cascade, shuttling factors, and receptors that aid its cellular tasks (reviewed in [142]). The nuclear pore complex on the other hand uses the same protein network that it employs for nucleocytoplasmic transport also for its assembly (Figure 1-3A). While RanGTP acts as nucleoplasmic marker during transport, it fulfills the same role during assembly. And while NTRs chaperone cargoes and release them upon encountering RanGTP in the nuclear interior, they perform a similar role with nucleoporins during assembly.

However, while lower eukaryotes only use a single *de novo* assembly pathway during interphase, metazoans additionally need to re-build NPCs after their disassembly during mitosis. These two assembly modes show both commonalities and differences, and represent a rare case of separate cellular assembly pathways accomplishing the same goal [143].

Postmitotic assembly

Of the two characterized NPC assembly pathways, postmitotic assembly is significantly better characterized, mainly due to its defined timing. During mitosis, most metazoans break down their NE, and typically their NPCs alongside. This is initiated via widespread protein phosphorylation by mitotic kinases such as PLK1, CDK1, VRK1, AURKB, PKC, and NEKs (reviewed in [144]). Within the NPC, this phosphorylation is economically clustered around the few inter-subunit connecting hub proteins of Nup98 [36] and Nup53 [145], that carry important connecting SLiMs. Consequently, Nup98 is dissociated from the NPC early on [146], which results in a reduction of the permeability barrier [36]. This is followed by additional phosphorylation events [147] and rapid dissociation of the other nucleoporins [146]. During mitosis, many key mitotic players and NE proteins including the nucleoporins Nup62, 98, 153, 214, 358, ELYS and the Y-complex are kept in solution chaperoned by NTRs, especially Importin α, ß1/ß2 (Figure 1-3, reviewed in [148]).

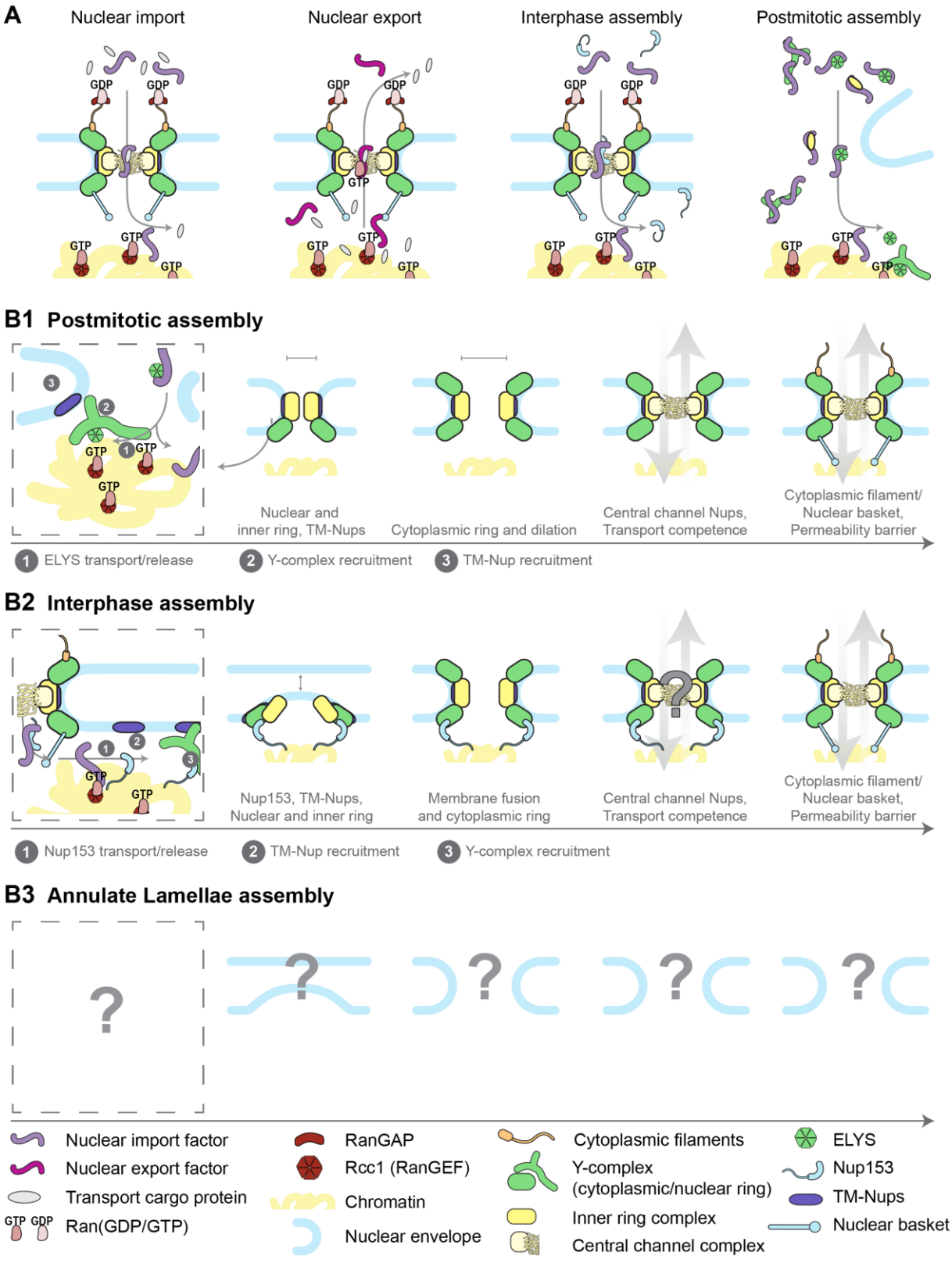

Figure 1-3: NPC assembly mechanisms and molecular commonalities between assembly and nucleocytoplasmic transport

(A) Schematic depiction of the molecular basis for nuclear import, nuclear export, interphase assembly and postmitotic assembly. In all cases mediated by nuclear import factors, cargo or nucleoporins are kept in solution by nuclear transport receptors (NTRs), shuttled through the NPC or cytoplasm, and released locally upon encountering RanGTP. RanGTP is enriched around chromatin via Rcc1. For nuclear export factors, the directionality is reversed, displaying cargo-

binding in presence of RanGTP in the nucleus and cargo release upon GTP hydrolysis via Nup358-RanGAP at the cytoplasmic side of the nuclear envelope. **(B)** Temporal progression of NPC assembly mechanisms. (B1) During postmitotic assembly, local seeding occurs by local release of NTR-chaperoned ELYS at decondensing chromatin (1), followed by recruitment of remaining Y-complex members (2) and the TM-nucleoporins Ndc1/Pom121 (3). Nuclear and inner rings are discernable on small membrane fenestrations early on, followed by dilation and addition of an outer ring. Establishment of transport competence occurs and is completed by addition of peripheral complexes such as cytoplasmic filaments, central channel Nups and nuclear basket. Finally full permeability barrier capacity is established via addition of yet unknown factors. (B2) During interphase assembly, nuclear import of the nuclear basket component Nup153 via NTRs is a crucial early step (1), but likely preceded by other membrane-bound factors. Subsequent recruitment of the TM-Nup Pom121 (2) and the Y-complex (3) establishes seeding of a new NPC insertion site. Ultrastructurally, small mushroom-shaped membrane evaginations are the earliest discernable event, followed by vertical and lateral growth of the evagination and fusion of the inner and outer membrane. An eight-fold nuclear ring is apparent from the earliest stages, in addition to central density that develops clear symmetry over time. Membrane fusion is completed by addition of the cytoplasmic ring and peripheral subunits, and the eventual establishment of transport competence and permeability barrier. (B3) Contrary to nuclear NPC assembly mechanisms, virtually nothing is currently known about the molecular determinants of cytoplasmic Annulate Lamellae pore or stack formation. Figure was based on [149].

Temporally, both NE and NPC reformation are initiated by the inactivation of these mitotic kinases and concomitant up-regulation of phosphatases at the end of mitosis ([150,151], reviewed in [152]). This is enhanced and locally directed towards chromosomes by ELYS, which locally recruits protein phosphatase 1 (PP1) [151]. ELYS is itself locally released from importin ß1/ß2 by RanGTP and bound to chromosomes (Figure 1-3B1, [153,154]). As described previously, also here RanGTP acts as spatial cue via chromosome-bound RCC1. Illustrating their importance, artificial tethering of RCC1 and ELYS to nucleosome-free DNA in *Xenopus laevis* egg extracts is sufficient to initiate NPC assembly [155], whereas depletion of ELYS or addition of soluble RanGTP results in aberrant assembly of NPCs at the ER in form of Annulate Lamellae [137,156]. ELYS recruits the Y-complex [143,156], the TM-Nups Ndc1/Pom121 [157,158] and Nup53 [28,159], possibly alongside membrane, which in turn recruit connectors [159,160], the inner ring complex [161] and the central channel nucleoporins [162] (Figure 1-3B1). Finally the asymmetric cytoplasmic filament and nuclear basket components are recruited and pores become transport competent [146], followed later by establishment of the full permeability barrier (Figure 1-3B1) ([163], reviewed in [164]). What additional factors are required for this last maturation step is still unclear, but might include non-nucleoporin soluble factors such as NTRs.

On an ultrastructural level, post-mitotic assembly seems to start ~3 min after chromosome separation from small remaining holes within the fenestrated endoplasmic reticulum (ER) (Figure 1-3B1) [165]. These holes initially accumulate central channel and nuclear densities, the latter already displaying eightfold symmetry. As the central density

increases and an inner ring becomes distinguishable, the membrane opening widens and an eightfold cytoplasmic ring appears. The pore finally reaches its full mature width with now clearly identifiable NR, IR and CR densities (Figure 1-3B1) [165]. How the initial recruitment of ELYS is spatially coordinated with ER fenestrations is currently unclear.

Importantly, several Nup subcomplexes remain intact during mitosis [166]. Furthermore, the utilization of pre-existing holes eliminates the need for costly membrane fusion [165]. Consequently, postmitotic assembly finishes within ~10 min and produces transport-competent NPCs.

Interphase assembly

After a cell has divided and distributed its nucleoporins between the two daughters and they have reassembled their NPCs, each new cell has to prepare for the next round of cell division. This includes doubling their nuclear size and, in order to maintain a steady nuclear pore density, consequently NPC number. Contrary to postmitotic assembly, this occurs via slow, stochastic insertion of NPCs via membrane fusion from newly synthesized nucleoporins [167]. As NPC density differs between cells, it has long been a mystery how cells decide when to produce another pore. Recently however, a regulatory pathway that relies on TPR and Nup153 (two nuclear basket components) and acts through the MAPK/ERK pathway was shown to regulate NPC number [168]. Temporal regulation might thus arise by a continuous monitoring of NPC density via their nuclear protrusions.

Interestingly Nup153, although largely dispensable for postmitotic assembly [169,170], is crucial during initiation of interphase assembly [170]. Imported into the nucleus through existing nuclear pores via importin ß2 (transportin), it is again locally released via RanGTP, thus directing NPC assembly to the nuclear envelope (Figure 1-3B2) [170]. As Nup153 binds to highly curved membranes, it is likely that other proteins carrying membrane-bending activity (such as Nup53, Pom121, Sun1, or reticulons, reviewed in [171]) precede Nup153 at the membrane. Indeed it has been shown that Pom121, also dependent on NTR-mediated transport [172], arrives before the Y-complex during interphase, but later during postmitotic assembly (Figure 1-3B2) [173]. Nup153, analogous to ELYS during postmitotic assembly, then recruits the Y-complex (Figure 1-3B2) [170]. A comprehensive assembly order as it has largely been determined for postmitotic assembly ([146], reviewed in [164]), from here onwards has yet to be completed. Either replacing or in addition to the sequential, binary recruitments of Nups, the subunit-connecting properties of disordered FG-Nups have recently been introduced

in the so-called 'velcro' hypothesis in yeast [39]. Here, cohesive GLFG domains in *y*Nup188 and *y*Nup116 (homolog of *h*Nup98) can stabilize critical NPC scaffold interactions. These are important for late-stage interphase assembly and act as targeting determinants to the NPC. Yeast cells lacking Nup116 or just its GLFG domains in the absence of Nup188, fail to assemble NPCs and instead produce well-known assembly/degradation intermediates called herniations [39]. These sometimes mushroom-shaped evaginations of the inner nuclear membrane towards the lumen were described in many yeast nucleoporin mutants over the years (reviewed in [174]). Recently, work in human cells found similar structures during interphase assembly and followed their ultrastructure through different intermediates to maturation (Figure 1-3B2) [175]. Here, similar to postmitotic assembly, an eightfold nuclear ring appears early on. A dome-shaped central density at the inner nuclear membrane (INM) gradually grows laterally and vertically towards the outer nuclear membrane (ONM) over the course of ~50 min (Figure 1-3B2) [175]. Finally the membranes fuse, the cytoplasmic ring is added, and the central density differentiates into distinct central and membrane-proximal regions with eightfold symmetry (Figure 1-3B2). Contrary to postmitotic assembly, the nuclear ring diameter stays rather constant throughout this process [175]. A direct correlation of this ultrastructural description of intermediates with molecular identity of the proteins involved and the rough nucleoporin assembly order mentioned earlier however was so-far unattainable.

Conceptually, interphase assembly is much more demanding for the cell than postmitotic assembly for several reasons. First, nucleoporins are presumably newly synthesized to double the amount of NPCs and are thus not already pre-assembled into subcomplexes. Second, a continuous membrane connection has to be established via fusion of the INM and ONM rather than using existing ER fenestrations. Third, the permeability barrier has to be maintained during this entire process, whereas the barrier is broken down during mitosis and is only re-established afterwards. Consequently, the need for controlled membrane deformation puts increased emphasis on protein domains that either induce or sense membrane-curvature. This is illustrated by the fact that such domains within Nup53 [28], Nup133 [143], Nup153 [170] and the targeting of the INM proteins Sun1 and Pom121 [176] are essential during interphase assembly but dispensable during postmitotic assembly (reviewed in [171]). The exact driving forces for membrane shaping during NE fusion are still largely enigmatic. In addition to the aforementioned evolutionary relatedness of several scaffold nucleoporins to COPI/II and clathrin vesicle coats [24], there are additional parallels with other membrane remodeling pathways that allow inferences. Indeed over the years, several known remodelers such as

reticulons, YOP1-family proteins, ESCRT proteins, and torsins have all been implicated in nuclear pore fusion (reviewed in [27,171]).

1.1.4 Annulate Lamellae

Contrary to what their name suggests, nuclear pores are not exclusive to the nucleus. They also frequently occur embedded in parallel stacks of cytoplasmic membranes called Annulate Lamellae (Figure 1-4, reviewed in [177]); then referred to as Annulate Lamellae Pore Complexes (ALPCs). AL have been an obscure cellular feature with enigmatic function and biosynthesis for close to 60 years (first described in 1950 [14]). Due to a difficulty to purify them for biochemical analysis, much of our previous knowledge is based on morphological characterization within different cells and tissues by electron microscopy (EM) and immunofluorescence, and is thus rather descriptive.

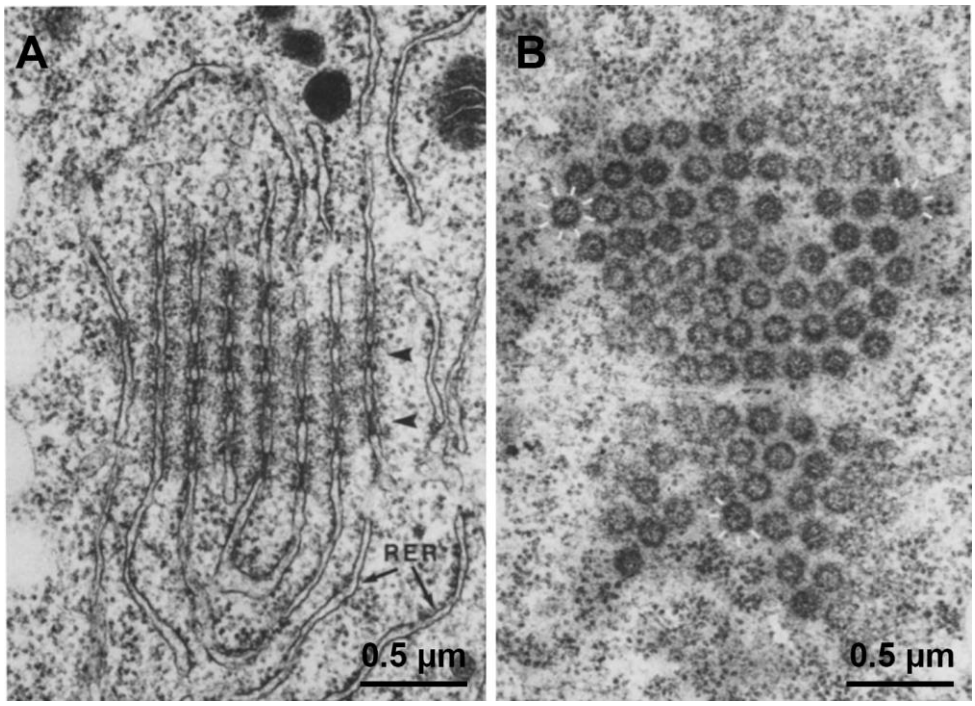

Figure 1-4: Annulate Lamellae from *Drosophila melanogaster* embryos
(A) Cross section of a single eight-layered parallel membrane array embedded within the rough ER (RER) of the embryonic cytoplasm. Arrows indicate individual densities of aligned pores. **(B)** Tangential section of a large Annulate Lamellum with many hexagonally packed pore complexes. Pores display a central granular density as well as up to eight smaller radial densities (white dashes). Surrounding the pore complexes are structures characteristic of polysomes as also apparent in (A). Image adapted from [178].

Based on their superficial morphological resemblance of nuclear pores (Figure 1-4) and their prevalence in gametes and highly proliferative cells (reviewed in [177]), AL were

soon postulated to serve as a storage for nuclear pore complexes [179]. Fittingly, they were often found in close proximity to the nucleus and sometimes even continuous with its membrane [180–182]. There is however a vast collection of other proposed functions and determinants for their appearance that are discussed elsewhere (reviewed in [177,183]). While some studies based on EM morphometry and subcellular fractionation found no significant contribution of AL as NPC storage in *Drosophila melanogaster* (fruit fly) embryos [178,184], other work later showed the opposite [84]. Based on quantitative live cell fluorescence microscopy, volume EM, and correlative light and electron microscopy (CLEM), *en bloc* insertion of AL into rapidly expanding nuclei was demonstrated and quantified to contribute substantially to nuclear growth [84]. Based on proteomic measurements, ALPCs were speculated to be symmetric (contrary to NPCs), thus lacking certain peripheral nucleoporins, and to mature only after insertion into the nuclear membrane. Importantly, the permeability barrier is maintained throughout this process, despite the large-scale remodeling of the NE [84]. Recently, similar insertions have also been observed in other systems such as human cell lines [185].

Fly ALPCs, just like NPCs, are disassembled during metaphase and rapidly reappear during mitotic exit [150,178], although contrary to mammals this occurs without NE breakdown [178]. As in other systems, this cycle of disassembly and reassembly is mediated by kinases such as Cdk1 and opposing phosphatases [150]. It is thus reasonable to assume that a similar postmitotic assembly mechanism as it was described for NPCs, is also at play for ALPCs. Compared to the two relatively well-documented NPC assembly pathways at the nucleus, very little is known mechanistically about AL assembly (Figure 1-3B3). Even more so, transferring the identified rules and guidance cues of the nuclear assembly modes would largely not be applicable for AL. Whereas the temporal cue in postmitotic assembly – dephosphorylation at mitotic exit – might very well be preserved, a spatial cue guiding AL assembly towards ER rather than the nucleus or anywhere else in the cell is not readily apparent. As described, RanGTP acts as a spatial marker for chromatin via nucleosome-attached Rcc1 in both documented nuclear assembly pathways. In cytoplasmic AL however, both membranes are facing the cytosol and there is no nuclear compartment or chromatin nearby. A possible alternative might be specific localization of Rcc1 or of a yet to be identified RanGEF molecule towards the ER, which would then fulfill an analogous role in AL assembly. Fittingly, in *Xenpous laevis* egg extracts that are capable of assembling a NE and NPCs around added sperm chromatin, the omission of such chromatin [186] or addition of excess cytosolic RanGTP [137] induces AL formation. A similar effect is achieved *in vivo* by depletion of the downstream initiating factor ELYS

[156]. Furthermore, the pre-assembly of AL in such extract diminishes its capability to produce NPCs upon later addition of chromatin [187], thus implicating that many of the same factors are involved and necessary for both NPC and ALPC assembly. Morphologically, several mutually non-exclusive biosynthesis pathways have been proposed, such as budding from the NE [188], differentiation from golgi cisternae [189], differentiation from ER sheets or vesicles [179,190], and differentiation from nucleolar material [191]. All of the above however were based on individual EM snapshots of defined developmental stages, therefore lacking information about continuous progression or molecular identity.

One final occurrence of cytoplasmic pores that is worth highlighting is that within the *Caenorhabditis elegans* germ line. Here P granules, which by now have become a textbook example of phase separated membraneless organelles [192], are found tightly associated with NPCs and MTs at germ cell nuclei [193]. Later in development, P granules alongside NPCs were described to detach from the nucleus and become cytoplasmic; although cytoplasmic NPCs were only seen in mutant worms that cannot rapidly self-fertilize [193]. In EM, these dense granules attached to single-sheeted porous membrane stretches look remarkably similar to proposed AL assembly intermediates in *Drosophila* [191,193]. They further display a layered arrangement [194] that is reminiscent of the layered NPC architecture and their integrity is crucially dependent on several nucleoporins including Nup358 [71]. Appropriate to their overall function, these composite structures also accumulate many different RNAs in and around them [194].

1.2 mRNA localization and local translation

With the establishment of immunofluorescence techniques and the introduction of molecular cloning and fluorescent proteins to cell biology, protein localization rapidly emerged as an important attribute. Considering the many different organelles and microenvironments within eukaryotic cells, hardly any protein is evenly localized and thus their function is spatially restricted. This differential localization is largely achieved by a system of cellular trafficking based on short signal peptides that encode each protein's destination (reviewed in [195]). Correspondingly, with the use of *in situ* hybridization (ISH), the protein coding mRNAs – as well as other RNA species – have also been recognized to display widespread and distinct subcellular localization [196–202]. Analogous to proteins, their destination is also genetically encoded in primary sequence elements within these molecules (reviewed in [203]). This subcellular RNA localization has proven important for spatially restricted molecular activity such as chromosome compaction, splicing, RNA storage and degradation, and/or translation (reviewed in [204]).

As mRNAs encode for proteins, the effects and importance of their localization are not to be viewed in isolation but rather in combination. Consequently, RNA localization and local translation are often intimately linked and co-regulated. A single mRNA molecule can produce multiple protein copies, which is a likely reason for the significantly lower cellular abundance of mRNAs compared to proteins [205]. If the ultimate goal is localized protein activity, it is thus economical to enforce localization on the mRNA level. Additionally, analogous to prokaryotic operons [206,207], concentration of mRNAs encoding related proteins combined with local translation could allow the formation of local transcriptomes that function independently of the distant nucleus. Several such examples are described under the so-called RNA regulon hypothesis, postulating that this co-regulation of functionally related mRNAs via shared RBPs replaces the lack of physical operons in eukaryotes [208]. Amongst the most prominent examples is the yeast RBP Puf3, which recruits, anchors and regulates over a hundred nuclear-encoded mitochondrial proteins towards mitochondria [209,210]. This might be particularly important during protein complex assembly, where diffusion is often a rate-limiting step [211], and in cells that display a large size or a high degree of polarization (e.g. neurons, filamentous fungi, or oocytes). Fittingly, locally translated proteins are more likely to contain protein-protein interaction domains [212] and might thus facilitate rapid proteome reorganization, at least partially by reducing diffusion-based association and

assembly. Finally, localized translation is often necessary for delicate gene products, as many proteins are in fact detrimental to their cell or organism when active at the wrong time or place. Prominent examples of this are critical cell cycle regulators [213], and regulators of morphogenesis [214]. Coupling translation initiation to an achieved spatial destination can thus mitigate this effect.

In eukaryotes, the life cycle of an mRNA molecule begins with its transcription by the RNA polymerase Pol II in the nucleus, where early decisions about its fate are already determined. Through selection of alternative transcription start sites, alternative splicing, and alternative termination/polyadenylation sites, localization-determining *cis*-regulatory elements are either included or excluded from the nascent transcript (reviewed in [203]). Co- or peri-transcriptional events such as loading of the exon junction complex have been shown to exert profound effects on ultimate localization and thus phenotype [215]. After decoration with nuclear *trans*-regulatory RNA-binding proteins (RBPs) [216,217], the new ribonucleoprotein particle (RNP) is then shuttled across the NE via the NPC [218,219], where it is briefly retained for quality control and RNP remodeling ([220,221], reviewed in [222]). From here on, localizing RNPs can reach their destination through one of several characterized mechanisms or a combination thereof (reviewed in [223,224]):

1. **Directed, active, motor-dependent transport**. (Figure 1-5A)
   Perhaps the most well-studied mode of RNA localization is achieved via motor-dependent transport along the cytoskeleton (i.e. mostly F-actin and microtubules). The earliest and most prominent examples of this include the identification of actin-based transport of *ASH1* in yeast [225,226], as well as MT-based transport of ß-*actin* in vertebrate fibroblasts and neurons [201,227], of *Vg1* in *Xenopus* oocytes [228] and several axis determining factors such as *oskar* in *Drosophila* oocytes [229].
   The latter case highlights the intricacies of this mode of transport especially well: Initially, *oskar* is trafficked via dynein motors towards MT minus-ends into the growing oocyte [230,231]. After reorganization of the MT network, a shift towards plus-end directed transport via kinesin occurs, which leads to accumulation at the posterior end [232–234]. As both motors are likely loaded early on via adapter proteins and are dynamic parts of the RNP throughout its path [235], net transport direction results from differential regulation of motor activity [235] and a weakly polarized MT network [236,237]. Similar movement along slightly polarized MT-networks or biased bi-directional movements are also observed for RNP transport

in other systems [238,239]. Throughout its path, *oskar* is transported in a translationally repressed state, which is crucial to prevent detrimental premature translation [240,241] and is a reoccurring feature of transported mRNAs (reviewed in [242]). At the posterior pole, *oskar* is actively anchored [243,244], but this anchoring is not stable and additionally depends on persistent trafficking [245]. The combination of adapter-mediated RNP-motor association, their differential regulation, translational silencing along the way, and a specific arrangement of the MT tracks thus ultimately leads to localized translation and accumulation of Oskar protein for germ plasm specification.

The same or similar molecular machineries and regulatory logic have been demonstrated or are suspected in the long-range localization of numerous transcripts in many other large cell types. In neurons e.g., RNA localization appears to be the best descriptor of protein abundance changes along the somite-neurite axis [246].

2. **Hitchhiking on other cargos** (Figure 1-5B)

   A variation of directed, active, motor-dependent transport is the co-transport of RNPs attached to other cargo such as membrane-bound organelles (reviewed in [247]). Initially described mostly for endosomes [248] and ER/Golgi-derived vesicles [249–251], lysosomes are another recent addition to the growing list of such RNP vehicles [252]. However there is also considerable co-migration between these organelles, allowing for the possibility of even bigger co-migrating cargo assemblies ([253], reviewed in [254]). This would seem to constitute an economic solution for cellular transport where several cargos share a common destination. In fact, every example mentioned earlier under direct motor-dependent transport, has also been implicated in hitchhiking alongside organelles ([251,252], reviewed in [255]). As RNP-adaptor-motor interactions can be dynamic [235], and cargo generally does not reach its destination along a straight, uninterrupted path [256–258], there is ample opportunity for local exchange of transportation partners.

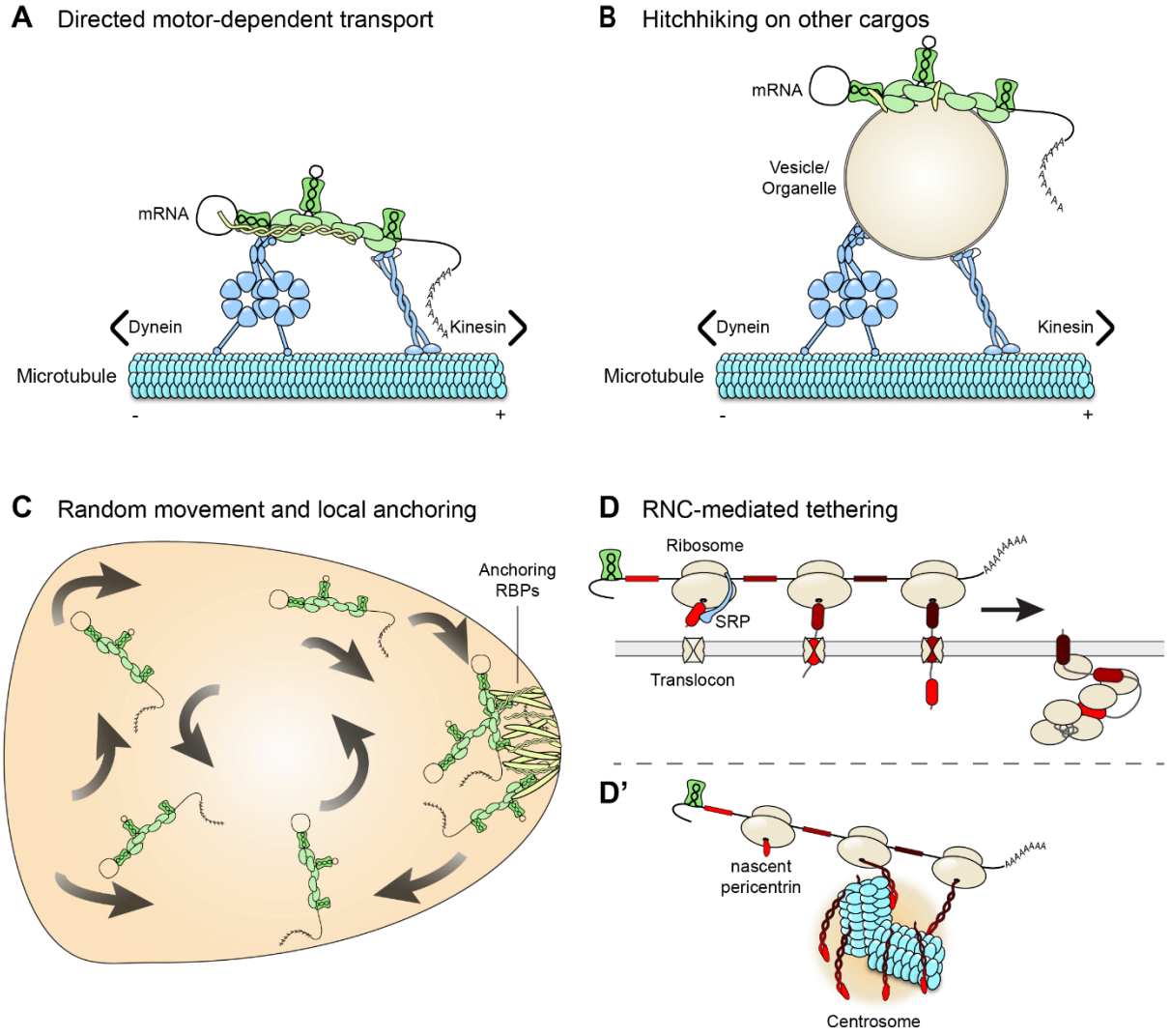

Figure 1-5: Different mechanisms of RNA transport and localization
(A) Complexes consisting of RNA and proteins, called ribonucleoproteins (RNPs, green) can be transported actively along cytoskeletal elements (e.g. microtubules) via attachment to adapter proteins (yellow) and motor proteins (e.g. dynein/kinesin, light blue). **(B)** RNPs can further be attached to other cellular cargo (e.g. vesicles/organelles) that are themselves transported along the cytoskeleton via motor proteins. Such a transportation mode is referred to as 'hitchhiking'. **(C)** Local anchoring is involved in many modes of RNA localization but it can also be its sole determinant in combination with random movement. Random movement (arrows) can occur passively via diffusion, or actively via cytoplasmic streaming or motor-dependent transport along an unpolarized cytoskeleton. Local anchoring (or protection) is often achieved via locally tethered RNA-binding proteins (RBPs, yellow), static motor proteins, or a static cytoskeleton. **(D)** Local tethering can further be achieved via the Ribosome-nascent chain complex (RNC) and thus dependent on peptide rather than RNA directly. Prominent examples include the co-translational tethering of secretory/transmembrane RNCs to the translocon and the endoplasmic reticulum via the signal-recognition particle (SRP) (D) or the co-translational tethering of Pericentrin RNCs to the pericentriolar matrix during centrosome assembly (D').

The molecular connections between specific motor-cargo-cargo combinations are still largely unexplored with a few specific exceptions. On the one end of the complex, there are many well-characterized adapters for motor-organelle

interactions (reviewed in [259]). On the RNA-organelle side on the other hand, there are only a few connector molecules directly implicated in hitchhiking. These include the RBP Rrm4, which recognizes both a set of RNAs and Upa1 that acts as endosome membrane adaptor [260,261], as well as Annexin A11, which tethers RNPs to lysosomes [252]. In addition however, the involvement of broad-specificity organelle-tethering RBPs such as Puf family members [262] also during hitchhiking would seem rather plausible.

Contrary to many directly motor-bound RNPs that are translationally silenced during transport, organelle-mediated co-transport is often associated with active translation [253,263–265] and possibly even co-translational protein complex assembly ([266], reviewed in [267]).

3. **Random, active/inactive movement and local anchoring/protection** (Figure 1-5C)

   Local anchoring plays an important role in most RNA localization pathway, as diffusion would otherwise eventually negate the achieved localization. However, certain RNAs are localized in the absence of directed transport purely by local tethering or protection. Their mobility can either result from passive diffusion [268], or when this is not sufficient, facilitated mixing via cytoskeleton- and motor-dependent cytoplasmic streaming [269]. Finally, active transport along an unpolarized cytoskeleton network can also result in net (semi-) random movement [270]. A well-studied example for diffusion and entrapment based localization is that of the translational regulator *nanos* at the posterior pole of *Drosophila* oocytes. Localization of *nanos* mRNPs does not absolutely depend on microtubules, although MT-based cytoplasmic streaming enhances its posterior enrichment [269]. The microfilament network however is crucial for the local entrapment of *nanos*, as actin depolymerization leads to detachment of large *nanos* aggregates from the oocyte posterior [269]. An example of random active transport and local anchorage is that of *bicoid*, in the same cellular system. Particularly late during oogenesis, its anterior enrichment is characterized by continuous dynein-mediated transport [271,272] along MTs and local entrapment [270]. Although the transport of *bicoid* RNPs is slightly biased towards the anterior, *bicoid* localization remains unchanged if MT polarization is artificially negated [270]. *bicoid* anchoring does not appear to rely on MT or F-actin integrity [270] but is likely based on sequestration of *bicoid* mRNA into P bodies/sponge bodies [273]. In addition to F-actin and retention in cellular granules such as P bodies, the conversion of

molecular motors to static anchors at the destination constitutes another common anchoring mechanism [274].

Instead of local anchoring, distinct RNA localization arising from random movements can also be achieved via broad degradation and localized protection. Such a mechanism is employed during the posterior localization of *Hsp38* mRNA in *Drosophila* embryos. Here, enrichment is achieved by local shielding of an otherwise exposed destabilizing sequence within the RNA [275] coupled with enhanced degradation elsewhere in the cytoplasm [276].

4. **RNA-independent tethering via ribosome-nascent chain complex** (RNC, Figure 1-5D)

   Unlike the previous examples, where RNA localization is initiated by a sequence element of the RNA molecule, often forming a certain secondary and tertiary structure, RNA-independent tethering relies on the affinity of the translated nascent chain to specific subcellular structures and as such, indirectly on the RNA primary structure.

   One of the most intensely studied examples for RNC-mediated localization is the co-translational association of secreted or transmembrane proteins (and therefore ribosomes and mRNAs) to the surface of the ER. In addition to previously described RNA-RBP mediated tethering [277], this can occur either via signal peptide binding to the ER translocon mediated by the signal recognition particle (SRP, reviewed in [278]) (Figure 1-5D), or via other less studied peptide-ER interactions [279]. Interestingly, the ER appears to constitute a more general translation-promoting environment that also recruits cytosolic and nuclear protein mRNAs onto its surface for translation [280]. This results in the characteristic 'rough' appearance of rough ER (rER) by decoration of translating polysomes and associated mRNAs. As parts of the ER and ER-derived vesicles are actively transported in many cells as described before, this might in fact constitute one of the anchoring mechanisms employed during organelle hitchhiking. Similar translation-dependent mRNA localization has been observed for the mitochondrial surface, arguing for widespread occurrence [281,282].

   Co-translational mRNA targeting is however not limited to membrane-bound organelles, although there are only a few counterexamples described so far. First, during poxviral infection of human cells, liquid/gel-like protein bodies called A-type inclusions (ATI) are formed by viral ATI protein and accumulate its own mRNA on its surface [283]. In line with co-translational association, this

accumulation is dependent on translation and sensitive to N-terminal truncations or pre-mature stop codons [283]. In another recent example, co-translational targeting of the pericentriolar matrix (PCM) protein Pericentrin, as well as the MT minus-end regulator ASPM mRNAs to the centrosomes is observed during mitotic entry in zebrafish embryos and human cells [284]. Disruption of polysomes via the translation inhibitor puromycin completely abolishes localization, but contrary to ATI, initial localization is dependent on MT-dependent transport via dynein [284]. It is proposed that co-translational transport and local RNC-mediated anchoring enables cells to deliver large quantities of Pericentrin to growing centrosomes within minutes despite the laborious synthesis of such a large protein. Finally, as a first example in budding yeast, distal pole localization of ABP140 mRNA is delivered by retrograde flow and locally anchored to actin cables via an N-terminal localization peptide [285]. As in previous cases, tethering is dependent on active translation and the protein coding sequence (CDS), while 5' and 3' untranslated regions (UTRs) are dispensable. Fittingly, the strength of mRNA enrichment is proportional to the length of the CDS following the N-terminal interaction domain, presumably by allowing more time for co-translational association [285].

More generally there have by now been several examples of co-localization between mRNAs and their protein products, and these cellular foci have alternatively been termed 'assembly factories', 'translation hotspots' or ' translation factories' [283,284,286–290]. These granules can further contain dedicated chaperones, presumably to aid in folding and complex assembly [287]. So far however the mechanism for RNA localization to many of these foci still remains to be identified.

The co-translational association or assembly of several protein subunits of the same protein complex constitutes a special scenario of RNC-mediated mRNA localization. While this often does not lead to asymmetric localization with reference to the cell, on a molecular level it nevertheless results in non-random distribution, co-localization or clustering of mRNA [287,291–293]. Indeed our current understanding and definition of RNA localization is rather coarse and largely based on localization to cellular landmarks such as organelles and specific cytoplasmic compartments. However, RNC-meditated tethering and co-translational association localize RNAs at a molecular scale and future studies will have to dive deeper into the specific localization of mRNAs with respect to each other and to its corresponding protein products.

1.2.1 Co-translational assembly

Intuitively, since a single mRNA molecule can be translated into many protein copies, the local clustering of mRNAs and coordinated co-translation would immediately place the proteins in close proximity, thus reducing diffusion-based stochasticity of assembly. This has indeed been proven to enhance assembly efficiency in the context of prokaryotic operons, where both protein subunit ORFs of bacterial luciferase are encoded on a single mRNA molecule [206]. For eukaryotic protein complexes, such direct evidence of enhanced assembly efficiency is still lacking. In addition to efficiency however, efficacy of assembly, i.e. how reliable a certain complex can be formed and how often it fails, is another crucial attribute. The combined cytosolic macromolecule concentration within *Escherichia coli* has been estimated around 300 – 400 mg/ml [294]. In such a crowded environment, nascent polypeptides are in constant competition for binding partners, which puts a tremendous toll on any cellular assembly and quality control system. For many complexes, stochastic assembly is nevertheless sufficient, as demonstrated by various *in vitro* assembly reactions [295]. For many others, the broad specificity chaperones provided by the cell are of sufficient assistance [296], while yet others evolved dedicated sets of personal chaperones [296] or even entire assembly organelles [297,298]. Yet in recent years, co-translational assembly has proven to fulfill a similar and sometimes complementary role for a growing number of cellular complexes. Initially identified for prokaryotic enzymes [299], this list was gradually extended to now include eukaryotic polymers (reviewed in [300]), membrane-embedded homo- and heteromers [301,302], and an ever growing number of soluble heteromeric complexes ([292,303–305], reviewed in [267,306]). Often in coordination with chaperones [304,307], co-translational interaction tends to prevent mis-assembly and aggregation [292,304,305,308].

New techniques such as selective ribosome profiling have further revealed that the onset of subunit association often corresponds directly with the emergence of the interaction domain from the ribosome tunnel [206,304]. Furthermore, co-translational binding can either occur symmetrically between two nascent chains [291,292] or directional with one mature and one immature subunit [304]. In terms of RNC localization, only the former case would result in co-localization between different mRNAs as well as translated proteins, whereas the latter would only show mRNA-protein co-localization. While mRNA localization and local translation can restrict the activity of an individual protein such as Oskar in time and space, local co-translational assembly can extend this concept towards protein complex activity. While members of the 20S core proteasome were found not to

be subject of co-translational assembly in yeast [304], several subunits of the 19S regulatory particle were found to assemble in this way in independent studies both in budding yeast [291] and fission yeast [303]. When probed in human cells, the mRNAs of RPT1 and RPT2 co-localized within cytosolic particles induced upon arsenite stress [291]. Such local assembly might be of particular importance for proteins with delicate activities. Perhaps because the unrestricted and untimely activity of these proteins would be detrimental for the cell, both the Cdk-protein Cdc2 [303] as well as the caspase-activated DNase CAD [307] were found to bind their corresponding inhibitors co-translationally. It is conceivable that local co-translation and co-translational assembly provides a spatial cue, thus seeding subsequent complex maturation.

While the mRNA localization of *nucleoporins* has, to the best of my knowledge, not been systematically tested, one fission yeast nucleoporin Nup211 (homolog of human TPR) has indeed been found to self-associate with its own RNC after translation termination (by immunoprecipitation via its C-terminus) [303]. This would be in line with the reported structure of its human homolog TPR, which forms a long, N-terminal, homo-dimeric coiled-coil domain [309] that could well be formed co-translationally.

1.3 Early *Drosophila melanogaster* development

Drosophila melanogaster, commonly known as fruit fly, has been a long-established model system for many biological research questions including apoptosis, genetics, development and RNA localization. Particularly the early developmental stages of oogenesis and embryogenesis serve as models for RNA transport and localization due to their reliance on several key morphogenic mRNAs. *D.m.* ovaries follow a telotrophic meroistic organization, where support cells (here called nurse cells) are directly connected to the growing oocyte (Figure 1-6) and deliver mRNAs, proteins and other material to it, while the oocyte nucleus is transcriptionally silent (reviewed in [310]). Each of the two ovaries is divided into 16 – 20 individual units called ovarioles, which represent strings of various developmental stages surrounded by an epithelial muscle sheath (Figure 1-6, [311]). Each ovariole contains its own stem cell population, embedded within the so-called germarium followed by several egg chambers containing nurse cells, somatic follicle cells and the oocyte at different stages. In the germarium, germline and follicle stem cells continually give rise to nurse cells, oocytes, and follicle cells. Here, a differentiated germline stem cell (cystoblast) divides four times resulting in 16 inter-connected sister cells via incomplete cytokinesis. Cellular bridges that are left behind develop into so-called ring canals, connecting nurse cells and oocyte (reviewed in [310]). These connections are initially established via a specialized membranous organelle called fusome and later stabilized by actin filaments and accessory proteins (reviewed in [312]). The future oocyte is chosen early on during the first cystoblast division in an act of stereotypic symmetry breaking and accumulates early oogenetic marker RNAs and proteins. As during the remainder of oogenesis, an intact, polarized MT network is important for proper oocyte differentiation early on.

The different cell types within *D.m.* egg chambers display different cell cycle stages throughout oogenesis. Nurse and follicle cells undergo so-called endocycles, which are characterized by DNA synthesis and immediate gap phases without mitosis (reviewed in [313]). This results in genome amplification, which is important for their respective functions in producing lots of RNA and protein for delivery to the oocyte, and producing egg shell components and other signaling molecules [314]. The oocyte on the other hand is arrested in meiosis I prophase already in the germarium. At stage 13, this arrest is lifted and the oocyte progresses into meiosis I metaphase, where it is again arrested until egg activation (reviewed in [313]).

Oogenesis can be divided into 14 morphological stages (Figure 1-6) developing over the course of 7 – 8 days. During this time, the oocyte consistently grows in size and remains encircled by follicle cells that contribute crucially to its axis determination. Starting at stage 9, follicle cells differentiate into three distinct populations: A set of 6 – 10 anterior follicle cells (called border cells) start migrating through the nurse cells towards the oocyte. Of the remaining follicle cells, another set of ~50 anterior cells undergo flattening and eventually cover the nurse cells as so-called squamous follicle cells, whereas the remaining posterior cells assume a columnar shape and cover the oocyte. Later on, these cells will secrete the components for both vitelline membrane as well as the eggshell and are further important in proper axis determination (reviewed in [315]). At stage 11, nurse cells will actively and rapidly contract in a process called nurse cell dumping, thereby expelling their content into the oocyte and undergo cell death (reviewed in [316]).

The oocyte then matures into the egg, which is activated via mechanically induced calcium signaling during its passage through the oviduct. This activation mechanism triggers completion of meiosis, as well as swelling and cytoskeletal reorganization (reviewed in [317]). The activated egg is then fertilized and the merger of maternal and parental genomes is completed with the first mitotic division. In the following early hours of embryogenesis, the embryo undergoes a series of 13 rapid, synchronous nuclear divisions within a common cytoplasm (called syncytium) to arrive at ~6,000 nuclei within ~2 hours (reviewed in [317]). The zygotic genome is largely transcriptionally silent throughout this process, which is driven by maternally contributed material. Subsequently, cellularization occurs by enclosing the cortically aligned somatic nuclei within plasma membrane invaginations, thereby forming the first epithelial cell layer. The embryo then enters gastrulation, which is concurrent with large-scale transcriptional onset of the zygotic genome (reviewed in [317]).

How the large amounts of maternally provided macromolecules are produced and stored during oogenesis is a matter of active interest. Since *D.m.* embryos have previously been shown to utilize stockpiled arrays of cytoplasmic ALPCs [84] to fuel their rapid nuclear divisions, these also presumably need to be made in the growing oocyte, where the final products were indeed identified before [318]. While certain potential steps of AL assembly have been morphologically described during *D.m.* spermatogenesis [191] and in other oocytes [188], no detailed knowledge about its mechanism is currently available for any system. The absence of a nuclear compartment as spatial cue and an arrested cell cycle as temporal cue necessitates an alternative assembly mechanism to the previously

described modalities at the nuclear envelope. *Drosophila* oogenesis is thus an idea model system to study the molecular mechanisms of ALPC assembly for several reasons:

1. The need to produce and stockpile large amounts of ALPCs within a defined time window for subsequent embryonic divisions
2. *D.m.* egg chambers are a well-established model system for RNA localization and transport, where many of the factors involved have been identified
3. *D.m.* oocytes are very large cells (stage 14: ~250 µm anterior-posterior, ~90 µm dorsal-ventral), thus making diffusion-mediated complex assembly more challenging (refer to Section mRNA localization and local translation).
4. Each individual ovariole harbors an inherent snapshot of oogenetic progression by combining egg chambers of several distinct developmental stages (Figure 1-6)
5. Oogenesis occurs within an intact living animal with accessible genetics and associated phenotypic readouts

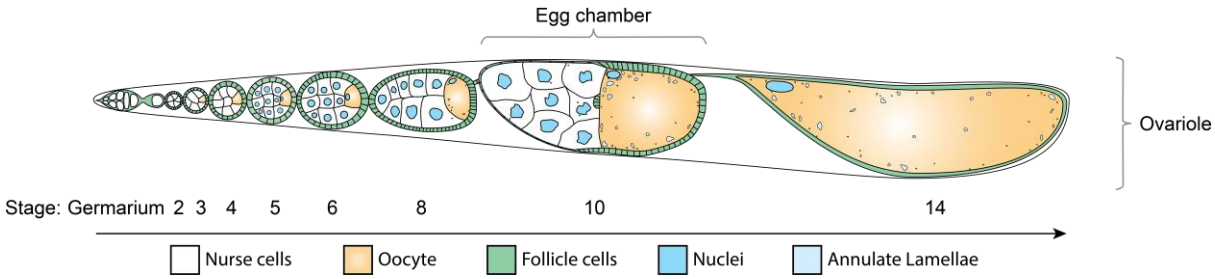

Figure 1-6: Schematic of *Drosophila melanogaster* oogenesis
Depicted is a cartoon representation of a single ovariole containing a germarium and eight egg chambers of various developmental stages from anterior (left) to posterior (right). The anterior germarium contains follicle stem cells and germline stem cells, as well as differentiated cystoblasts giving rise to individual egg chambers. Each egg chamber consists of 16 inter-connected germline sister cells divided into 15 nurse cells (white) and one oocyte (yellow-orange) with their respective nuclei (light and medium blue), surrounded by a layer of somatic follicle cells (green). Nurse cells and oocytes are connected via cytoplasmic bridges called ring canals. Both nurse cells and follicle cells are polyploid. The oocyte nucleus is arrested in meiosis I throughout oogenesis. At stage 11, nurse cells expel their cytoplasm into the oocyte and undergo cell death.

1.4 Objectives

Any assembly mechanism is by definition transitory and therefore often both short-lived as compared to the lifetime of its product, and consequently rare. In addition, the assembly of many protein complexes is either stochastic or induced upon unknown or uncontrollable cues. For NPC assembly, major advances in describing its sequence were made either by obtaining control over its composition and initiation using the reconstituted *Xenopus laevis* egg extract system [137,157,170,319], or by precise temporal staging of the cell cycle combined with correlative microscopy data acquisition [165,175]. The second prominet location of pore complexes, within cytoplasmic AL, has received less attention despite being abundant in many cell types, and should display at least partially distinct rules due to the lack of a nuclear compartment. Finally, while local translation has been recognized to participate in a number of cellular processes including complex assembly, its possible involvement in NPC/ALPC assembly has not been addressed thus far.

I believe that *D.m.* oogenesis represents a cellular system, within a living animal, where large amounts of NPCs should be assembled at defined temporal stages, specifically within the oocyte. In addition, due to its unusually large size and polarization, local translation could be of particular importance during the assembly of its large heteromeric complexes. I thus propose the following objectives for my PhD work:

1. To establish whether ALPCs are assembled during *D.m.* oogenesis
2. To probe whether NPC and ALPC assembly follow identical rules and what adaptations were made to accommodate ALPC assembly in the absence of a nuclear compartment.
3. To probe whether mRNA localization and local translation are involved in ALPC or NPC assembly within this system.

2 Results

The data and analyses described throughout this thesis were produced in close collaboration with Dr. Bernhard Hampoelz, postdoctoral fellow in our laboratory, as well as Dr. Paolo Ronchi, scientist in the EMBL Electron Microscopy Core Facility (EMCF). It is thus stated in the figure legend and occasionally the main text wherever data is displayed that was not produced by myself.

2.1 Ultrastructural characterization of Annulate Lamellae and accumulation during oogenesis

Annulate Lamellae were previously shown to be present in large numbers within *Drosophila* syncytial embryos, and to contribute substantially to the rapid nuclear growth during early embryogenesis by insertion into the nuclear membrane [84]. Furthermore, it is well-described that the majority of gene products within the early embryo are provided maternally as the zygotic genome generally lies dormant prior to zygotic genome activation [320]. It was thus a logical assumption that AL assembly might take place within the oocyte. Consistently, previous work had indeed identified AL within *Drosophila* oocytes [318]. In order to first confirm the presence of these structures in our specimen, and establish a protocol to consistently visualize them, I dissected several stage 10 egg chambers from wild type *D.m.* flies and subjected them to high pressure freezing together with Dr. Paolo Ronchi (EMCF). After freeze substitution, resin embedding and ultramicrotome sectioning, thin sections of ooplasm were imaged via transmission electron microscopy (TEM) and revealed a high density of characteristic AL membrane structures (Figure 2-1A).

In order to confirm the molecular identity of nucleoporins as constituents of ooplasmic AL, several stage 9 – 10b egg chambers dissected from flies expressing a fluorescently labeled scaffold nucleoporin (*RFP::Nup107*) were subjected to the same sample preparation protocol. Subsequent correlative light and electron microscopy indeed confirmed its localization to ooplasmic AL (Figure 2-1B-C') as previously also shown in embryos [84].

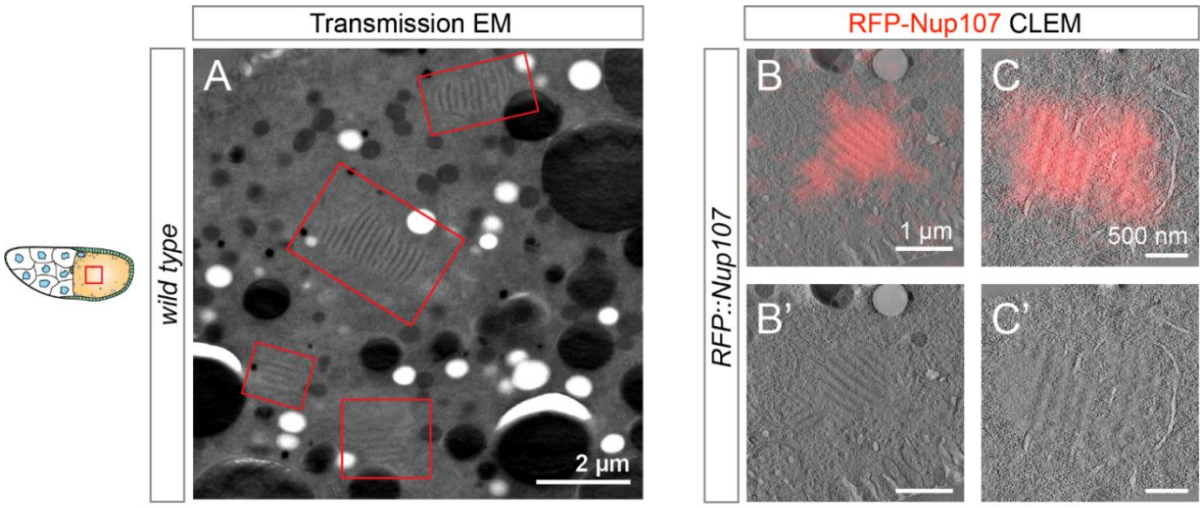

Figure 2-1: Transmission EM of *D.m.* ooplasm and localization of RFP-Nup107 signal to Annulate Lamellae
(A) Transmission electron microscopy (TEM) of a 200 nm section of resin-embedded late stage ooplasm. Several multi-sheet Annulate Lamellae (AL, red rectangles) are visible throughout the ooplasm, which is otherwise mostly inhabited by large yolk granules (black), mitochondria (dark grey) and lipid droplets (white). **(B-C")** RFP-Nup107 is enriched at AL. Correlative light and electron microscopy (CLEM) overlays of RFP-Nup107 fluorescence (B, C) with TEM images of late stage *RFP::Nup107* ooplasm showing multi-sheet AL (B', C'). Data was produced jointly with Dr. Paolo Ronchi.

While these initial experiments were performed in oocytes at mid to late oogenesis (Figure 1-6), biosynthesis of AL might occur at any point throughout this process. Conveniently, ovarioles of *D.m.* house a sequence of egg chambers at different developmental stages, representing an inherent timeline Figure 1-6. In order to monitor a potential accumulation of AL throughout oogenesis, Dr. Bernhard Hampoelz in parallel performed live cell imaging and image quantification of cultured egg chambers, dissected from the same *RFP::Nup107* transgenic flies. At several distinct stages, RFP-Nup107 signal intensity was quantified throughout the nurse cell and oocytic compartments respectively, and revealed a steep increase in the oocyte over developmental time (Figure 2-2A, red arrowheads; Figure 2-2B). In contrast, within the nurse cells, signal increased much more slowly (Figure 2-2B) and was largely restricted to nuclear envelopes, even at later stages (Figure 2-2A, yellow arrowheads). Thus, I conclude that the growing oocyte accumulates cytoplasmic Annulate Lamellae as defined by its pore-embedded, stacked sheet morphology and the presence of RFP-Nup107, whereas there is no corresponding accumulation in the nurse cell cytoplasm.

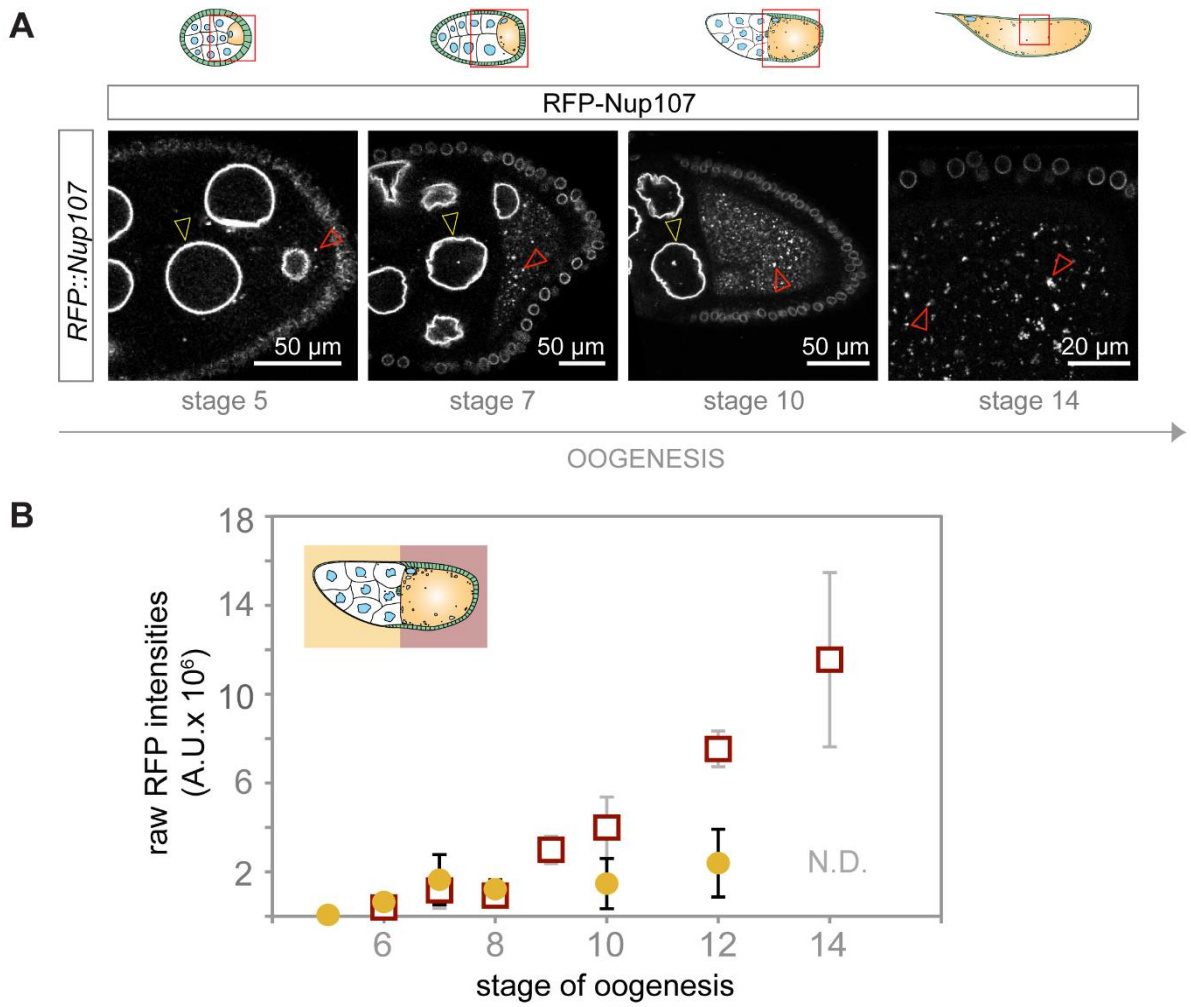

Figure 2-2: Annulate Lamellae are gradually enriched during oogenesis
(A) Snapshots of increasing developmental stages shows an increasing amount of RFP-Nup107 structures in the ooplasm. Single slices of confocal volume imaging through fixed *RFP::Nup107* egg chambers at stages 5, 7, 10 and 14. Whereas RFP-Nup107 signal within nurse cells is largely restricted to nuclear envelopes (yellow arrowheads), it is detected at both nuclei and cytoplasmic foci (red arrowhead) within the oocyte. **(B)** Quantification of RFP-Nup107 accumulation across compartments. Raw integrated RFP intensity (± SD) is measured across several nurse cells (yellow) and oocytes (red) and plotted as a function of its corresponding stage. Around stage 11, nurse cells expel their cytoplasmic content into the oocyte in a process called 'nurse cell dumping' and subsequently undergo cell death (N.D.) (n = 23 egg chambers). Data was produced by Dr. Bernhard Hampoelz.

While tomography of the aforementioned sections had provided some measure of three-dimensional information about AL, this was restricted to the section thickness (~200 nm), which is far lower than the dimensions of larger AL. To circumvent this issue and generate both a more holistic census of AL abundance as well as a three-dimensional representation of AL ultrastructure, several *wild type* stage 10 egg chambers were subjected to 3D EM via Focused Ion Beam milling and Scanning Electron Microscopy (FIB-SEM) in our EMCF. This resulted in a dataset covering ~1,200 µm^3 of ooplasm with 5 nm isotropic resolution (Figure 2-3A). Within this volume, automated detection implemented by the EMCF team member Helena Bragulat Teixidor identified a total of

45 Annulate Lamellae, which were divided into 25 (~56%) AL with a single membrane sheet, 9 (20%) AL with two sheets and 11 (~24%) AL with three sheets or more (Figure 2-3A'). Manual inspection of automatically identified AL confirmed their correct classification. This automatic segmentation revealed many AL that certainly would have been missed by a manual search, particularly for small AL that were oriented parallel or at a shallow angle to the viewing direction. As the majority of our current understanding of AL architecture is based on manual inspection of 2D TEM images, our stereotypical idea of AL as large parallel membrane stacks is thus likely the result of a strong identification bias – at least in oocytes.

Isosurface rendering of two segmented multi-sheet AL from this dataset are depicted in Figure 2-3B-C" and reveal an elaborate membrane topology of the parallel AL sheets embedded within the rough ER (rER) (Figure 2-3B-C"). ALPC-containing sheets display a near perfect parallel arrangement and are connected and partially shielded by rER sheets in consecutive three-way junctions (Figure 2-3B", arrowheads). This arrangement is markedly different from the proposed 'parking garage' model for stacked ER sheets, where one continuous sheet is wound around a central axis [321]. It is however reminiscent of the thylakoid organization in plants, where stroma thylakoids connect several grana thylakoids via junctional connections [322]. Such an arrangement leaves certain regions within the AL shielded, and others exposed to the cytoplasm.

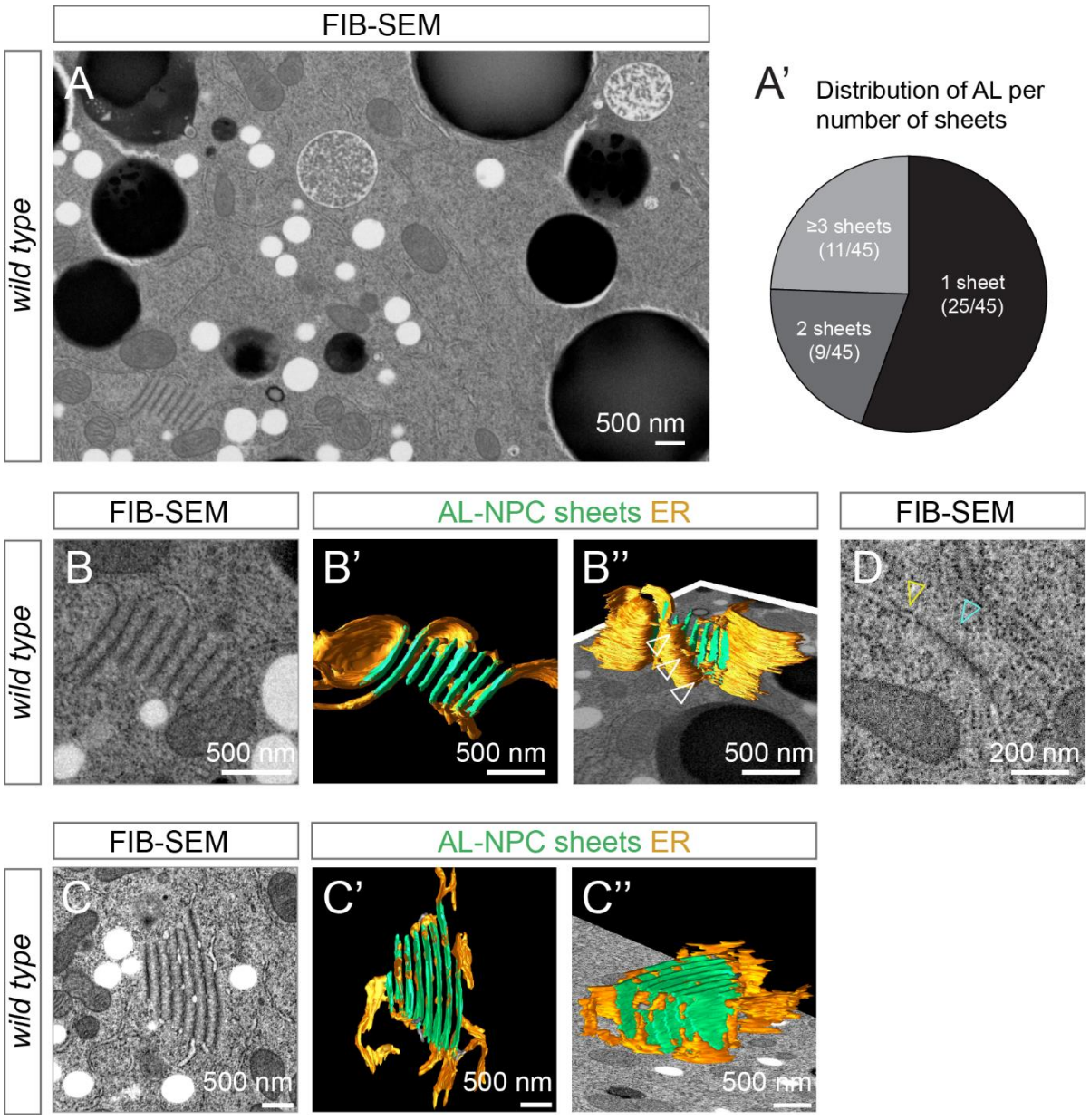

Figure 2-3: Annulate Lamellae distribution and 3D ultrastructural characterization across the ooplasm

(A-A') Annulate Lamellae can be automatically identified and exist mainly as arrangements of a single or two sheets. (A) A representative single slice of an acquired EM volume produced via Focused Ion Beam milling and Scanning Electron Microscopy (FIB-SEM) is displayed, showing many cellular organelles as well as one prominent multi-sheet AL (bottom left). The dataset covers a single ~1,200 μm^3 volume near the cortex of a *wild type* stage 10 oocyte. (A') Automatic identification of 45 AL revealed that the majority of AL at this stage only contain a single (25/45) or two (9/45) sheets, and only ~24% (11/45) consist of 3 or more. **(B-C")** Multi-sheet AL are arranged as parallel stacks of membrane, embedded within the endoplasmic reticulum. Two representative multi-sheet AL (B, C) were subjected to segmentation and 3D isosurface rendering (B'-B", C'-C") and show the partial shielding of AL sheets by the ER and partial exposure to the cytoplasm. Individual sheets are typically continuous on either side with the ER and are often inter-connected via three-way junctions (B", arrowheads). **(D)** Single-sheet AL display a clear surrounding ribosome exclusion zone to all sides. While ribosomes (small, black structures) are abundant in the cytosol and directly attached to adjacent rough ER (yellow arrowhead), they are excluded within a zone of ~70 nm extending evenly to all sides of the AL. Data was acquired by Dr. Paolo Ronchi and automatic AL identification/segmentation was performed by Helena Bragulat-Teixidor, both members of the EMCF.

A common feature of AL containing any number of sheets is the exclusion of cytoplasmic constituents such as organelles and ribosomes (Figure 2-1B-C', Figure 2-3B-D). Whereas the surrounding cytoplasm is filled, and adjacent rER sheets are decorated with ribosomes (Figure 2-3D, yellow arrowhead), the part of each membrane sheet carrying the characteristic high staining density of ALPCs displays a clear exclusion zone around it extending to all sides. This is particularly apparent in single-sheet AL (Figure 2-3D, cyan arrowhead). While this exclusion zone appeared to be highly stereotypical and of consistent size for most AL, EM guided by fluorescence further identified a population of RFP-Nup107 positive structures that showed an adjacent exclusion zone that was many times larger and circular in thin sections (Figure 2-4A-C'). Also here, RFP-Nup107 still decorated an internal membrane that was continuous with rER, but it was absent from the remaining amorphous zone. This second population of ALPC-containing structures will be discussed more extensively later on.

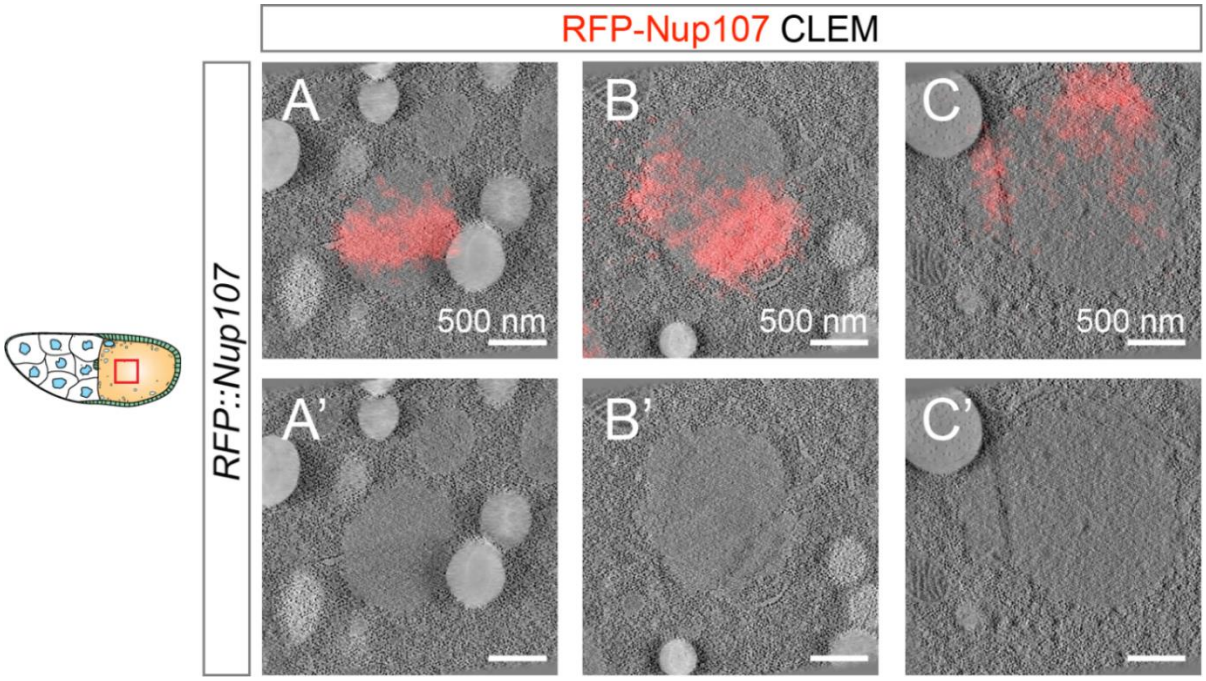

Figure 2-4: Presence of ALPC-containing membrane sheets with extended exclusion zone
Correlative light and electron microscopy (CLEM) overlays revealed the existence of several RFP-Nup107 positive structures with distinct morphology to AL. Whereas RFP-Nup107 is located to internal membrane structures of identical staining pattern as AL sheets, the surrounding circular exclusion zone is extended as compared to AL (compare to Figure 2-1) and devoid of RFP-Nup107.

2.2 Systematic investigation of mRNAs encoding nucleoporins and related factors

Having characterized the presence, molecular identity, architecture, and time-dependent accumulation of AL within the *Drosophila* egg chamber, I next turned to my proposed objective to systematically probe the localization of *nucleoporin* mRNAs. For this, I designed short DNA oligonucleotide probes complementary to all nucleoporin-encoding transcripts. Via enzymatic labeling [220], I first attached either Atto565 or Atto633-conjugated ddUTP to the 3' ends of two alternating, non-overlapping probe sets per mRNA target. Each resulting single-molecule fluorescence *in situ* hybridization (smFISH) probe set was then validated by co-hybridization of both subsets to the same specimen, followed by imaging, automatic detection of smFISH spots, and co-localization analysis (Suppl. Figure 1). The detected fluorescence intensity in a reference channel was plotted as a function of intensity of the target channel and vice versa, which showed in a linear relationship of smFISH intensities of both sub-sets (Suppl. Figure 1B). With the exception of *sec13* and *nup107*, all transcripts passed this quality assessment and typically displayed co-localization of >90%. I then systematically screened the localization of 39 mRNAs encoding nucleoporins, as well as NTRs, and Ran cycle related proteins (Figure 2-5). To gain an overview over this relatively comprehensive dataset, Figure 2-5 displays a combined line intensity profile of both smFISH fluorescence channels across a single representative stage 10 egg chamber (Figure 2-5C) for each target transcript. While probe binding to the target is stochastic, labeling efficiency, probe number and background binding are not consistent across probe sets, and thus the intensity merely serves as a rough approximation of RNA expression. Centered around the nurse cell oocyte border, these profiles contain information about the rough abundance (amplitude), homogeneity of RNA distribution (fluctuation of signal, e.g. comparing *pendulin* to *moleskin*), as well as cellular distribution (e.g. comparing *pendulin* left to right side). Additional qualitative descriptors summarize the visual inspection of each mRNA localization (Figure 2-5C, right column). While the majority of transcripts displayed a rather homogenous distribution and relatively low abundance across the egg chamber (e.g. all Y-complex members) (Figure 2-5C, Figure 2-6A-A'), certain mRNAs showed a clear enrichment either to subcellular structures (Figure 2-5C, 'NE/AL', 'ER') as confirmed by individual co-staining experiments (Figure 2-6B, Figure 2-7), or to the growing oocyte (Figure 2-5C, 'oocyte enriched early').

A

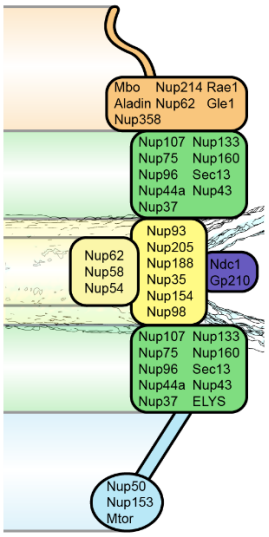

B

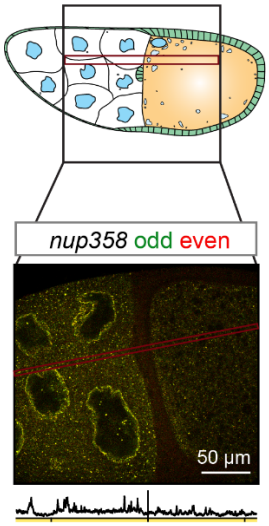

C

	transcript	intensity line profile	comments
Cytoplasmic filaments	*nup358*		NE/AL
	nup214		homogenous
	aladin		homogenous
	mbo (nup88)		homogenous
Y-complex	*nup160*		homogenous, oocyte enriched early
	nup75 (nup85)		homogenous
	nup133		homogenous
	nup37		homogenous
	nup43		homogenous
	nup98-96		homogenous
	nup44a (seh1)		homogenous
	elys		homogenous
Inner ring	*nup93.1*		homogenous
	nup154 (nup155)		homogenous
	nup205		homogenous, slight NE enrichment
	nup35		homogenous
	nup188		homogenous
Central channel	*nup62*		homogenous
	nup54		homogenous
	nup58		homogenous
Nuclear basket	*mtor (tpr)*		granular, slight NE enrichment
	nup153		NE/AL
	nup50		homogenous, slight NE enrichment
TM nups	*ndc1*		ER
	gp210		slight NE, oocyte enriched early
Nuclear transport receptors	*ketel (importin β)*		NE/AL, oocyte enriched early
	karyopherin β3		NE/AL
	moleskin (importin 7)		NE/AL, oocyte enriched early
	importin β11		homogenous
	cadmus (importin 13)		homogenous
	transportin		homogenous
	transportin-SR		homogenous
	embargoed (crm1)		homogenous, oocyte enriched early
	karyopherin α1		homogenous, oocyte enriched early
	pendulin (karyopherin α2)		homogenous
	ntf2		homogenous
Ran cycle	*ran*		homogenous
	ranGAP		homogenous
	bj1 (rcc1)		homogenous, oocyte enriched early

Figure 2-5 Systematic visualization of 39 nucleoporin, Ran cycle and NTR-encoding mRNAs across *D.m.* egg chambers

(A) Schematic depiction of *D.m.* nucleoporins and their (presumed) location within the NPC. **(B)** Example smFISH imaging data of *nup358* mRNA distribution and corresponding intensity line

profiles. Depicted is a single confocal slice acquired for two non-overlapping smFISH probe subsets (odd/even) conjugated to Atto633 and Atto565 respectively, acquired at constant microscope settings between probe sets, and displayed as composite image. Intensity line profiles (avg. over 18 pixels) are measured from anterior (left) to posterior (right), crossing a single nurse cell nucleus, and centered around the nurse cell – oocyte border. **(C)** Overview over all measured smFISH intensity line profiles representing mRNA localizations. The x-axis represents the distance in µm from anterior to posterior with 100 µm ticks, centered around the nurse cell – oocyte border. The y-axis represents combined two-channel intensity in arbitrary units from 0 to 130. Due to its strong peak enrichment, the y-axis for *moleskin* was trimmed at 130 for better visualization across all transcripts. Most transcripts display homogenous distributions throughout the egg chamber, but certain transcripts such as *nup358, nup153, ndc1, ketel, karyopherin β3,* and *moleskin* show distinct localization to either the nuclear envelope, Annulate Lamellae, or the endoplasmic reticulum. The last row indicates qualitative descriptors of observed localization. 'NE/AL' = enriched around Nuclear Envelope or Annulate Lamellae, 'ER' = enriched around the endoplasmic reticulum, 'oocyte enriched early' refers to oocyte enrichment during early developmental stages.

Multicolor imaging of *nucleoporin* smFISH probes in egg chambers expressing *Rtnl1::GFP*, which serves as an ER marker, showed a strong co-localization of the transmembrane nucleoporin-encoding *ndc1* mRNA with the ER, but not of the inner ring nucleoporin-encoding, soluble *nup35* (Figure 2-6B).

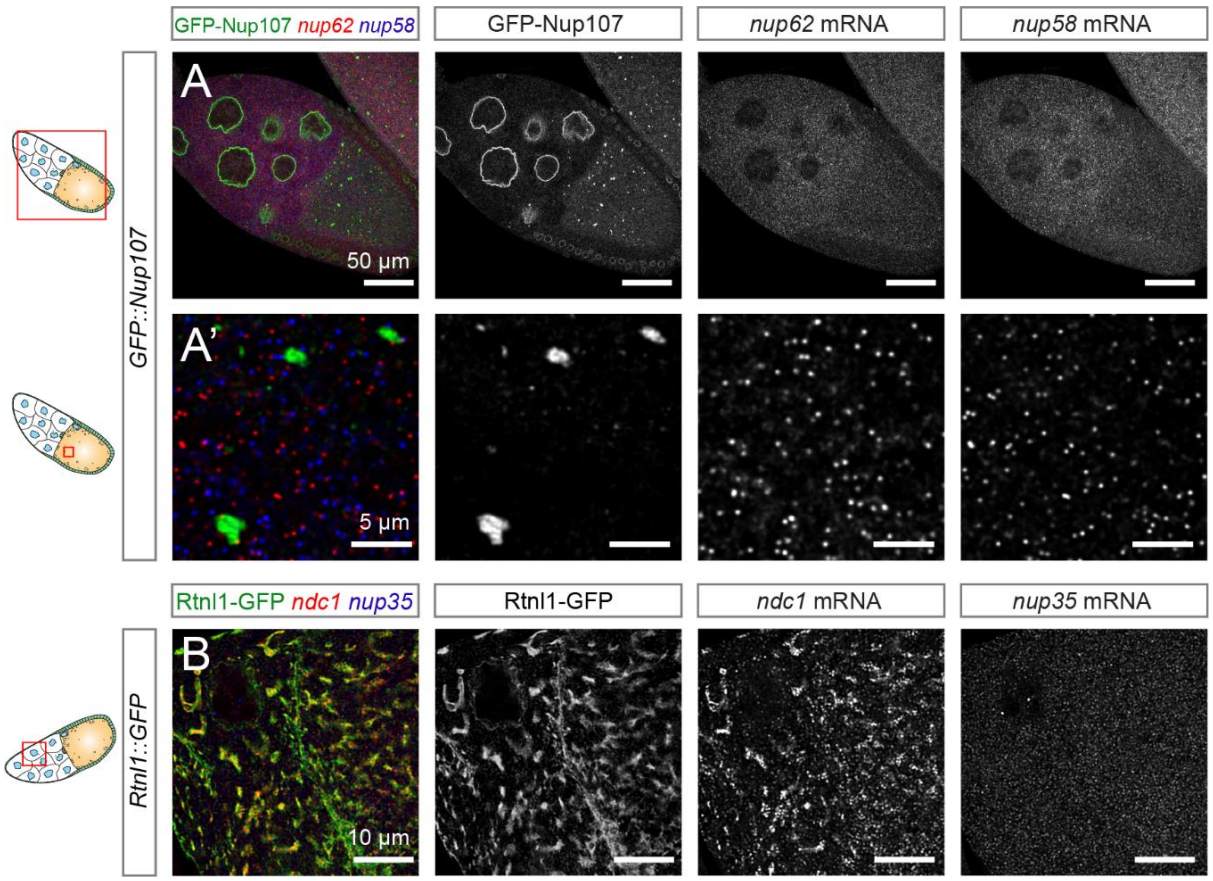

Figure 2-6: Homogenous distribution of *nup62/nup58,* and ER enrichment of *ndc1* but not *nup35*

(A) The two inner ring nucleoporin transcripts *nup62* and *nup58* are evenly distributed throughout nurse cell and oocyte cytoplasm. Low (A) and high (A') magnification confocal images of smFISH

hybridization in *GFP::Nup107* egg chambers shows decreased fluorescence signal within nuclei and follicle cells, but homogenous distribution within nurse cell and oocyte cytoplasm. No obvious clustering or co-localization was observed either with each other or with GFP-Nup107 positive structures (A'). **(B)** The transmembrane nucleoporin transcript *ndc1*, but not the inner ring component *nup35* shows strong enrichment at the endoplasmic reticulum (ER). High magnification confocal images of *ndc1/nup35* smFISH hybridization in *Rtnl1::GFP* egg chambers. Rtnl1-GFP serves as an ER marker and shows strong co-localization with *ndc1* but not with *nup35*.

Finally, a small subset of *nucleoporin* mRNAs including *nup358, nup205, mtor, nup50, nup153,* and *gp210* as well as the importin ß family NTR transcripts *ketel* (homologous to *importin β*), *moleskin* (homologous to *importin-7/8*) and *karyopherin β3* (homologous to *importin-5*) displayed variable enrichment towards the nuclear envelope and occasionally AL (Figure 2-5C). As the main goal of this smFISH-based RNA localization screen was to probe a potential role of local translation in NPC assembly, both of these identified localizations to NPC-containing structures was of particular interest to me and its characterization was henceforth the main focus of further experiments.

2.2.1 Characterization of *nucleoporin/importin* mRNA localization to different nucleoporin structures

Multicolor fluorescence imaging of these transcripts in *GFP::Nup107* egg chambers confirmed the strong enrichment of *nup153*, *nup358*, *ketel*, and *moleskin* not only to the NE (Figure 2-7A, C, D), but additionally to GFP-Nup107 positive cytoplasmic structures in both nurse cells (Figure 2-7A', C', D') and oocytes (Figure 2-7A", C", D"). In both compartments the mRNAs clearly accumulated around the surface of these structures and did not penetrate it. Whereas in oocytes these structures appeared to be entirely filled with GFP-Nup107 however (Figure 2-7A", C", D", E" arrowheads), in nurse cells the inner GFP-Nup107 accumulation was weaker and sometimes barely noticable (Figure 2-7A', C', D', E', arrowheads). In contrast to the surrounding cytoplasm, where all smFISH spots appeared homogenously distributed and of uniform brightness, around GFP-Nup107 all five observed RNAs clustered into larger assemblies that could not be further resolved by confocal microscopy (Figure 2-7A'-A", C'-C", D'-D", E'-E"). *karyopherin β3* localization was generally weaker than that of the other *importin* transcripts (Figure 2-7E-E"), and the even weaker localizations of *nup205*, *mtor*, *nup50*, *nup153* and *gp210* were subject to strong variability and could not consistently be observed across several experiments. For *nup153*, *nup358*, *ketel*, and *moleskin*, image analysis of mRNA enrichment around GFP-Nup107 foci in both compartments quantified the significant enrichment of up to sevenfold (Figure 2-7B) compared to the surrounding cytoplasm. *nup214*, a homogenously

distributed and non-localized transcript served as a control and showed no such local concentration (Figure 2-7B). The enrichment of all observed mRNAs varied significantly between compartments. Whereas *nup153* was amongst the most concentrated transcripts within nurse cells (Figure 2-7A', B), its enrichment around ooplasmic GFP-Nup107 foci was only twice the basal level (Figure 2-7A", B). In contrast, *ketel* displayed a stronger enrichment within the oocyte (Figure 2-7B, C") as compared to nurse cells (Figure 2-7B, C'). Such differential recruitment towards GFP-Nup107 positive structures is indicative of local regulation of RNA localization and warranted further examination of its mechanism.

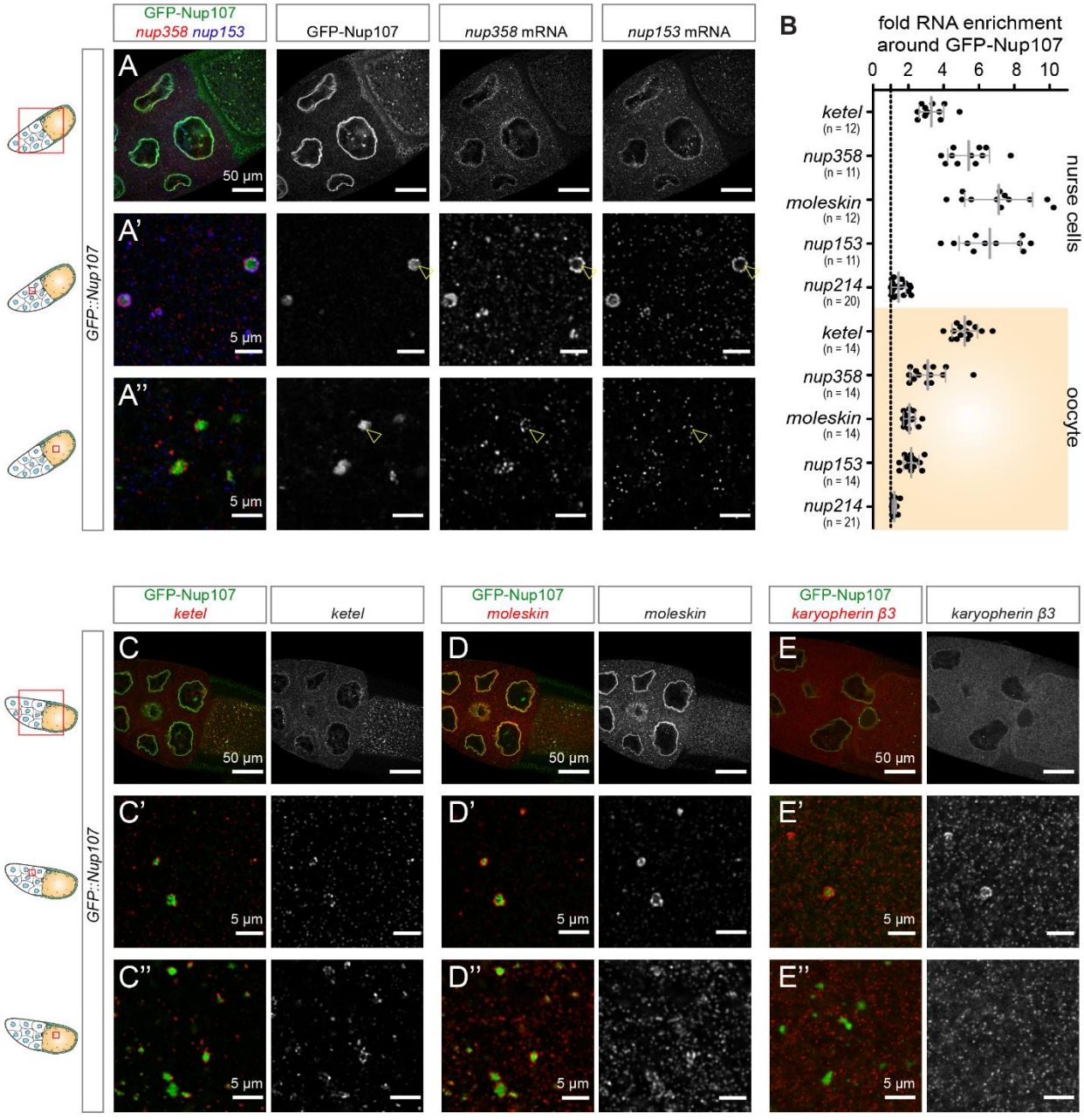

Figure 2-7: A specific set of *nucleoporin* and *importin* mRNAs are enriched around nucleoporin-containing structures

(A-A") *nup153* and *nup358* transcripts localize to the NE and GFP-Nup107 positive structures in both nurse cell and oocyte cytoplasm. Single confocal images of *nup153/nup358* smFISH hybridization in *GFP::Nup107* egg chambers show clustering around NE (A), and to the surface of GFP-Nup107 foci in nurse cells (A') and oocytes (A"), but are markedly excluded from their interior (arrowheads). **(B)** Quantification of distinct mRNA enrichment factors across both compartments. Scores were calculated as the ratio between the measured integrated signal intensity within 400 nm surrounding GFP-Nup107 foci, as well as the remaining cytoplasm. Each depicted data point represents in itself an average of all such foci within the acquired volume. *nup214*, which showed no obvious enrichment in the initial screen served as a negative control. All four measured transcripts showed differential enrichment scores between the different compartments. **(C-E")** Three *importin* transcripts display similar localization patterns as *nup153/nup358*. As in (A-A"), images represent single confocal volumes of smFISH hybridization against *ketel* (C-C"), *moleskin* (D-D") and *karyopherin β3* (E-E") respectively. *ketel* and *moleskin* were acquired by co-hybridization within the same sample and thus show an identical egg chamber (C-D"). Whereas all three transcripts are strongly enriched around GFP-Nup107 foci in nurse cells (C', D', E'), *karyopherin β3* was only mildly localized at NE (E) and not noticeably enriched within oocytes (E"). In contrast, *ketel* (C-C") and *moleskin* (D-D") consistently showed strong GFP-Nup107 enrichments in all samples and compartments tested.

In order to probe the nature of this observed mRNA localization, I performed a series of pharmacological disruption experiments. In the *D.m.* egg chamber, several well-characterized RNA localization pathways – including that of the axis determinant *oskar* – are dependent on microtubule-based transport. I thus first examined whether *nucleoporin* and *importin* mRNA enrichments were sensitive to MT depolymerization by feeding female flies overnight with food containing the MT-depolymerizing agent colchicine, followed by dissection and smFISH hybridization of egg chambers. As reported previously [323], this treatment caused *oskar* to largely dissociate from the posterior end of the oocyte (Figure 2-8A'), but surprisingly had no detectable effect on either *nup358* or *ketel* mRNA localization (Figure 2-8A). While it is still possible that the MT network might be involved in the initial targeting of *nup358/ketel* mRNAs to their destination, at least its maintenance thus seems to function independently. As my initial hypothesis postulated an involvement of local translation in NPC assembly, I next turned to probe the importance of active translation. As expected, incubation of dissected egg chambers in culturing medium supplemented with the protein synthesis inhibitor puromycin for 15 min had no discernable effect on *oskar* posterior enrichment (Figure 2-8B'). As *oskar* is localized via local anchoring and continuous transport to the posterior, active translation is not thought to be required for its localization. In contrast, enrichment of both *nup358* and *ketel* was completely abolished (Figure 2-8B). A similar effect was noted for the remaining localized mRNAs *nup153* and *moleskin* (not shown). As mentioned previously, most RNA targeting mechanisms reported to date – including *oskar* – are dependent on sequence elements within the RNA and binding of specific RBPs to these elements, which typically renders them independent of translation. One possible explanation for the observed translation sensitivity of *nucleoporin/importin* transcripts however would be an

RNC-mediated localization mechanism, where the nascent chain interacts with its target and tethers its own mRNA via the translating ribosome. As long as translation rates are high, each terminating ribosome would constantly be replaced by a new nascent chain, produced by the next ribosome translating shortly after, thus reaching a steady state and remain attached. As puromycin disrupts polysomes and causes the dissociation of nascent peptide and mRNA, such localization would disappear accordingly. In such a model, the mere stalling of ribosomes, rather than their disruption, would preserve steady-state localization as the mRNA and nascent chain remain connected. Consistent with this, incubation of egg chambers with the elongation inhibitor cycloheximide (CHX) fully preserved both *oskar* and *nup358/ketel* localization (Figure 2-8C, C').

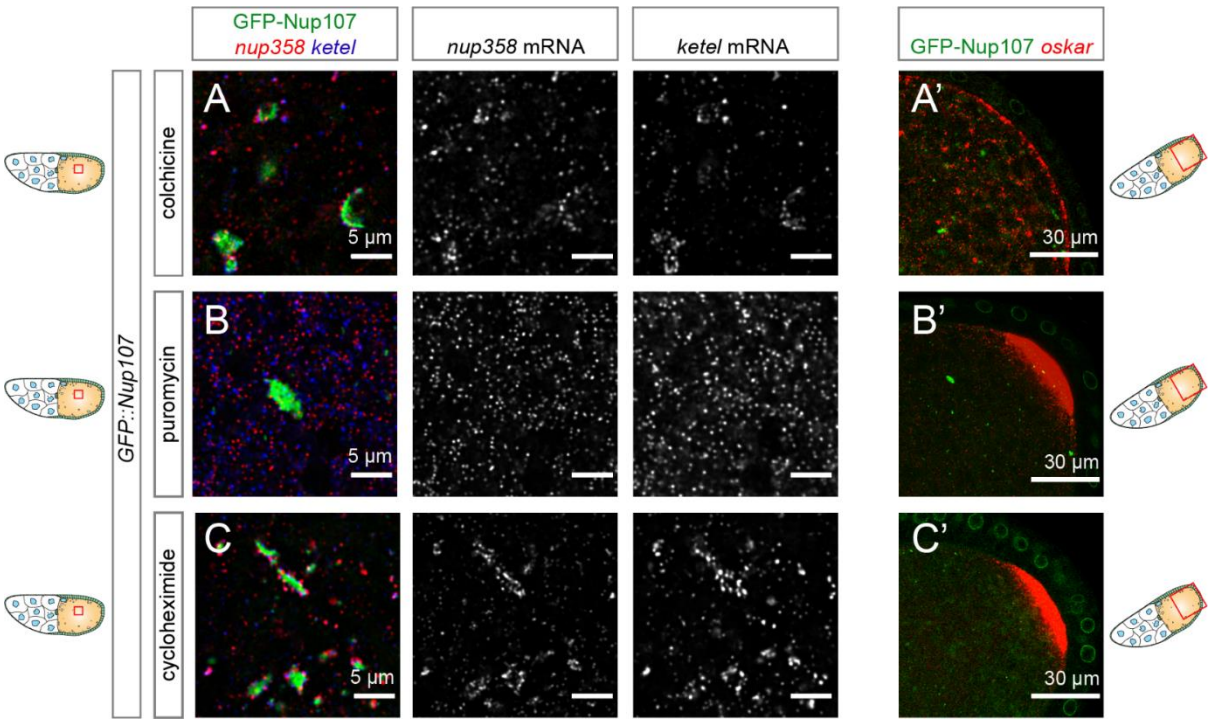

Figure 2-8: *nup358/ketel* mRNA localization is dependent on active translation but insensitive to translational stalling and depolymerization of microtubules
(A-A') Microtubule-depolymerization by colchicine disrupts *oskar* but not *nup358/ketel* localization. Single high magnification confocal images of smFISH hybridization in *GFP::Nup107* oocytes. Prior to dissection, flies were fed with yeast paste supplemented with 100 µg/ml colchicine in 1% sucrose for 16 h. While smFISH probes targeting *oskar* (A') showed the expected loss of posterior enrichment typical for microtubule disruption, *nup358/ketel* enrichment around GFP-Nup107 in the ooplasm was unaffected. **(B-B')** Premature chain termination by puromycin abolishes *nup358/ketel* but not *oskar* localization. As in (A-A'), but flies were fed regular food. Instead, dissected egg chambers were incubated in imaging medium supplemented with 200 µM puromycin for 15 min. **(C-C')** RNA localization of *oskar, nup358,* and *ketel* are all unaffected by translational stalling. As in (A-A'), but flies were fed regular food and instead dissected egg chambers were incubated in imaging medium supplemented with 100 µg/mL cycloheximide for 15 min.

Another prediction of the steady-state RNC-anchoring model is that specific inhibition of initiating ribosomes, while elongating ribosomes remain unaffected, would result in a

gradual decrease in RNA enrichment as the remaining ribosomes finish translation. Such a ribosome run-off experiment has previously been performed both as validation and to determine ORFs and translation rates in ribosome profiling and translation imaging studies [324,325]. I therefore initiated ribosome run-off in my imaging-based RNA localization assay by adding the specific initiation inhibitor homoharringtonine (HHT), followed by fixation of egg chambers at several time points after addition. Consistently, RNA enrichment of all three tested transcripts gradually decreased to zero over a period of 20 minutes for all observed locations (Figure 2-9A). This progressive loss of enrichment was abolished by simultaneous block of elongation using cycloheximide (Figure 2-9A). Assuming a similar elongation rate between transcripts within each compartment, run-off should further only depend on the length of each transcript's protein coding sequence. Indeed, comparison between the three tested transcripts consistently shows the slowest depletion rate for the longest *nup358* transcript, followed by *nup153,* and the shortest transcript *ketel* (Figure 2-9A-B).

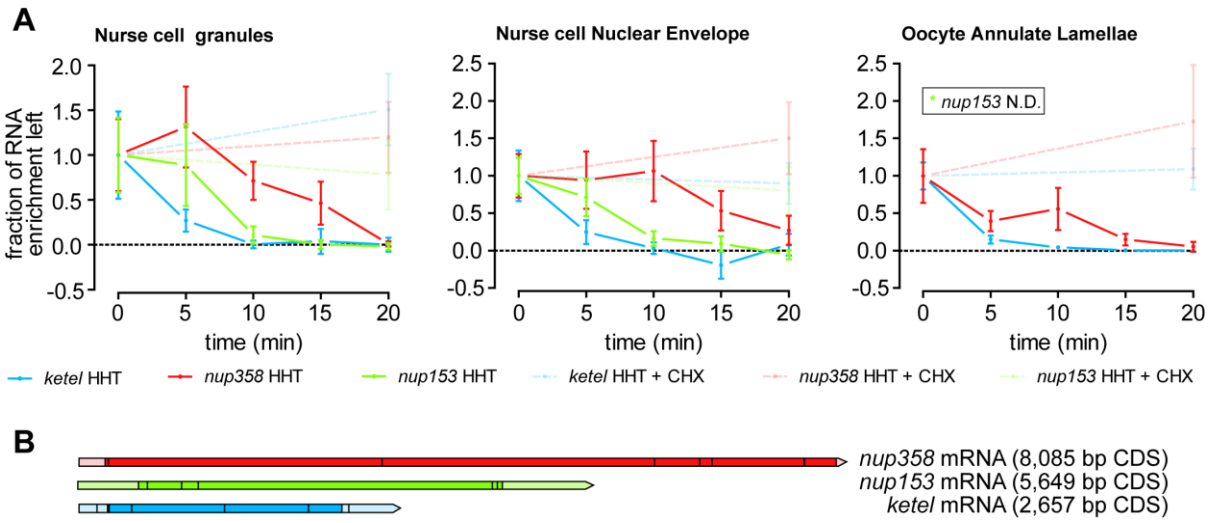

Figure 2-9 Ribosome run-off induces gradual loss of *nucleoporin/importin* mRNA enrichment proportional to their length
(A) Treatment of egg chambers with the translation initiation inhibitor homoharringtonine (HHT) led to a continual decrease of measured RNA enrichment. Egg chambers were either fixed immediately after dissection, or ribosome run-off was induced by incubation of dissected egg chambers in imaging medium supplemented with 5 µM HHT and stopped after 5, 10, 15, or 20 min by fixation. After smFISH hybridization and confocal imaging, mRNA enrichment scores around GFP-Nup107 structures in nurse cells, oocytes or the NE were measured as the average intensity within 400 nm around indicated structures relative to the average signal of the remaining cytoplasm, and normalized to t = 0 min. Values are displayed as mean ± SD. Analysis of *nup153* enrichment around oocyte structures was omitted as it did not display significant enrichment prior to treatment (N.D.). Concurrent addition of the elongation inhibitor cycloheximide (CHX) abolished the gradual decrease as measured after 20 min incubation. **(B)** Schematic representation of *nup153*, *nup358* and *ketel* transcripts drawn to scale. Indicated is the length of each annotated protein coding sequence (CDS) in base pairs (bp).

2.3 Characterization of Annulate Lamellae biosynthesis

I was particularly intrigued by the apparent local translation of exactly these two *nucleoporins* whose proteins have previously been identified as key regulators of NPC assembly (Nup153 via recruitment of membrane [170]) and architecture (Nup358 via dimerization of cytoplasmic NPC rings [23]) in other organisms. While most asymmetrically localized Nups (e.g. Nup214-complex, Nup62-complex, nuclear basket including Nup153) were previously shown to be absent from embryonic AL, Nup358 seemed to be enriched as compared to NE NPCs [84]. Furthermore, both Nup153 and Ketel protein products seem to mirror their respective mRNA localization (Suppl. Figure 2). Whereas Nup153 is restricted to nurse cells and absent from AL (Suppl. Figure 2A, red arrowheads), GFP-Ketel is present at both nurse cell and ooplasmic RFP-Nup107 foci (Suppl. Figure 2B-D). In order to see if Nup358 protein also mirrors its transcript localization, I decided to generate a fluorescent emeraldGFP-Nup358 fusion protein via CRISPR/Cas9-mediated endogenous genomic tagging to follow its role during oogenesis.

2.3.1 Nucleoporin granule composition and distribution

As expected for a stable component of the NPC, GFP-Nup358 clearly localized to the NE in all observed cell types (Figure 2-10A). In addition, GFP-Nup358 also marked a large number of cytoplasmic foci both in the oocyte (Figure 2-10A, red arrowheads) and in contrast to the previously observed GFP-Nup107 (Figure 2-2A, Figure 2-7) also within nurse cells (Figure 2-10A, B, yellow arrowheads). Upon closer inspection and combination with additional nucleoporin markers, the existence of several classes of granules became apparent that are differentially represented at different stages and compartments (Figure 2-10B-C). (i) Bright, spherical GFP-Nup358 positive granules, were relatively large (of 1-2 µm) and contained more GFP-Nup358 as compared to typical AL. In contrast to AL, the majority of their volume was devoid of RFP-Nup107 and FG-nucleoporins, but they sometimes contained these components in small sub-regions (Figure 2-10C, yellow arrowhead). These granules represented the main class within the nurse cell cytoplasm (Figure 2-10A, B, yellow arrowheads) and were rare in the ooplasm (Figure 2-10B-C). I will refer to them as 'Nup358 granules'. (ii) Comparably smaller granules that were negative for GFP-Nup358 (Figure 2-10C). They consisted of either RFP-Nup107 or FG-Nups, or a combination thereof (Figure 2-10B, cyan arrowheads; C) and were specific to oocytes. I thus classified them as 'oocyte specific granules'. (iii) Cytoplasmic foci positive

for all markers are putatively labeled as Annulate Lamellae (Figure 2-10B, red arrowheads; C). AL were exclusive to the ooplasm and displayed compact, but generally non-spherical shapes. This classification might need to be further refined with the availability of more nucleoporin markers in the future. Indeed, within granules, immunofluorescence staining via antibodies marking additional nucleoporins such as Nup214 and Gp210 showed the existence of even finer sub-structures within granules (Figure 2-10D-E).

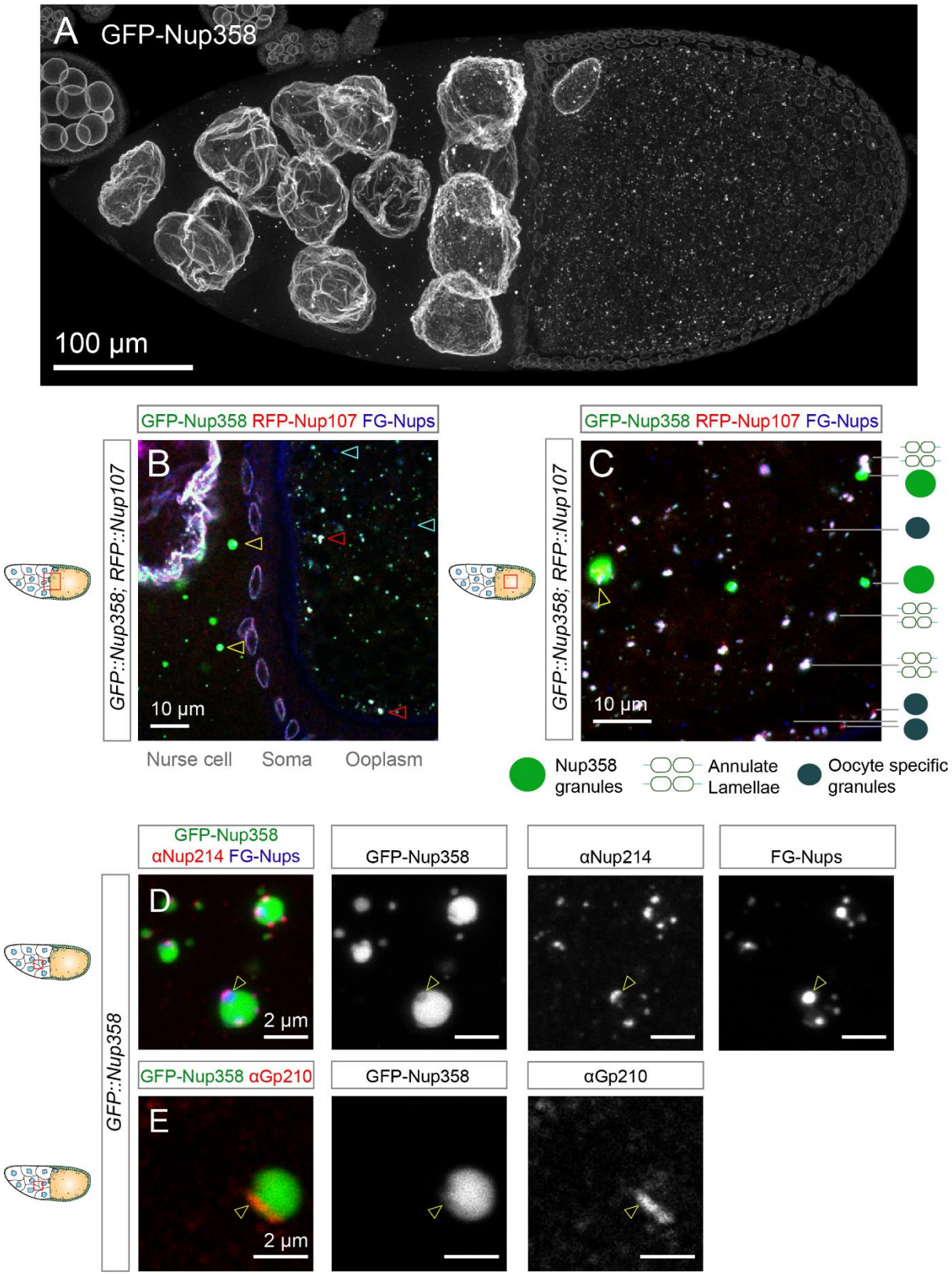

Figure 2-10: Nucleoporins form distinct granules throughout the egg chamber
(A) GFP-Nup358 localizes to follicle cell, nurse cell, and oocyte nuclear envelopes (NEs), and to cytoplasmic foci throughout nurse cell and oocyte compartments. Maximum intensity projection of a single stage 10b *GFP::Nup358* egg chamber covering 7 planes over 11 µm imaging depth. **(B-C)** Distribution of Nup358 granules, AL, and oocyte-specific granules between nurse cell and oocyte cytoplasm. Single confocal planes covering the nurse cell – oocyte border and oocyte of *GFP::Nup358; RFP::Nup107* transgenic egg chambers, and stained for FG-nucleoporins by

microinjection of wheat germ agglutinin (WGA-Alexa647). Based on marker distribution, granules were classified as large, spherical GFP-Nup358-dominant 'Nup358 granules', RFP-Nup107 and/or FG-Nup positive smaller 'oocyte-specific' granules, or triple-positive non-spherical 'AL'. Nup358 were predominantly located in nurse cells (B, yellow arrowhead) and rare in the ooplasm (C, yellow arrowhead), whereas oocyte-specific granules were restricted to the latter (B, cyan arrowheads, C). AL were also restricted to oocytes (B, red arrowheads, C). While generally devoid of RFP-Nup107/FG-Nups, Nup358 granules occasionally contained internal restricted accumulations of these components (C, yellow arrowhead). **(D-E)** The nucleoporins Nup214 and Gp210 localize to distinct regions within Nup358 granules. Maximum intensity projections over several confocal planes of a single stage 10 *GFP::Nup358* nurse cell region visualized by immunofluorescence with rabbit anti-Nup214 (D) or mouse anti-Gp210 AGP26.10 (E) antibodies. The cytoplasmic filament nucleoporin Nup214 occupies a distinct sub-region of the FG-Nup positive inclusion of a larger Nup358 granule (yellow arrowhead). This region shows reduced GFP-Nup358 intensity (D). The transmembrane nucleoporin Gp210 localizes to a continuous, linear surface-attached region that is reminiscent of internal membranes (E, arrowhead) and also exhibits locally reduced GFP-Nup358 intensity.

The perfectly spherical shape of these newly visible Nup358 granules with only partial inner accumulation of Nup107 (Figure 2-10C, arrowhead), led me to ask whether the earlier described discrepancy between circular mRNA accumulations around partially filled GFP-Nup107 foci (Figure 2-7A', C', D', E', arrowheads) in fact corresponded to hitherto uncharacterized Nup358 granules. In support of this, smFISH on *GFP::Nup358; RFP::Nup107* egg chambers showed clear *nup358* mRNA accumulation around a central GFP-Nup358 filled granule with partial interior accumulation of RFP-Nup107 in certain regions (Figure 2-11A), similar to what was observed previously for GFP-Nup107 (Figure 2-7A', C', D', E', arrowheads). As expected from the same observations with the remaining localized mRNAs, *nup153, ketel,* and *moleskin* exhibited the same enrichment around Nup358 granules (not shown). Higher magnification revealed that while *nup358* was largely covering the entire surface of GFP-Nup358 positive regions, it was consistently absent from exclusive FG-nucleoporin regions both in nurse cells (Figure 2-11B, arrowheads) and the oocyte (Figure 2-11C, arrowheads). An improved imaging protocol using stimulated emission depletion (STED) super-resolution microscopy further allowed to distinguish the earlier described accumulated RNA clusters around these foci into finer objects (Figure 2-11D), possibly representing individual RNA molecules. Adding these new observations to the previously stated RNC-mediated localization model, I conclude that individual *nup358* mRNAs are recruited to the surface of AL and Nup358 granules (Figure 2-7, Figure 2-11), but not oocyte specific granules (Figure 2-11B-C, arrowheads) via their nascent chain (Figure 2-8, Figure 2-9), where they cluster at a high density below the diffraction limit of confocal microscopy (Figure 2-11D).

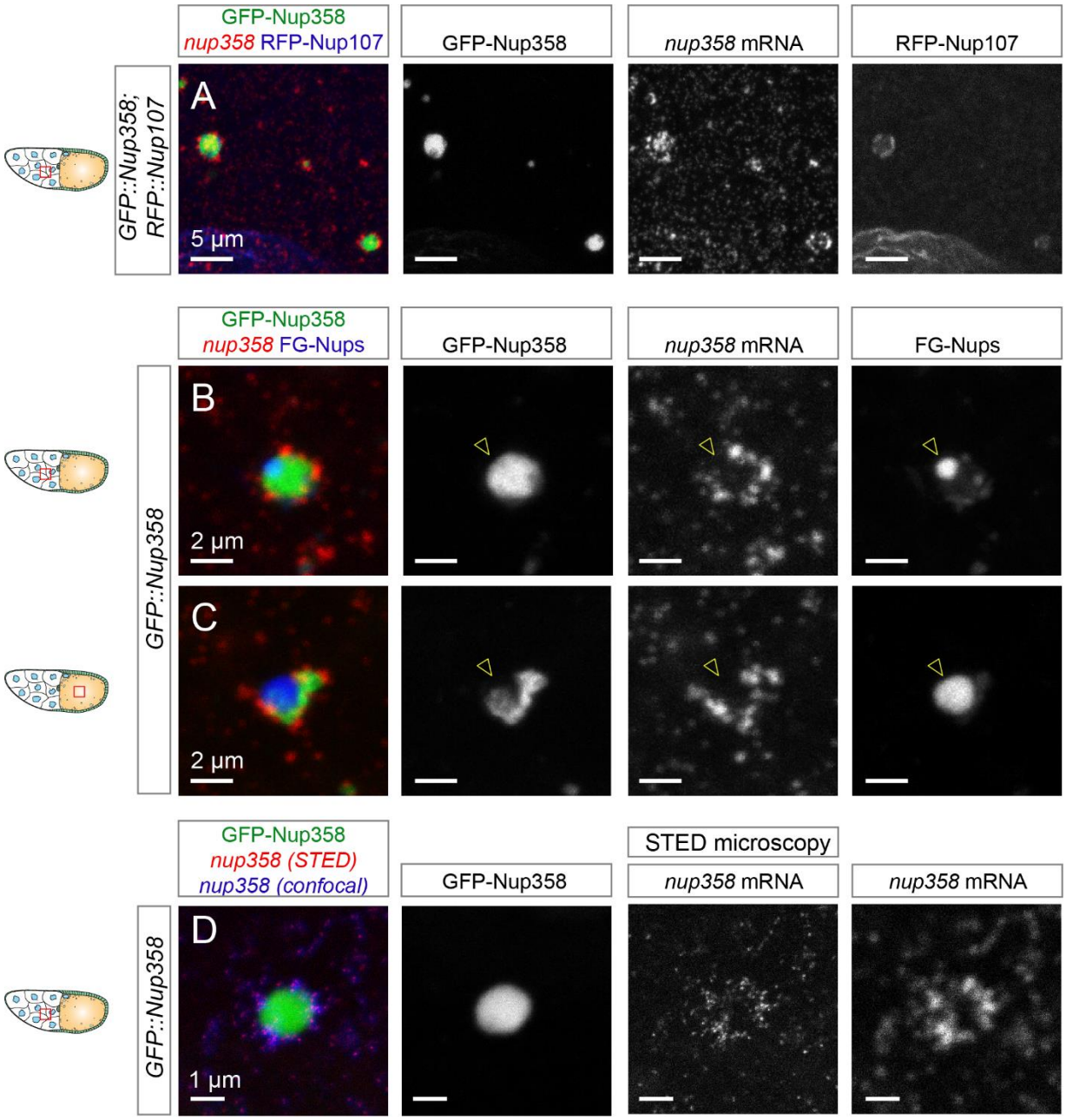

Figure 2-11: *nup358* mRNA forms clusters on the surface of Nup358 granules, but not FG-Nup foci
(A) *nup358* mRNA is attached to the outside of Nup358 granules. Maximum intensity projection over several confocal planes of a single stage 10 *GFP::Nup358; RFP::Nup107* nurse cell region hybridized with *nup358* smFISH probes. **(B-C)** *nup358* is enriched at GFP-Nup358 positive regions, but absent from FG-nucleoporins (arrowheads). As in (A), but acquired within the nurse cell (B) or oocyte (C) compartment of a *GFP::Nup358* egg chamber stained for FG-nucleoporins with wheat germ agglutinin (WGA-Alexa647). **(D)** *nup358* clusters can be divided into smaller smFISH foci. Stimulated emission depletion (STED) superresolution microscopy and conventional confocal microscopy of a single Nup358 granule within a *GFP::Nup358* nurse cell compartment, hybridized with *nup358* smFISH probes. Initial unresolved cluster of *nup358* smFISH signal can be resolved into smaller individual foci using STED microscopy.

Quantification of the spatial distribution of all three granule classes across oogenesis revealed that Nup358 granules disappeared at later stages, whereas oocyte-specific Nup granules remained present until egg maturation (Figure 2-12), but eventually

disappeared at some point prior to embryogenesis. AL progressively accumulated (Figure 2-2, Figure 2-12) and were also present in the early embryo, where they were the only Nup-positive structures in the cytosol (Figure 2-12A'", B). As nurse cells eventually expelled their cytosolic contents into the oocyte and underwent programmed cell death, later time points were not defined (N.D.). Conversion and comparison of this triple-labeling-based quantification to the earlier quantification of RFP-Nup107 accumulation (Figure 2-2), would lead to very similar results. Within nurse cells, the cytoplasmic occurrence of RFP-Nup107 positive foci (here AL + oocyte-specific granules) is minimal and largely restricted to the NE. In contrast, ooplasmic RFP-Nup107 positive structures (here AL + oocyte specific granules) accumulate both as a fraction of all identified granules (Figure 2-12) as well as in absolute amount (Figure 2-2).

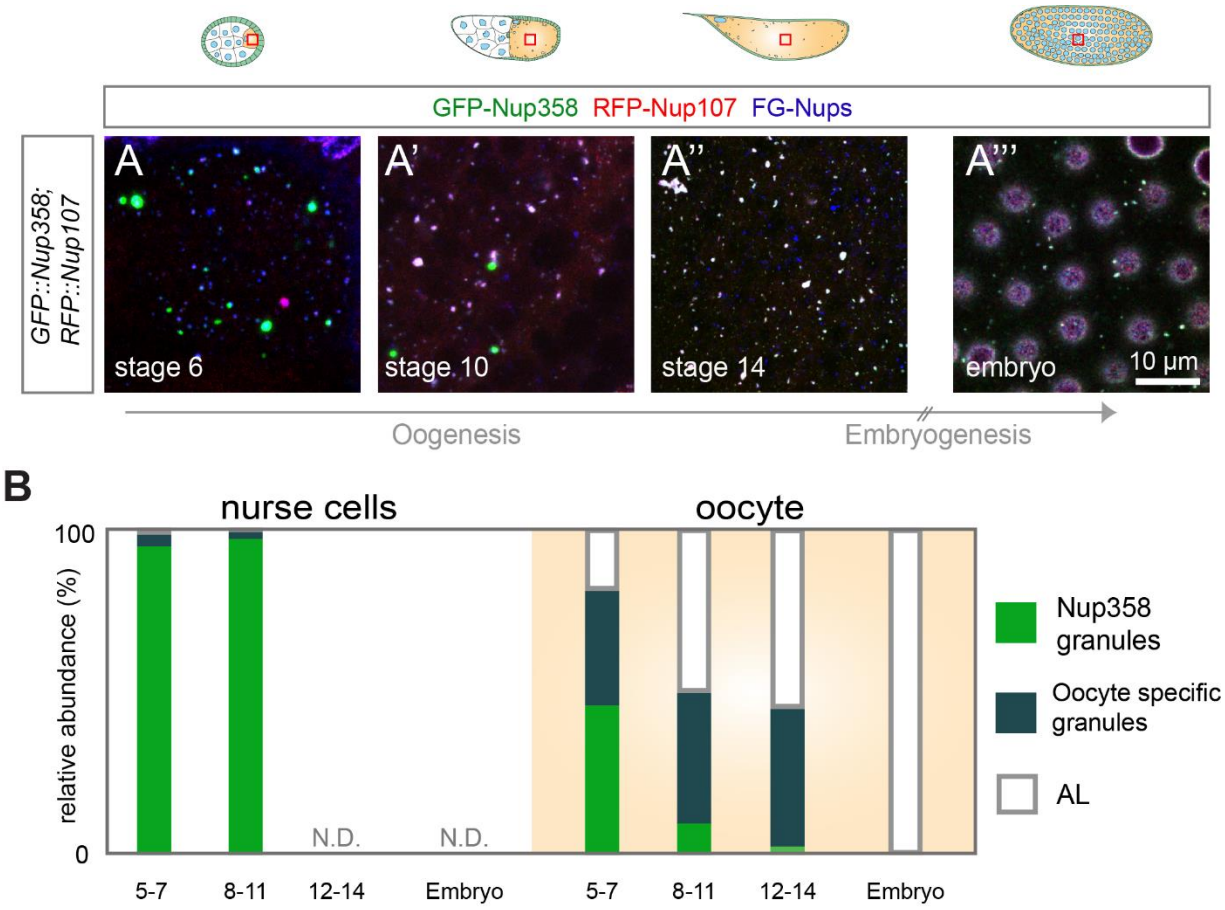

Figure 2-12: Spatial abundance of distinct nucleoporin structures throughout oogenesis (A-A'") Snapshots of increasing developmental stages shows changing proportions of Nup358 granules, oocyte-specific granules and AL over time. Single confocal images of the ooplasm of *GFP::Nup358; RFP-Nup107* transgenic egg chambers (A-A') at indicated stages, and the early embryo (A"'), stained for FG-nucleoporins by microinjection of wheat germ agglutinin (WGA-Alexa647). Whereas early stages exhibit a diverse mixture of nucleoporin granules (A), later stages exhibit a majority of AL and oocyte-specific granules (A'-A") and embryos only display AL (A"'). **(B)** Abundance of distinct nucleoporin granules and AL as a function of developmental time. Individual

granules were scored and counted within the different compartments and at different stages, and displayed according to their calculated proportions. In nurse cells, Nup358 granules are the dominant species throughout their lifetime. As nurse cells undergo nurse cell dumping and cell death around stage 11, later stages are not defined (N.D.). In oocytes, AL are in the minority at stages 5-7 with similar abundances of Nup358 granules and oocyte-specific granules, but Nup358 granules rapidly diminish and AL increase at later stages. As seen in (A'''), AL are the only remaining class in the embryo. Data was produced jointly with Dr. Bernhard Hampoelz.

2.3.2 Nucleoporin granule dynamics and microtubule-dependent transport

Based on the measured abundance trajectories of different nucleoporin granules (Figure 2-12), I hypothesized that both types represent NPC precursors that merge with each other to progress into AL within the oocyte. As Nup358 granules are predominantly located within nurse cells (Figure 2-10B, Figure 2-12B), these structures would thus have to be transported to the oocyte in order to interact with oocyte specific Nup granules. Culturing of *GFP::Nup358* egg chambers and continuous 3D imaging via selective plane illumination microscopy (SPIM) over a period of 6 hours indeed revealed tremendous movement of Nup358 granules within the egg chamber (Figure 2-13A). Importantly, several granules crossed the nurse cell – oocyte border and migrated into the oocyte (Figure 2-13A, arrowheads), where they however quickly disappeared, presumably due to the highly scattering imaging environment of the ooplasm. To further corroborate the directed migration of Nup358 granules through nurse cell – oocyte ring canals, together with Bernhard Hampoelz, we acquired confocal volumes of *GFP::Nup358; GAP43::mCherry* transgenic egg chambers with higher spatial and temporal resolution (Figure 2-13B). GAP43-mCherry here serves as a membrane marker, highlighting the cell membrane separating the nurse cells from the oocyte. As observed via SPIM imaging previously, we were able to capture several transition events within a relatively short imaging window, where Nup358 granules crossed the membrane opening corresponding to ring canals (Figure 2-13B) and entered the oocyte. Both during confocal and SPIM imaging, we did not observe any such migration events in the opposite direction.

As much of the inter-cellular transport within egg chambers is mediated by molecular motors traveling along the MT cytoskeleton, we attempted to visualize both MTs and GFP-Nup358 granules simultaneously. However, as the exceedingly high MT density within the intact oocyte renders visualization of individual MTs rather challenging, we decided to visualize co-labeling in *ex vivo* oocyte squash preparations instead (Figure 2-13C). Individual frames of the acquired time series shows fast, directed runs along an intact MT network, characteristic of motor-dependent transport along MTs (Figure

2-13C). Within the intact ooplasm, Nup358 granules and oocyte specific granules frequently made direct contact with each other or with AL (Figure 2-13D-E). During this, they occasionally fused (Figure 2-13D) but more often stayed adjacent for many minutes, possibly allowing transfer of material between them (Figure 2-13E).

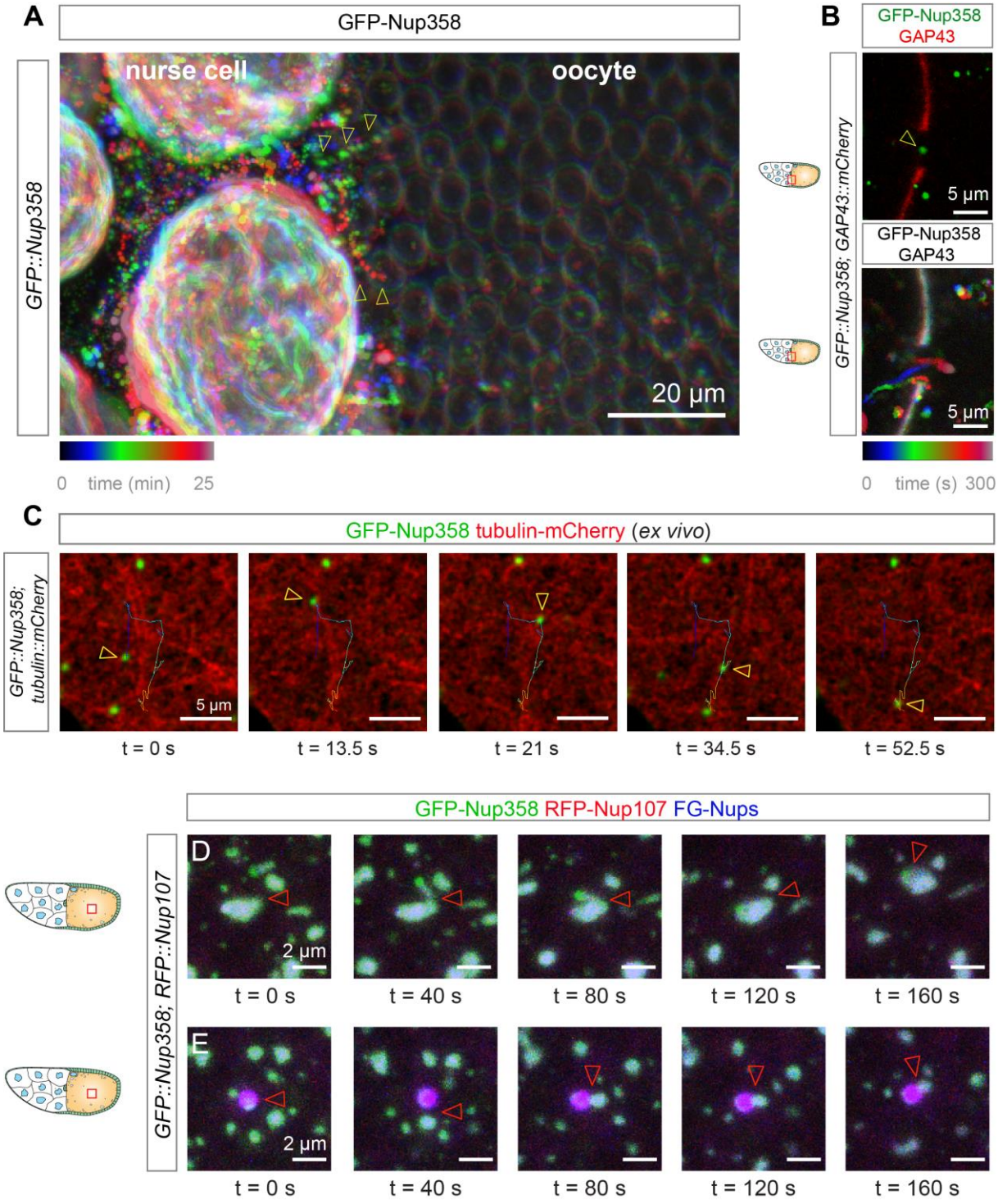

Figure 2-13: Nucleoporin granules are subject to microtubule-dependent movements and interactions

(A-B) Nup358 granules move from nurse cells to the oocyte. (A) Selective plane illumination microscopy (SPIM) imaging of an entire live stage 10 *GFP::Nup358* egg chamber over 6 hours showed abundant movement of Nup358 granules within the cytoplasm, as well as occasional

transition of individual granules from a nurse cell into the ooplasm (A, arrowheads). Within the ooplasm, they rapidly disappeared, presumably due to poor imaging conditions in the oocyte. Individual frames are overlaid as temporal projection and color-coded based on imaging time. SPIM data was acquired jointly with Dimitri Kromm. (B) Confocal microscopy across a single ring canal connecting a nurse cell and oocyte in a *GFP::Nup358; GAP43::mCherry* stage 10 egg chamber also revealed several such observed crossing events. GAP43-mCherry serves as a membrane marker highlighting the separating membrane and the ring canal as opening within. Top image depicts a single frame during a crossing event, whereas the bottom image represents a temporal color projection as in (A). **(C)** Nup358 granules display fast, directed runs along an intact microtubule (MT) network. Confocal time-lapse microscopy of an e*x vivo GFP::Nup358; tubulin::mCherry* oocyte squash preparation. Visible in red is a dense MT network with occasional individual filaments. Panels represent single frames depicting turning points of linear GFP-Nup358 movements at indicated time points. The color-coded trace highlights the overall path of the granule. **(D-E)** Nucleoporin granules interact with each other and with AL within the oocyte, resulting either in fusion or extended attachment. Individual frames of a time-lapse confocal volume acquired in *GFP::Nup358; RFP::Nup107* egg chambers stained for FG-Nucleoporins by microinjection of wheat germ agglutinin (WGA-Alexa647), and flattened via maximum projection. Large volumes were acquired and individual fusion or extended attachment events were extracted. Panel (D) depicts the approach, fusion on one end, followed by flattening on the other end of a granule with a larger AL. The newly fused AL stayed intact throughout the remaining data acquisition. Panel (E) shows the initial binding and extended interaction of a small AL with a larger oocyte-specific granule, potentially to allow slow transfer of material between them. Data for panels B-E were produced jointly with Dr. Bernhard Hampoelz.

In order to test whether MT-dependent transport and granule interactions are important for AL biosynthesis, we again fed female flies overnight with colchicine-supplemented food. Live cell imaging and quantification of nucleoporin marker distribution on the following day revealed both a strong reduction of granule dynamics (Figure 2-14A-A'), as well as a clear decrease in overlap of nucleoporin markers (Figure 2-14B-B'). Although granule integrity was unperturbed by colchicine treatment, they stayed separated more often and did not combine. This resulted in an overall reduction of AL density within the oocyte with a corresponding increase of individual granules (Figure 2-14C). This suggests that both MT-dependent transport and facilitated interactions are necessary for efficient precursor granule mixing and consequently ALPC formation.

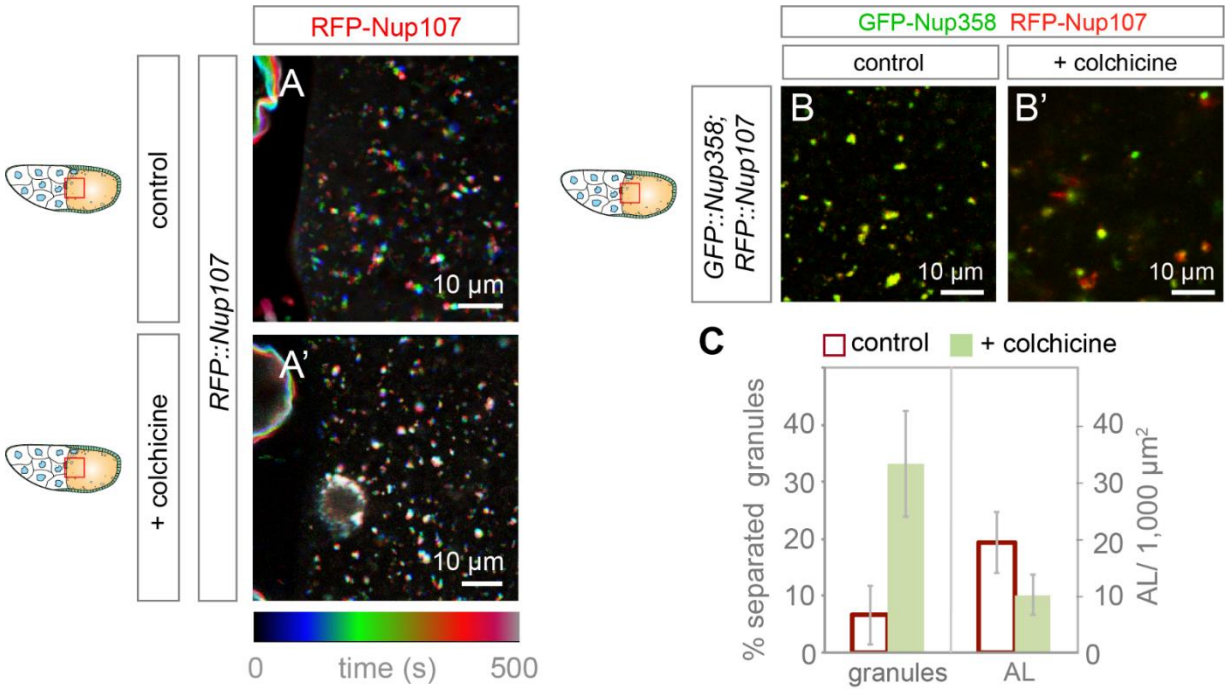

Figure 2-14: Microtubules-dependent movements mediate AL assembly
(A-A') Microtubule depolymerization via colchicine abolishes nucleoporin granule movements. Temporal projections of time-lapse confocal imaging of a single plane in *RFP::Nup107* egg chambers across the nurse cell – oocyte border. Movies were acquired from dissected egg chambers of flies that were either fed with regular yeast paste (A) or with yeast paste supplemented with 100 µg/ml colchicine in 1% sucrose for 16 h (A'). Movements are largely abolished as indicated by the increasingly white (overlap) color in (A). **(B-C)** MT-depolymerization increases Nup granule proportion and reduces the amount of AL. (B-B') Single confocal images of ooplasmic regions acquired by live imaging of a *GFP::Nup358; RFP-Nup107* stage 10 egg chamber dissected from flies treated as described in (A-A'). While the overlap of RFP-Nup107 and GFP-Nup358 is typical for stage 10 ooplasm (refer to Figure 2-12) for control flies (B), they display markedly increased separation upon colchicine treatment (B'). Quantification of granule classes based on this marker overlap shows an increase in the proportion of separated granules (C) with a concomitant decrease of AL abundance (C) compared to flies kept on regular food. Data was produced by Dr. Bernhard Hampoelz.

2.3.3 Nucleoporin granules display features of biomolecular condensates

High resolution fluorescence imaging of Nup358 granules in fixed and stained *GFP::Nup358* egg chambers frequently revealed an intricate compartmentalization of different nucleoporins, reminiscent of multi-component phase separation of several liquid-like constituents (Figure 2-15). According to polymer physics, multi-liquid coexistence and demixing can arise when the interaction energies and therefore surface tension between the different components, as well as with the surrounding solvent (water), follow specific relationships [56]. As proteins can be described as biopolymers of individual amino acids, this framework has proven increasingly useful to describe the organization of membrane-less compartments in biology. Particularly early during oogenesis, Nup358 granules and oocyte specific granules display a characteristic arrangement called a Neumann's triangle

(Figure 2-15A), where the interface tension or energetic costs between the droplets is identical or similar to the surrounding solvent [326]. At later stages this seems to change, and droplets more frequently display FG-Nup regions enveloped within GFP-Nup358 droplets (Figure 2-15B-C), indicating that at this stage the interface between oocyte specific granules and water is more costly than that of Nup358 and water or Nup358 and FG-Nups [56]. The occasional observation of an internal region of reduced staining intensity within certain FG-Nup droplets (Figure 2-15C, arrowhead) that are themselves enveloped within a larger Nup358 droplet, raises the possibility of even further sub-compartmentalization, potentially inhabited by other nucleoporins as previously seen for Nup214 (Figure 2-10D, arrowhead). As a physical attribute of a liquid-like state, each droplet assumes (or attempts to assume) a spherical shape to minimize its surface area. This is displayed particularly well in the shape of (Figure 2-15B), which harbors a perfectly round main droplet which is separated from a smaller GFP-Nup358 droplet with local accumulation of FG-nucleoporins at the interface (Figure 2-15B, arrowhead). This arrangement looked strikingly similar to previously characterized the previously observed spherical exclusion zone structures in RFP-Nup107 CLEM (Figure 2-4C).

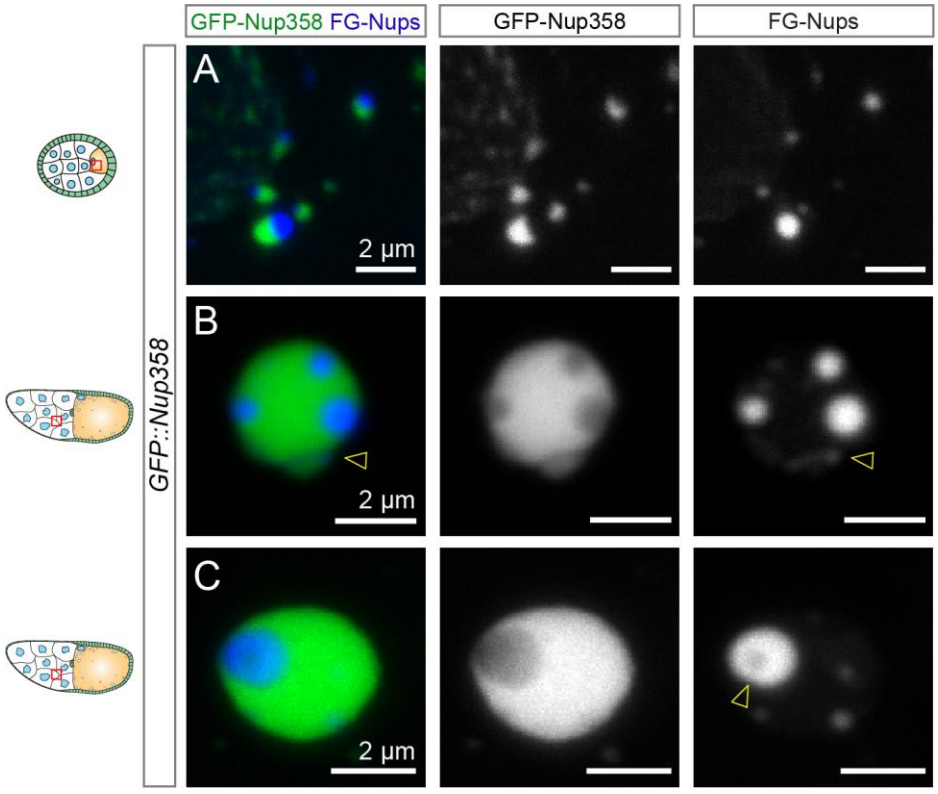

Figure 2-15: Nup358 granules display a layered organization and interfaces characteristic of multi-component phase separation
Maximum projection images of confocal volumes acquired from fixed *GFP::Nup358* egg chambers stained for FG-nucleoporins with wheat germ agglutinin (WGA-Alexa647). In early stage 5 oocytes (A) Nup358 granules and oocyte-specific granules form large contact interfaces and stay associated but do not immediately mix. At later stages (B-C), within nurse cells FG-Nucleoporins have

transitioned to occupy distinct regions within or on the surface of Nup358 granules. The example in panel (C) appears to have undergone a recent fusion event, as the FG droplet is still rather peripheral and the Nup358 part has not quite reverted to an optimal round shape yet. At places of internal FG-Nup occupation, GFP-Nup358 content is reduced (B-C, arrowheads) and occasionally FG-Nups also display internal intensity minima, indicative of further compartmentalization (C, arrowhead). FG-Nups further accumulate at the dividing interfaces between two Nup358 droplets (Figure 2-15C).

To test whether these were indeed the same structures that I had previously observed, I performed dual color CLEM on *GFP::Nup358; RFP::Nup107* transgenic egg chambers. Particularly in stage 10 nurse cells, I could indeed identify multiple large assemblies (Figure 2-16A-B') that looked both strikingly similar to the previously identified structures (Figure 2-4C), as well as the layered droplet structures visualized by fluorescence microscopy in fixed egg chambers (Figure 2-15A-B'). Also here, RFP-Nup107 decorated internal membrane structures (Figure 2-16A-B', red arrowheads) that were continuous with rER, whereas GFP-Nup358 filled the large interior ribosome exclusion zone. One such structure further displayed round (in 2D sections) internal and surface-associated regions of locally reduced GFP-Nup358 fluorescence signal that corresponded to a distinct EM staining density (Figure 2-16B-B', yellow arrowheads). Interpolating from whole mount fluorescence staining data (Figure 2-15), these regions could likely be occupied by FG-Nups or other nucleoporins that I was unable to stain against on resin-embedded EM sections. As expected based on the previous spatiotemporal quantification (Figure 2-12), within the oocyte I now found a variety of structures including many mature AL with multiple parallel membrane stacks (Figure 2-16E-E'), and smaller structures with a single (Figure 2-16D-D') or no central sheets (Figure 2-16C-C'). These could represent assembly intermediates that are in the process of conversion from a Nup358 granule to AL. Further supporting the notion that Nup358 granules in fact represent sites of AL biosynthesis, I was able to identify hexagonally arranged circular structures that looked identical to NPCs within the RFP-Nup107 positive membrane stretches of Nup358 granules (Figure 2-16F-G'"). While AL assembly appears to be largely inhibited within nurse cells as judged by RFP-Nup107 accumulation (Figure 2-2B), some residual assembly nevertheless appears to take place, which might then be completed upon interacting with other Nup granules after transport into the oocyte (Figure 2-13). As both the Y-complex (including Nup107) and several FG nucleoporins are crucial for the structural integrity and assembly of the NPC, this supply of structural components in the oocyte could thus be a rate limiting step as they are largely absent in nurse cells (Figure 2-2, Figure 2-10B).

In all observed cases of AL and Nup granules, the membrane-overlapping RFP-Nup107 signal was covered and extended by a GFP-Nup358 positive zone that consistently excluded cellular constituents such as ribosomes (Figure 2-16, insets). While these compartments often do contain internal membranes, they are markedly not enclosed within a membrane (Figure 2-1, Figure 2-3B-C", Figure 2-4, Figure 2-16). Their internal composition that is markedly distinct from the surrounding cytoplasm thus has to originate by a different mechanism. A hallmark of biomolecular phase separation is the concentration of molecules with favored surface chemistries and simultaneous exclusion of non-favored molecules [327,328]. Consequently, previously characterized membraneless compartments based on liquid-liquid phase separation have also been shown to exclude ribosomes [327]. As such a selective permeability barrier function lies at the heart of nucleoporin function also within the central NPC channel, and as nucleoporins have previously been observed to undergo liquid-liquid phase separation [65] *in vitro*, it is thus a likely explanation for the GFP-Nup358 exclusion zone within Nup granules and AL *in vivo*.

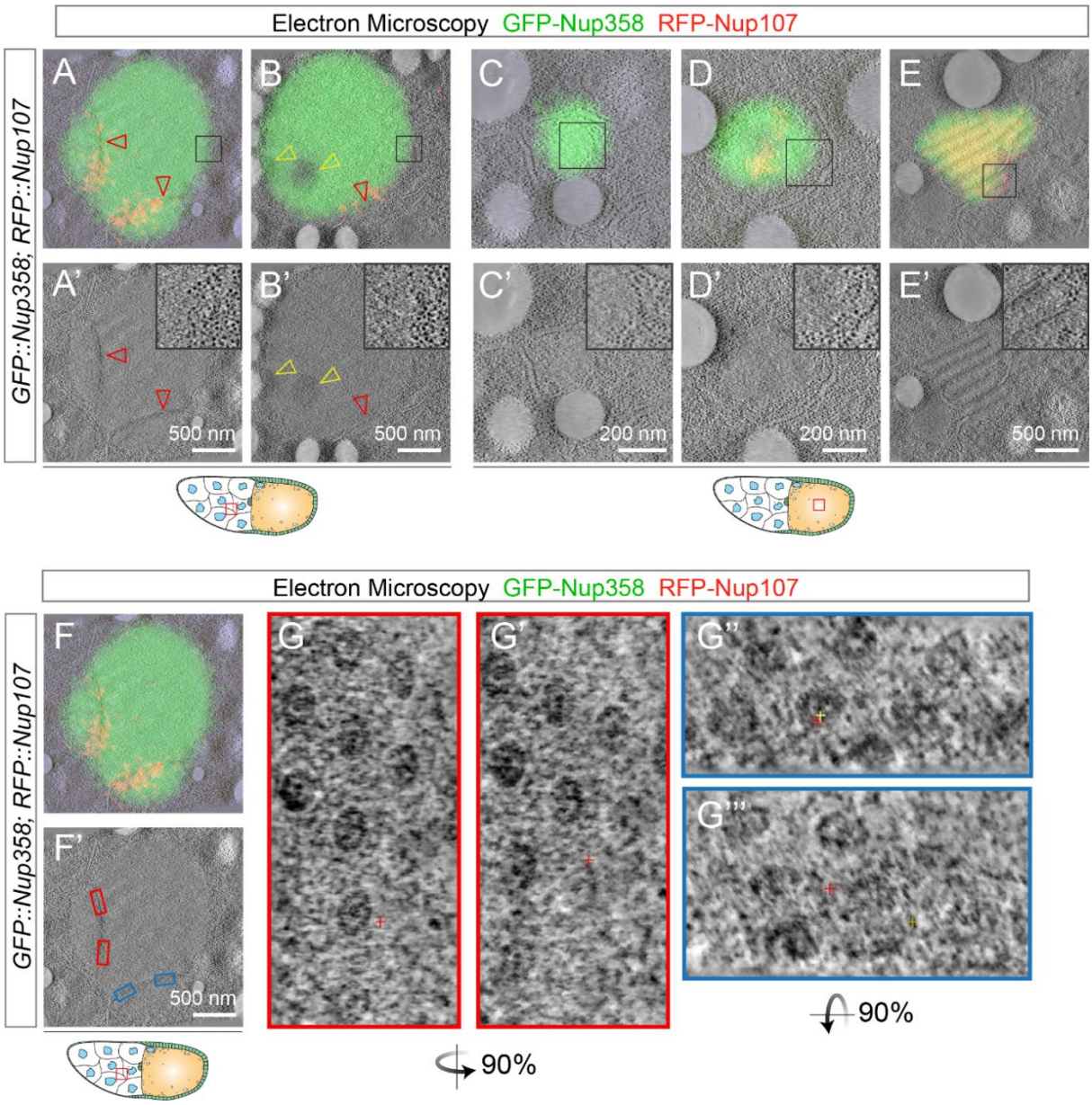

Figure 2-16: Nup358 granules display ultrastructural characteristics of AL precursors
Dual color correlative light and electron microscopy (CLEM) of ~200 nm sections cut from high pressure frozen and resin-embedded *GFP::Nup358; RFP::Nup107* stage 10 egg chambers. **(A-B')** Nup358 granules represent earlier identified unknown structures with large exclusion zones. Overlays confirmed the localization of RFP-Nup107 at internal membrane stretches (red arrowheads) and further revealed the location of GFP-Nup358 to previously identified extended ribosome exclusion zones (inserts; refer to Figure 2-4), thus identifying these structures as Nup358 granules. One of the granules (B-B') further displayed internal areas of locally reduced GFP-Nup358 fluorescence, that corresponded to distinct staining density in EM (B-B', yellow arrowheads) and furthermore to the layered organization observed in fluorescence microscopy (refer to Figure 2-15B-C). Internal membrane stretches were continuous with the endoplasmic reticulum. **(C-E')** Observation of distinct granules with variable membrane content within the ooplasm. The fluorescence-guided acquisition of GFP-Nup358 and/or RFP-Nup107 positive structures revealed a variety of structures within the ooplasm that could represent distinct intermediates. They range from pure exclusion zones without, but often adjacent to, membranes (C-C'), to large exclusion zones with a single or few internal membranes (D-D'), up to fully formed AL (E-E'). RFP-Nup107 invariably decorated membrane and GFP-Nup358 was overlapping and extending into the surrounding exclusion zone (E). **(F-G''')** Nup358 granule internal membranes already contain pore complexes. As the CLEM composite images represent correlation to single

slices of acquired volume, rotation of said volume shows the hexagonally arranged appearance of pore complexes within internal RFP-Nup107 and GFP-Nup358 positive membranes.

Liquid-liquid phase separation of biopolymers is generally established via weak, multivalent interactions – often in the form of repeated folded domains or intrinsically disordered regions [56]. Fittingly, nucleoporins including the eponymous FG-nucleoporins and Nup358, contain large intrinsically disordered regions of hydrophobic FG repeats. In addition however, Nup358 also contains a number of TPR, RanBD and zinc-finger domains (Figure 1-2) that might mediate biomolecular condensation. Perhaps unsurprisingly as they are amongst the most hydrophobic soluble proteins within the cell [48], their higher order assembly was previously shown to be sensitive to hexanediols [68,69], agents known to interfere with hydrophobic interactions. In order to probe whether *in vivo* phase separation of nucleoporins also depends on hydrophobic interactions, I incubated dissected *GFP::Nup358; RFP::Nup107* egg chambers in culturing medium containing 5% 1,6-hexanediol for 15 min prior to fixation. Surprisingly, this incubation completely abolished not only Nup granules, but also AL and NE localization of all nucleoporin markers (Figure 2-17A-B). The same effect could also be observed for GFP-Nup358 during live cell imaging after addition of 5% 1,6-hexanediol to the imaging medium. Within a few minutes, all Nup358 containing structures entirely dissolved into the surrounding cytoplasm (Figure 2-17C). I thus conclude that both *in vivo* phase separation, as well as NPC integrity within egg chambers is reliant on hydrophobic interactions. Whether these are mediated by FG repeats or repeated hydrophobicity-based interaction domains however is not clear at this point and will require further investigation such as genetic deletion studies.

Another widely recognized hallmark of assemblies with liquid-like properties is the highly dynamic nature of its interactions, arising from the mentioned predominantly weak, multivalent interfaces. Fluorescence recovery after photobleaching (FRAP) is a common tool used to probe these dynamics as a high turnover leads to fast replenishment of bleached macromolecules with new ones and thus a fast recovery rate. As Nup358 granules were highly mobile within the egg chamber (Figure 2-13A, Figure 2-14A), it was challenging to observe individual granules within the imaging volume throughout their recovery. Egg chamber squash preparations onto the imaging coverslip reduced this issue by constraining the expelled cytoplasm within a thin layer, thus preventing diffusion in z direction. Both *ex vivo* and *in vivo*, I was ultimately able to observe Nup358 granules throughout their internal recovery, which occurred on the order of ~10 – 20 seconds (Figure 2-17D-D"), thus showing rapid intra-droplet dynamics. It furthermore shows that

the dynamics are not influenced by breaking granules out of their cellular context during *ex vivo* oocyte squashes (Figure 2-17D-D').

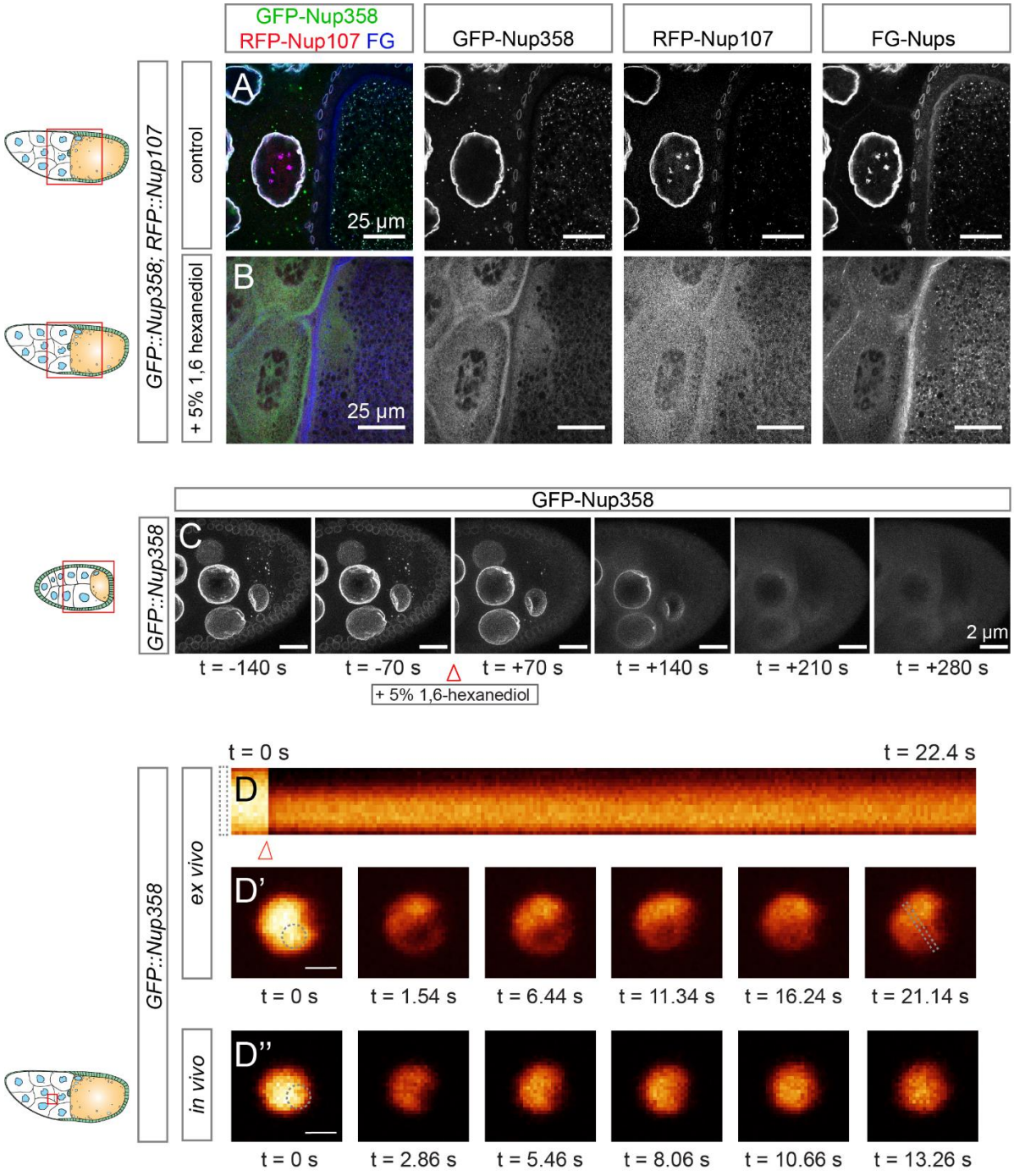

Figure 2-17: Nucleoporin condensation is dynamic and dependent on hydrophobic interactions

(A-C) Nucleoporins can be dissolved by treatment with 1,6-hexanediol. (B) Incubation of *GFP::Nup358; RFP::Nup107* egg chambers in imaging medium supplemented with 5% 1,6-hexanediol for 15 minutes caused the widespread dissociation of all observed nucleoporins, as assayed by fixation, staining for FG-nucleoporins with wheat germ agglutinin (WGA-Alexa647) and confocal imaging. Images represent single confocal slices of stage 10 egg chambers. Nucleoporin localization at the NE, AL and Nup granules were equally effected. (C) Live cell time-lapse confocal imaging of stage 8 *GFP::Nup358* egg chambers showed the rapid dissolution of all GFP-Nup358 positive structures upon exchange of imaging medium with imaging medium

supplemented with 5% 1,6-hexanediol within a few minutes. **(D-D")** Nup358 granules display rapid internal dynamics. Fluorescence confocal imaging of Nup358 granules in intact stage 10 *GFP::Nup358* egg chambers (D") or *ex vivo* oocyte squash preparations of stage 10 *GFP::Nup358* oocytes. Photobleaching of a small area within the droplet and continuous imaging revealed the rapid internal recovery of fluorescence (D-D"). (D) Kymograph representation of the highlighted rectangular area in (D') throughout bleaching and recovery.

2.3.4 Regulation of nucleoporin condensation and AL assembly

In this section I so far established the existence of several distinct nucleoporin granules that display characteristics of biomolecular condensates, that these undergo directed movements and interact with each other based on MT-dependent transport, and that this ultimately leads to the assembly of Annuate Lamallae. Yet apart from enforced interactions, it is still unclear how such an elaborate series of events is regulated on a molecular level. As introduced previously, the Ran gradient across the NE, established by asymmetric localization of Rcc1 and RanGAP, is simultaneously the basis for nucleocytoplasmic transport, and both NPC assembly pathways. I thus aimed to establish the involvement of these Ran cycle components in AL assembly.

As reported previously, immunofluorescence showed the distinct localization of Rcc1 to large parts of the nurse cell nucleoplasm (Figure 2-18A", white arrowhead, [329]), presumably bound to chromatin, and of RanGAP to the nurse cell NE (Figure 2-18A', white arrowhead, [103]). In oocytes, Rcc1 is massively enriched within the nucleus (Figure 2-18A", cyan arrowhead) as compared to nurse cell nuclei, whereas RanGAP displays a slightly depleted NE localization (Figure 2-18A', cyan arrowhead). In addition, RanGAP further decorated globular cytoplasmic structures (Figure 2-18B', yellow/red arrowheads) that were described but remained unidentified previously [103]. I could show that these represent Nup358 granules and AL respectively (Figure 2-18D). Furthermore, its localization to both AL and cytoplasmic foci is dependent on Nup358, as shRNA-mediated gene silencing of *nup358* (Figure 2-18C) led to relocalization of RanGAP towards the cytoplasm (Figure 2-18E). As the knockdown was incomplete (Figure 2-18C, Suppl. Figure 3B-C) and only induced around stage 4 of oogenesis (Suppl. Figure 3A), some remaining GFP-Nup358 was still present within the egg chamber (Figure 2-18E-E", arrowheads) and wherever it was present, RanGAP was equally still associated (Figure 2-18E", arrowheads). Rcc1 on the other hand appeared homogenously enriched within the ooplasm (Figure 2-18B", red arrowhead) as compared to the nurse cell cytoplasm. As I could not visualize the nucleotide status of Ran directly, interpolation from RanGAP/Rcc1 localization would indicate a local high concentration of RanGDP around both Nup358

granules and AL, with surrounding high RanGTP concentration specifically in the ooplasm but not the nurse cell cytoplasm.

Upon direct comparison of GFP-Nup358 and RanGAP immunofluorescence intensities across the different structures, it became apparent that both GFP-Nup358 and consequently RanGAP was much more abundant in Nup358 granules as compared to NE or AL (Figure 2-18F-G'). As Nup358 are presumably converted into AL upon entering the oocyte, this process would result in a reduction of Nup358/RanGAP content during the transition to AL. In contrast, as seen previously, RFP-Nup107 fluorescence increased from Nup358 granules to AL (Figure 2-18H-H'), which is in line with its so-far exclusive identification on membranes (Figure 2-1, Figure 2-4, Figure 2-16) and the increased membrane content of AL compared to Nup granules (Figure 2-16).

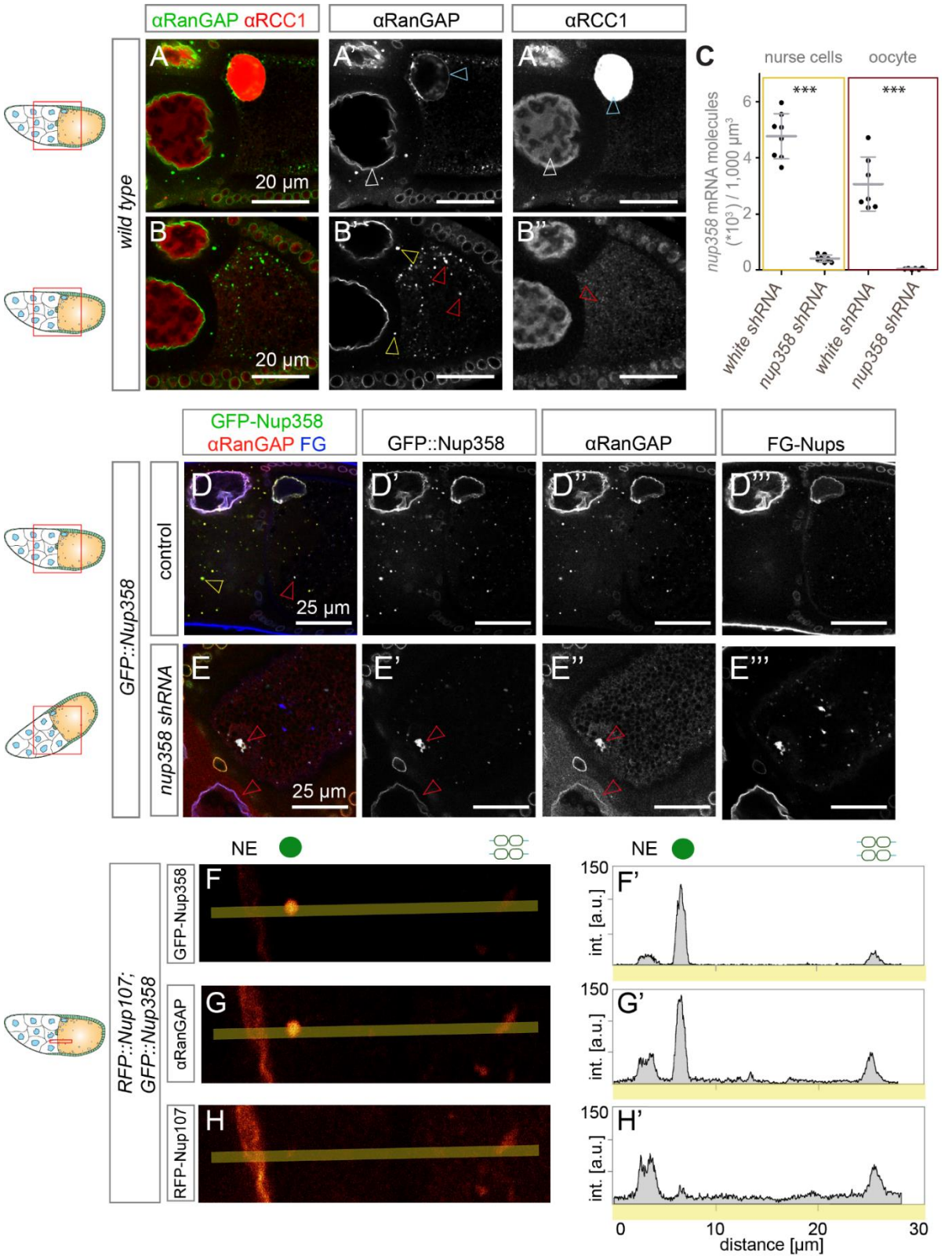

Figure 2-18: Localization of RanGAP and Rcc1 throughout the egg chamber
(A-B) RanGAP localizes to the NE, AL and nucleoporin granules, Rcc1 is located in the nucleoplasm and ooplasm. Single confocal images of fixed stage 10 *wild type* egg chambers subjected to immunofluorescence via rabbit anti-RanGAP and mouse anti-BJ1 (Rcc1) antibodies. Rcc1 is predominantly located within the oocyte nucleus (A", cyan arrowhead) and to a lesser extent in nurse cell nuclei (A", white arrowhead) and is furthermore markedly enriched within the ooplasm (B", red arrowhead). RanGAP is localized to the NE at both nurse cell (A', white arrowhead) and oocyte (A', cyan arrowhead) nuclei, and furthermore to many cytosolic structures

in both nurse cell (B', yellow arrowheads) and oocyte cytoplasm (B', red arrowheads). **(C-E)** RanGAP localization at all structures is Nup358-dependent. (C) Knockdown of *nup358* via a *nup358* targeting shRNA, expressed in the germline via UAS/matGal4 was assessed via smFISH-based transcript counting in both nurse cell and oocyte compartments, and compared to a control shRNA targeting the unrelated *white* transcript. The calculated knockdown efficiency was 91.5% in nurse cells and 98.8% in oocyctes (*** $p<0.0001$, unpaired t-test; n [*nup358*] = 6 recorded volumes from 4 egg chambers for oocytes and 7 volumes from 4 egg chambers for nurse cells, n [*white*] = 6 volumes from 4 egg chambers for both compartments). (D-E) Single confocal images of fixed stage 10 *GFP::Nup358* egg chambers either expressing *nup358* shRNA or control, subjected to immunofluorescence via rabbit anti-RanGAP and mouse anti-BJ1 (Rcc1) antibodies. Whereas RanGAP co-localized with GFP-Nup358 at the NE (D), Nup358 granules (D, yellow arrowhead) and AL (D, red arrowhead) in *GFP::Nup358* egg chambers, partial shRNA-mediated *nup358* knockdown resulted in a partial dissociation into the cytoplasm (E"), with resident signal proportional to the residual GFP-Nup358 signal. **(F-H')** Nup358 and RanGAP are more abundant in Nup358 granules than at AL. Single confocal images of fixed stage 10 *GFP::Nup358* egg chambers imaged across the nurse cell – oocyte border. Yellow rectangles (F, G, H) mark quantified area of the corresponding intensity line profiles (F', G', H'). While RFP-Nup107 displayed higher fluorescence intensities at the NE and AL as compared to Nup358 granules, this was reversed for GFP-Nup358 and anti-RanGAP staining.

As RanGAP and Rcc1 are merely indicators of the Ran nucleotide status, I wanted to assess the effects of Ran on AL assembly more directly. For this, I crossed *GFP::Nup358* transgenic flies with flies expressing different Ran mutants via the GAL4/UAS system [330] under the germline-specific maternal Gal4 driver [331]. Whereas expression of wild-type Ran had no discernable effect on GFP-Nup358 distribution (Figure 2-19A, D), RanT24N, which is locked in a GDP-bound state, almost entirely abolished the presence of any cytosolic GFP-Nup358 foci (Figure 2-19B, D). In contrast, expression of the constitutively GTP-bound RanQ69L mutant protein led to a drastic increase in cytoplasmic GFP-Nup358 foci across the egg chamber (Figure 2-19C, D). Furthermore, while I have observed occasional fusion events of Nup358 granules with both nurse cell and oocyte NEs in *GFP::Nup358* flies before (not shown), in *GFP::Nup358; mat-Gal4; UAS-HA::RanQ69L* egg chambers, many of the cytoplasmic Nup358 foci were continuous with the NE, as if they were stuck in such fusion events (Figure 2-19C, arrowheads). Surprisingly, Ran thus not only seems to regulate AL assembly, but markedly also nucleoporin condensation. Such an effect of regulatory proteins – even dependent on bound nucleotide status – on biomolecular condensation has indeed been observed in other contexts [332,333], but to the best of my knowledge not for nucleoporins. With exception of wild-type Ran, expression of either mutant proteins resulted in embryonic lethality [103]. As Ran is a regulator of a vast number of essential processes however, it is unclear whether this is due to its effects on Nup condensation/AL assembly or other essential processes.

Immunofluorescence of HA-tagged Ran mutant proteins displayed as single confocal slices shows that HA-RanT24N closely mirrors the localization of Rcc1 to chromatin in the

nuclear interior (Figure 2-19F), whereas HA-RanQ69L mirrors the distribution of RanGAP at NE (Figure 2-19G), cytoplasmic Nup granules and AL (Figure 2-19G, red/yellow arrowheads). Wild-type Ran shows an intermediate behavior between the two mutant proteins and is rather uniformly distributed across nuclei and cytosol (Figure 2-19E), but notably not significantly enriched at AL/granules (Figure 2-19E, red/yellow arrowheads). Occasional mosaic expression of HA-RanT24N in most but not all nurse cells shows that individual cells with low expression of HA-RanT24N (Figure 2-19H") in fact still exhibit Nup358 granules (Figure 2-19H', arrowheads) contrary to their surrounding sister cells. This corroborates the direct effect of RanT24N expression on nucleoporin condensation in egg chambers. Interestingly, these cells were also larger and their nuclei were more distorted (i.e. similar to wild-type situation), a to my knowledge so-far undescribed function of the Ran gradient in flies.

Whereas ooplasmic AL in *GFP::Nup358; mat-Gal4; UAS-HA::Ran* egg chambers had normal dimensions and shapes (Figure 2-19E, red arrows), the corresponding structures in *GFP::Nup358; mat-Gal4; UAS-HA::RanQ69L* oocytes appeared much larger and overall less spherical (Figure 2-19G, red arrowheads). They were further typically found at the anterior border, where the oocyte is connected to its nurse cells via ring canals and where Nup358 granules were shown to cross (Figure 2-13A-B). Combined with the abundant occurrence of Nup358 granules stuck at the NE (Figure 2-19C, arrowheads), it is tempting to speculate that RanGTP typically promotes AL assembly by modulating nucleoporins to be more prone to interact. Excessive RanGTP as in ectopic *HA-RanQ69L* expression might thus exacerbate this effect and render them too 'sticky', which would lead to widespread aggregation.

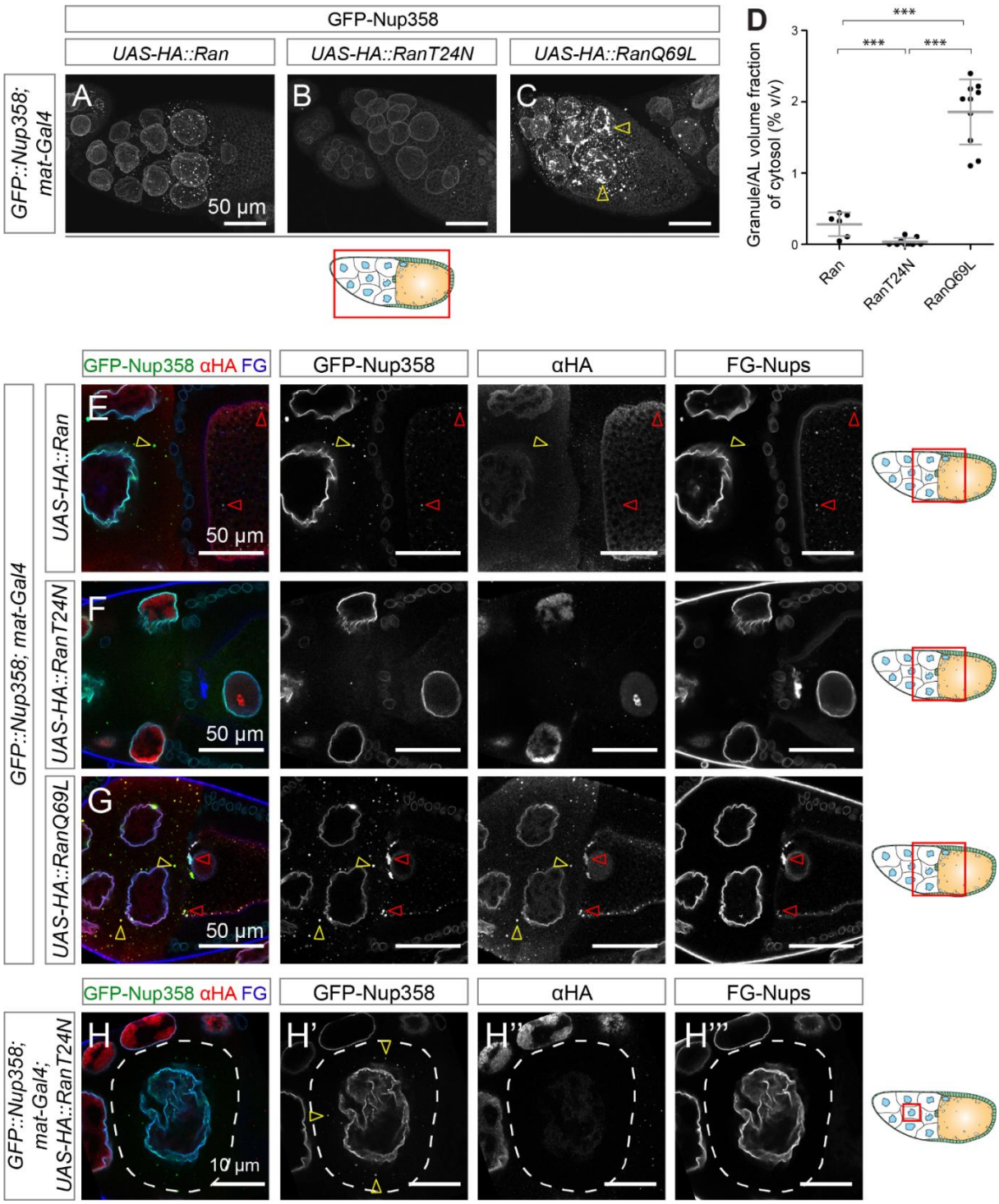

Figure 2-19: The nucleotide status of Ran controls nucleoporin condensation and AL assembly

(A-D) Expression of Ran mutants effects the amount of GFP-Nup358 structures throughout the egg chamber. Maximum projection images of confocal volumes covering entire stage 9 egg chambers expressing *GFP::Nup358; mat-Gal4* as well as HA-tagged wild-type Ran (A), HA-RanT24N which is locked in a GDP bound state (B), or HA-RanQ69L, which is constitutively bound to GTP (C). The amount of GFP-Nup358 positive structures throughout the egg chamber is drastically reduced upon HA-RanT24N expression (B, D), and increased upon HA-RanQ69L expression (C, D). Many granules were continuous with nurse cell NEs (C, yellow arrowhead), indicative of arrested fusion events. (D) Quantification of GFP-Nup358 containing volume fraction was performed via automatic segmentation of all cytosolic structures and represented as fraction of the remaining cytosol. (Bars represent mean ± SD, *** $p < 0.0001$, unpaired t-test; n[Ran] = 6

egg chambers, n[RanQ60L] = 10 egg chambers, n[RanT24N] = 9 egg chambers). **(E-G)** Ran mutant localization mirrors Rcc1 and RanGAP localization. Single confocal images of fixed stage 10 egg chambers expressing *GFP::Nup358; mat-Gal4* as well as HA-tagged wild-type Ran (E), HA-RanT24N (F), or HA-RanQ69L (G) subjected to immunofluorescence via rabbit anti-HA antibody and WGA-Alexa647 staining FG-nucleoporins. HA-RanT24N is largely localized to nurse cell and oocyte ooplasm (F). with a staining pattern indicative of chromatin and mirroring Rcc1 localization (refer to Figure 2-18A", B") HA-RanQ69L is found co-localized with Nup358 at the NE (G), nurse cell Nup358 granules (G, yellow arrowheads) and AL (G, red arrowheads), thus mirroring RanGAP localization (refer to Figure 2-18A', B'). Annulate Lamellae in RanQ69L ooplasm further show anterior enrichment and clustering at the nurse cell – oocyte border (G, red arrowheads). **(H)** Mosaic HA-RanT24N expression shows direct correlation with Nup358 condensation. High resolution confocal image of a stage 10 egg chamber as described in F. Occasional mosaic absent expression of HA-RanT24N as shown by absence of anti-HA immunofluorescences (H") leads to enlarged cells and nuclei, a more folded appearance of the NE, as well as detectable presence of Nup358 granules (H') in comparison to their absence in surrounding sister cells with higher HA-RanT24N expression.

So far, a model of AL regulation emerged, where both facilitated interactions between nucleoporin condensates by microtubules, and the action of GTP-bound Ran promote nucleoporin interaction and structural assembly (Figure 2-20A). If both of these regulatory elements function in the same pathway and in the same direction, inhibition of one should potentially diminish the effect of the other component. *RFP::Nup107; mat-Gal4; UAS-HA::RanQ69L* flies were thus fed overnight with food containing colchicine and their ooplasmic contents were assayed the following day. Whereas HA-RanQ69L expressing flies maintained on regular food exhibited strong aggregation of RFP-Nup107 positive structures in the ooplasm (Figure 2-20B), MT-depolymerization largely reverted this molecular phenotype (Figure 2-20B').

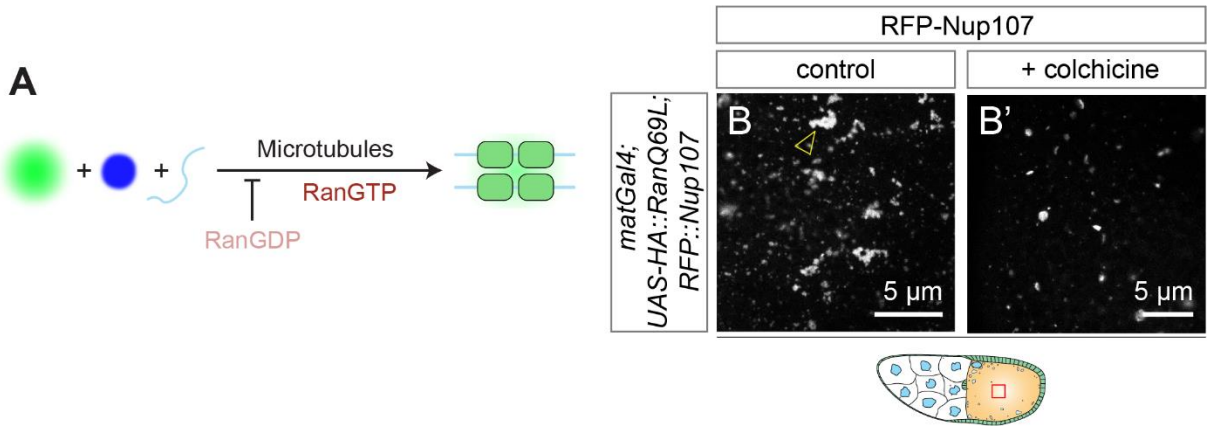

Figure 2-20: Microtubule-dependent movements and RanQ69L both promote granule interactions

(A) Schematic model of AL assembly regulation. Nup358 granules (green), oocyte-specific granules (blue), as well as membrane (light blue) interact to form AL. This interaction is positively mediated by RanGTP and microtubules (MTs) and inhibited by RanGDP. **(B-B')** MT-depolymerization prevents aberrant RanQ69L aggregation phenotype. High resolution confocal image of two stage 10 *RFP::Nup107; mat-Gal4; UAS-HA-RanQ69L* egg chambers, dissected from flies that were either fed with regular yeast paste, or with yeast paste supplemented with 100 µg/ml colchicine in 1% sucrose for 16 h. AL agglomeration observed in the RanQ69L genetic background is strongly suppressed by colchicine-induced MT-depolymerization and individual structures stay much more separated. Data was produced by Dr. Bernhard Hampoelz.

3 Discussion

How Annulate Lamellae are formed *de novo* was largely unknown. Throughout this thesis I, in close collaboration with others at EMBL, could first confirm that Annulate Lamellae are abundant in *D.m.* oocytes, establish that AL continually accumulate specifically within the ooplasm throughout oogenesis, and describe their existence as single or multi-sheet arrangements that are embedded within the ER and exhibit a surrounding exclusion zone of cellular constituents. I performed a systematic RNA localization screen, visualizing 39 nucleoporin, Ran-cycle and NTR encoding transcripts and identified two *nucleoporin* and three *importin* mRNAs that specifically accumulate around NE, AL and cytoplasmic Nup granules. This RNA enrichment differed between compartments, was independent of an intact MT network but dependent on polysome integrity, and progressively diminished upon ribosome run-off. Generation of a *GFP::Nup358* transgenic fly line led to the identification of multiple distinct classes of nucleoporin granules, each only containing a subset of all probed nucleoporins. These granules displayed spatiotemporal abundance trajectories indicative of AL precursors, and were subject to directed movements including nurse cell to oocyte transport. Consistently, I was able to visualize a limited number of ALPCs embedded in internal membrane stretches within granules. In the oocyte, MT-mediated interactions between different granules were observed and interference resulted in a greater separation of granules and reduced number of mature AL. Nucleoporin granules exhibited certain liquid-like properties and hallmarks of biomolecular condensates, such as fast intra-granule dynamics, spherical structures, and establishment of a distinct cytoplasmic milieu excluding cytoplasmic constituents without membrane enclosure. Both AL assembly and nucleoporin condensation were regulated by the small GTPase Ran, likely coordinated by Nup358-mediated recruitment of RanGAP towards Nup granules and AL, and Rcc1 localization to the ooplasm.

This work thus for the first time established a molecular framework and basic sequence of events that leads to the assembly of Annulate Lamellae, an understudied cellular organelle critical in the context of development, and abundant in a variety of other cell types. It further identified an example of local translation that occurs during the massive coordinated construction of an exceedingly large protein complex, the nuclear pore complex. Finally, it established *D.m.* oogenesis as a valuable model system for protein complex assembly research due to its spatially and temporally defined accumulation of

large stockpiles of cellular material for future use. Combined with its large size, genetic control and phenotypic readout, it will hopefully be used in the future to both build on our work on NPC assembly and local translation, as well as many other complexes. Much of this initial work was focused on describing the system and hence the majority of the underlying biochemical mechanism and its relevance in respect to local translation still awaits future determination.

3.1 Characterization of AL and their accumulation during oogenesis

Previous characterization of Annulate Lamellae was typically based on ultrastructural characterization by electron microscopy, or molecular identification by fluorescent tagging or immunofluorescence [177,178,180,186,334]. By combining the strengths of these two approaches using CLEM, I could first correlate the fluorescent signal either to mature AL (Figure 2-1) or intermediate structures (Figure 2-4) to then quantify their accumulation throughout oogenesis by live cell imaging (Figure 2-2). Both mature AL as well as putative assembly intermediates had previously been identified in a variety of tissues, but this classification was typically based solely on ultrastructural appearance and the developmental stage they were observed in [177,335,336]. By combining live cell imaging, quantification, and CLEM, I could prove and assign molecular identity of two nucleoporin markers to distinct sub-structures within such precursors (Figure 2-4, Figure 2-16) and show the appearance of ALPCs via electron tomography (Figure 2-16F-G"). This work was limited to the publicly available *GFP/RFP::Nup107* and *GFP::Nup358* produced by myself, but ongoing work within the laboratory will hopefully soon extend on this repertoire.

Another technological advance was the application of volume EM via FIB-SEM implemented by our EM core facility to the *D.m.* ooplasm, which allowed us to gain a much more holistic view of AL abundance and structural organization. While previous work was limited to 2D TEM or SEM of thin, mostly non-consecutive sections, this work includes a dataset spanning 1,200 μm^3 of a stage 10 ooplasm with 5 nm isotropic resolution and excellent staining quality of all contained organelles (Figure 2-3A). Combined with automatic identification and segmentation of AL, implemented by Helena Bragulat and our Center for Bioimage Analysis (CBA), several multi-sheet AL could be reconstructed with full 3D coverage (Figure 2-3B-C). These reconstructions confirmed previous characterizations that AL sheets are arranged in a parallel fashion, and led to novel insights about their inter-connection to the surrounding ER. Here, the added benefit of

three-dimensional information is particularly apparent. While in 2D slices or projections, many different arrangements appear to be identical (i.e. parallel stacks in this example), 3D information has previously proven crucial to determine the higher order arrangement of several stacked membrane structures including thylakoids [322], the endoplasmic reticulum [321], and the photoreceptor outer segment [337]. For AL, this showed that ALPC-containing sheets are partially shielded by membrane and partially open to the cytoplasm (Figure 2-3B-C"). They were always in continuation with ER at least on one and often both ends, and the connecting ER sheets often spanned more than two sheets in elaborate three-way junctions (Figure 2-3B", arrowheads) that are reminiscent of stroma-grana thylakoid connections [322]. While not the focus of this study, other researchers might be able to benefit from these descriptions and elucidate the molecular membrane-remodeling machineries that are involved in the creation and later resolution of these intricate arrangements upon NE insertion [84]. At regions without surrounding membrane, the AL nevertheless exhibited an extended proximal milieu that was marked by an exclusion of ribosomes and other material (Figure 2-3B, C, D, cyan arrowhead). This is particularly noteworthy as the detected *nucleoporin/importin* mRNA localization around AL is not uniform (Figure 2-7A", arrowheads). If local translation feeds (soluble) nascent proteins into the structure, then these RNAs should first be located at non-membrane shielded regions of the AL, and second lie outside the ribosome exclusion zone as they are evidently subject to active translation (Figure 2-8B). However, as there currently are no tools with sufficient sensitivity to simultaneously visualize RNA fluorescence and ultrastructure (i.e. RNA CLEM), this analysis will have to wait for new technologies to be developed; a task that I myself have recently started.

It has previously been speculated that embryonic AL are symmetric precursors that are only converted to mature asymmetric NPCs upon insertion into the NE [84]. This proposal was largely based on a general absence of asymmetric components – particularly nuclear basket components – as assessed by fractionation and proteomic identification. Nup358 on the other hand was found to be present at increased abundance as compared to the nuclear fraction. If the establishment of asymmetry at the NE depended on the Ran gradient and/or other factors establishing nucleoplasmic vs cytoplasmic identity, then the same mechanism would indeed lead to symmetric ALPCs as both sides are facing the cytosol. Here I could confirm the absence of the nuclear basket Nup153 (Suppl. Figure 2) and the presence of the cytoplasmic filament Nup Nup358 (Figure 2-10B-C, Figure 2-12A) also at ooplasmic AL. Furthermore, dual color CLEM with RFP-Nup107 and GFP-Nup358 showed a GFP-Nup358 positive region covering and surrounding multi-sheet AL and

extending uniformly to all sides (Figure 2-16E). If Nup358 were asymmetrically localized as it is in the NPC, this extended GFP-Nup358 positive zone would presumably also display asymmetric localization to only on one end of the AL; as is indeed observed at the nurse cell NE (not shown). Definitive proof of symmetric organization of ALPCs by structural methods, and elucidation of its ultimate conversion into asymmetric NPCs upon nuclear insertion will likely be subject for future research and will undoubtedly reveal valuable and more general insights into the mechanism and underlying rules of NPC assembly.

3.2 Systematic investigation of *nucleoporin* mRNA localization

My proposed objective to probe a possible involvement of RNA localization and local translation in NPC assembly was realized in the form of a systematic screen of all *nucleoporin* (and extended to Ran cycle and NTR-encoding) mRNAs throughout the egg chamber at all developmental stages (Figure 2-5). While smFISH probe sets for two *nucleoporin* transcripts did not pass the quality assessments we enforced, this nevertheless resulted in an imaging dataset covering 39 mRNAs. As it was difficult to compress such a dataset into a concise representation, I decided to display them as individual representative intensity line profiles covering the egg chamber from anterior (left) to posterior (right), centered around the nurse cell-oocyte border (Figure 2-5B, C). Whereas the majority of transcripts displayed rather flat and homogenous distributions and corresponding profiles (e.g. all Y-complex members), some RNAs displayed strong smFISH intensity and highly clustered behavior (e.g. *ran*, *pendulin*, *ketel*). Due to differences in probe labeling efficiency, binding affinities, and probe numbers per target transcript however, only limited conclusions about corresponding gene expression levels are possible. As became quickly apparent, the identification of novel RNA localizations without prior information is not trivial, as only very obvious localizations (e.g. to specific cells, to the cortex of a cell, or to the nucleus) are readily apparent without co-labeling. Finer sub-cellular localizations e.g. to the ER network or the NE can sometimes still be detected by intuition of the researcher and subsequent complementary staining (Figure 2-6B). More subtle non-random localizations such as co-localization of several RNAs, or to diffraction limited proteinaceous structures are much more challenging and are mostly missed or merely visible as clustering. Here, prior knowledge of involved molecular components by discovery based methods such as immunoprecipitation coupled to mass spectrometry or RNA sequencing are often instrumental, but were beyond the scope of

this research. I instead tried to address this by performing co-localization analysis of *nucleoporin* mRNAs in pairwise permutations of pre-selected subsets (based on structural information), but could not identify significant co-localizations after subtracting co-localization expected by chance (not shown).

3.2.1 *nucleoporin/importin* mRNA localization is likely mediated by RNC-dependent tethering

Fortunately, I was able to identify the strong clustering and co-localization of *nup153*, *nup358*, *ketel*, and *moleskin* (and *karypherin β* to a lesser extent) to specific structures that were easily identified as the nuclear envelope based on the consistently observed lower mRNA localization within nuclei (Figure 2-5B). Subsequent multicolor imaging allowed the further identification of enrichment also around other nucleoporin-containing structures such as Nup107-positive foci in both oocyte and nurse cells (Figure 2-7). The latter were later identified to represent Nup358 granules (Figure 2-11A).

Probing of its underlying mechanism by pharmacological perturbations revealed that this RNA localization mode seems to be distinct from the commonly used RBP and MT-dependent transport employed by other prominent oocytic examples such as *oskar* (Figure 2-8A', [338]). Whereas MT-depolymerization had no effect on enrichment (Figure 2-8A), it was instead highly sensitive to disruption of polysome integrity by puromycin, which induces premature nascent chain release [339]. Induction of ribosome run-off by homoharringtonine led to a gradual decrease of enrichment that correlated with the length of the coding sequence of each transcript (Figure 2-9) and was negated by simultaneous inhibition of ribosome elongation (Figure 2-9A). A possible explanation for these combined observations is thus the RNC-mediated localization of actively translating *nup153, nup358, ketel,* and *moleskin* transcripts to cellular sites containing NPCs, including NE, AL and nurse cell cytoplasmic Nup foci (Figure 3-1A). This is maintained by affinity of the nascent peptide to other factors within the NPC or granule – potentially itself – and the corresponding RNA co-recruitment via the ribosome (Figure 3-1A). During high active translation conditions, each terminating ribosome would sever this connection between nascent chain and mRNA, but would be replaced by one or several ribosomes/nascent chain(s) further upstream, thus resulting in steady-state anchoring (Figure 3-1A). Upon inhibition of translation initiation by homoharringtonine, no new ribosomes would provide nascent chain anchors and the tethering efficiency would gradually decrease, dependent only on elongation rate and length of the CDS (Figure 2-9).

Abrupt termination by puromycin on the other hand would lead to a near instant detachment of all RNAs (Figure 2-8B), whereas artificial stalling via cycloheximide would lead to stabilization (Figure 2-8C, Figure 2-9A). If these transcripts exhibit different translational capacities in each compartment, or different affinities of their nascent chain due to composition of the target structure, this could further explain the observed variation of enrichment between nurse cells and oocyte (Figure 2-7B). The necessary recognition and movement could either arise passively by random diffusion (or facilitated diffusion) and association upon chance encounter, or could be facilitated by dedicated molecular factors, analogous to RNC-mediated association to the ER via SRP (Figure 1-5D). While the initial targeting might still involve the MT cytoskeleton, at least its continuous association is independent of it (Figure 2-8A) and highly stable (persistent over 12 h colchicine feeding). Few examples of such a RNC-mediated tethering mechanism have been reported thus far [283–285]. In case of the PCM protein Pericentrin, the tethering appears to be RNC-mediated, but the transport seems to rely on active transport along MTs [284], whereas the underlying movement for ATI RNC-tethering was independent of both F-actin and MTs [283]. To dissect this further for *nucleoporin/importin* localization, future studies could perform puromycin treatment followed by washout and recovery in presence or absence of various transport inhibitors in the same egg chamber culturing and smFISH assay that I have employed throughout this work.

Within the NPC, both Nup358 and Nup153 are thought to bind via N-terminal domains [86,170,340]. Assuming the same interactions are at play for nascent chain binding, this this would aid co-translational association by allowing for more time as the N-terminus is translated first. Consistently, previous work studying heteromeric co-translational protein complex assembly has repeatedly identified N-terminally biased localization of involved interaction domains [206,291,292,304,305,341,342]. Considering the peptide-centric model for RNA attachment, it is interesting to ask what other commonalities the identified proteins display. Previous bioinformatic comparison of locally translated proteins to the remaining proteome found that they displayed both an increased tendency for intrinsically disordered regions, as well as to promote protein interactions and assembly [212]. Both of these attributes are certainly apt for Nup153 and Nup358. As described earlier, both share a set of homologous Ran-binding zinc finger domains (Figure 1-2, [87]) and large disordered stretches including FG-repeats throughout their length. Nup358 (but not Nup153) further shares a similar α-helical fold as Importin ß family members [343,344], and both Nup153 and Nup358 are key regulators of NPC assembly

(Nup153 as early initiator of interphase assembly [170]) and overall architecture (Nup358 via dimerization of cytoplasmic rings [23]). Considering this role of both proteins, local translation could conceivably represent a nucleating event for granule formation. Over time, continually translating polysomes would undergo chance encounters and remain associated, thereby gradually establishing the central nucleoporin granule and remaining at its surface as it grows. Considering the highly aggregation-prone nature of nucleoporins [59,60], this might also constitute a form of cellular quality control. By direct local translation into a favorable environment formed by other hydrophobic nucleoporins (including itself), and possibly enriched in stabilizing factors such as chaperones, the nascent chain would never be exposed to the potentially dangerous aqueous cytoplasm. Local clustering and translation at variably titled 'assembly/translation factories' or 'translation hotspots' containing the resultant and often related proteins alongside cellular chaperones was indeed also observed in several other contexts [283,284,286–288,290]. Likewise, it could also help to produce the high local concentration necessary for biomolecular condensation as will be discussed later on.

While the local translation of nucleoporins was in line with our initial objective to probe their potential role in co-translational assembly, the identification of three nuclear transport receptor RNAs came as a surprise. Almost by definition, these shuttling receptors are thought to merely be dynamic visitors of the pore, rather than stable constituents of it. Contrary to this view however, there is evidence that a certain fraction of NTRs acts as a stable and important component within the pore [345], where it is thought to modulate the permeability barrier. During NPC assembly, researchers have further reported a distinct lag phase between final maturation based on nucleoporin molecular markers and ultrastructural characterization, and the full establishment of the permeability barrier [163]. The remaining non-nucleoporin constituents that are still missing for this final maturation step are unknown but have been speculated to contain NTRs ([149,345,346]). Additionally, the high mobility of importins across the pore despite their multivalent FG-favoring interactions is thought to arise from local release on the nuclear side via binding to RanGTP [111–113]. It is however currently unclear whether such a gradient exists across ALPCs with both sides facing the cytosol. Its absence would thus remove this biased directional release and resultant flux. Particularly in such a scenario, NTRs could in fact be considered stable components of ALPCs and might thus benefit from co-translational association and insertion during assembly. This could be addressed by measuring NTR dynamics (e.g. by FRAP) at AL compared to the NE. *In vitro*, Imp4, Imp7 (homologous to Moleskin), Imp5 (homologous to Karyopherin ß-3), and

Impβ (homologous to Ketel), but not other import receptors, have all been shown to act as chaperones for highly basic substrates [135]. Perhaps this points to co-translational RNC binding of these proteins to yet-to-be identified positively charged components within granules or pores.

As already indicated, a major unanswered question is whether local *nucleoporin/importin* translation is necessary, and what molecular phenotype results from its disruption. My attempts to answer this by generating transgenic fly lines that artificially sequester certain mRNAs away from NE/AL/Nup granules did not yield any viable specimen and thus unfortunately remains unanswered. Likewise, my attempts to produce *GFP::STOP::Nup358* transgenic flies that produce essentially an identical mRNA to *GFP::Nup358,* but without translating a corresponding protein – to corroborate the sole reliance of RNA tethering on the encoded protein – also failed to produce viable offspring. While these methodologies often work well in cell culture systems and/or single-celled organisms, employing them within living animals is often challenging. However as the field is rapidly evolving, and new technologies promising less disruptive genetic methods are constantly emerging, it will be up to future research to confirm or deny these predictions and clarify these questions.

3.3 AL assembly is mechanistically distinct from NPC assembly

By pure serendipity, generation of the transgenic *GFP::Nup358* fly line based on its observed mRNA localization, revealed that Nup358 and later other nucleoporins all formed partially overlapping sets of nucleoporin granules (Figure 2-10). This subsequently evolved into the description of a novel assembly mechanism for pore complexes. Within oocytes, granule diversity was high at early stages and markers progressively became more overlapping with developmental time. By early embryogenesis, AL were the only detectable species (Figure 2-12A"', B). Within nurse cells on the other hand, this apparent progression was suppressed and Nup358 granules remained the dominant granule class throughout (Figure 2-12). Such a time-resolved distribution pattern implied the ordered progression of precursor granules into AL, an interpretation which I could further corroborate with several observations.

3.3.1 Nucleoporin granules undergo microtubule-dependent movement

First, while predominant in nurse cells where they are likely produced, Nup358 granules undergo directional transport into the oocyte within live egg chambers (Figure 2-13A-B) but not vice versa. This is however by no means efficient, as within the observed imaging window only a few out of hundreds of granules were seen to pass for a given ring canal and there was substantial movement within the nurse cells in other directions (Figure 2-13A). As the nurse cells eventually expel their cytoplasmic contents into the oocyte during so-called 'nurse cell dumping', it is possible that the majority of necessary Nup358 oocyte transport is performed during this stage. Interestingly however, at stage 12-14, nurse cells have already undergone dumping, yet there are very few Nup358 granules detected in the oocyte but still large amounts of oocyte-specific granules (Figure 2-12). Assuming all the Nup358 granules are dumped into the oocyte, they would have to be converted quickly as we did not notice a spike in oocyte Nup358 granules - although we might have missed it due to insufficient time resolution. It is possible that the oocyte prepares for this predicted flooding of nurse cell cytoplasm and Nup358 granules by stockpiling other precursor granules, and the resident oocyte-specific granule pool represents the excess. But then what happens to them between egg maturation and fertilization? Targeted degradation is one possible answer to this, but is hard to assess due to the inaccessible location of the egg during laying. Within the oocyte, the different nucleoporin granules display frequent and long-lasting interactions, occasionally resulting in fusion (Figure 2-13D) but more often persisting (Figure 2-13E) beyond the imaging time window. This might allow for the slow and regulated transfer of material. Both the directed movements and the facilitated interactions are dependent on microtubules, as evidenced by the recording of characteristic fast, linear runs along an intact MT-network in *ex vivo* oocyte squash preparations (Figure 2-13C) and the abolishment of all observed movements *in vivo* upon colchicine treatment (Figure 2-14A-A'). Importantly, the latter treatment further resulted in a substantial reduction in observed nucleoporin marker overlap, thus increasing the proportion of separate granules and decreasing the number of putative AL per our earlier definitions (Figure 2-14). The *Drosophila* ooplasm is highly viscous and remains as a compact mass for a long time after extraction into an aqueous buffer (personal observation). On top of this, oocytes, including the *D.m.* example, are exceedingly large cells of up to half a millimeter (Figure 2-10A). Resultantly, many such oocytes utilize MT-dependent movements to ensure efficient interaction between macromolecular complexes within this highly crowded environment, as evidenced by their long-standing use as models systems for MT-dependent transport

[347]. Cytosol in other cells has previously been shown to behave as a viscoelastic material [348], which allows efficient diffusion for small molecules, but behaves as a dense medium restricting movement for large assemblies [349]. As both Nup precursor granules and AL are rather large (~0.5 – 2 µm), it is not surprising that MT-dependent movements – either as directed transport or cytoplasmic streaming – are crucial for efficient mixing of precursors. How these structures are attached to potential molecular motors, or what the existence of these motors is, are open questions. Both Nup358 itself, as well as Imp ß (Ketel), which is a constituent of both Nup granules and AL (Suppl. Figure 2), have previously been shown to bind molecular motors and their adapters [98–100,129,130]. Nup358 was even shown to bind to both minus and plus-end directed motors simultaneously, thus resulting in a 'tug of war' between both directions which is employed during spindle assembly [98,99]. A similar simultaneous attachment of *oskar* mRNPs to kinesin and dynein was shown to occur during its transport to the posterior oocyte [235], so it is tempting to speculate that similar mechanisms are transporting Nup358 granules and AL.

3.3.2 Nucleoporin granules display characteristics of biomolecular condensation

The consistently spherical shape of Nup358 granules (Figure 2-15) and the previous identification of RFP-Nup107 containing structures with large, circular (in 2D sections) ribosome exclusion zones (Figure 2-4), combined with several previous studies concerning the material state of nucleoporins *in vitro* [55,63,65,68,350], led me to hypothesize that Nup358 granules represent biomolecular condensates with liquid-like properties. Many behaviors and attributes that allow insight into the material state of biomolecules, such as shape, fusion or fission events, or internal dynamics, can only be assessed above a certain size threshold, limited by the diffraction limit of most light microscopy based techniques. This renders the *in vivo* assessment of material properties cumbersome, and consequently often restricts thorough investigation to purified components in solution. Due to their confined nature within the nano-scale NPC channel, *in vivo* characterization of the properties of nucleoporins have consequently been unattainable as well. Here I discovered a naturally occurring system, where nucleoporins concentrate to mesoscale-sized entities with biological relevance, that can be probed for their behavior throughout assembly, and used as a proxy for their behavior within the mature pore. I was able to determine that Nup358 is located within the previously unidentified large ribosome

exclusion zone within Nup358 granules (Figure 2-4, Figure 2-16A-B) and of the extended exclusion zone surrounding AL (Figure 2-16E). Its underlying interactions are sensitive to 1,6-hexanediol, an agent known to interfere with hydrophobic interactions (Figure 2-17A-B), and display rapid internal recovery after photobleaching (Figure 2-17D-D"), indicating a highly dynamic nature. Nucleoporin granules were furthermore often found in layered arrangements with other granules. The underlying driving force for demixing can be explained by the preference of protein molecules to interact with each other rather than the surrounding "poor" solvent, i.e. water. If this occurs for multiple independent molecular species, the pairwise interactions between each other and between the solvent can be predictive of the resultant droplet architecture [56,327]. If the interaction energies between these two different species are sufficiently favorable, they will intermix on a molecular scale and effectively become one entity (as can be observed for Nup214 and FG-Nups, Figure 2-10D). If the interactions between each species are less favorable, multiple condensates form and co-exist that can be arranged in several distinct ways [56]:

1) They can be arranged in a shell-like architecture embedded within each other if the relative surface tensions between them is lower than with the surrounding solvent. Here the component exhibiting the worse solubility in water will be situated on the inside. Such a scenario can be observed in Figure 2-15C, with FG-Nups situated on the inside, surrounded by GFP-Nup358.

2) If the relative energetic costs of interfaces between each other are lower than of each component with water, multiple independent entities emerge.

3) If the relative energetic costs between each other and between the aqueous solvent are similar, arrangements will emerge as can be seen in Figure 2-15A, B. Such a droplet on droplet arrangement is known as Neumann's triangle [326]l, and its angles are predictive of the involved surface tensions between components.

This is particularly intriguing in this assembly context, as recent work suggested that interactions of disordered nucleoporin domains would coordinate ordered NPC assembly by what appears to be pairwise co-condensation *in vitro* [350]. The observed permutations of co-condensation here is largely consistent with the discrete steps of post-mitotic assembly that were previously determined (Figure 1-3B1). This would in turn imply that the broad order of recruitment during assembly is reflected in the material properties encoded by individual nucleoporins. Extending this paradigm to development, the layered interactions that I observed throughout this work (Figure 2-10D-E, Figure 2-11A-C, Figure 2-13D-E, Figure 2-15) could thus reflect defined steps of nucleoporin recruitment

within the established framework of AL assembly via granule interactions. Underscoring this connection, a similar role of unstructured FG-domains was previously also identified in yeast [39]. Via biochemical dissection of binding events coupled with microscopy-based confirmation of nucleoporin recruitment, these FG-repeats were shown to bind and recruit multiple scaffold nucleoporins to the NPC that were important during assembly [39].

The necessary multivalency for such observed collective condensation behavior is certainly fulfilled for several nucleoporins, including Nup358, as it harbors both 27 annotated FG repeats (Figure 1-2, *D.m.* Nup358) as well as several repeated domains including four repeated Ran binding domains (Figure 1-2). Regarding another pre-requisite, high local concentration, this might either arise spontaneously, or be facilitated by local translation. For other phase separating proteins this seems counterintuitive, as many such proteins display rapid exchange between the droplets and the surrounding solvent. FG-Nups however are amongst the most hydrophobic soluble proteins found inside the cell [48], and therefore have a high energetic barrier to enter the surrounding aqueous solvent (i.e. the cytosol). These effects could thus not be as relevant for hydrophobic nucleoporins and hence strengthen the importance of local concentration by other means. Indeed, while Nup358 granules exhibited very fast recovery kinetics during FRAP within droplets (Figure 2-17D-D"), their total fluorescence clearly stayed reduced throughout this (Figure 2-17D-D") and in fact did not recover for much longer (not shown). This suggests but does not prove, that while intra-droplet dynamics are indeed very high (i.e. liquid-like), their inter-droplet exchange via the cytosol might be rather restricted. Perhaps for nucleoporins this does not constitute a general issue, as Nups are typically sequestered within their own microenvironment within the NPC channel. During biosynthesis however, such insolubility suddenly becomes relevant; especially within this system of massive biosynthesis of NPCs. The cell thus might use phase separation to deal with this issue and prevent nucleoporin aggregation.

3.3.3 Regulation of nucleoporin condensation and AL assembly

This work was initiated by the astounding coordination necessary to assemble the massive nuclear pore complex from ~1,000 individual pieces. While I uncovered an unexpected pathway that potentially relies on biomolecular condensation rather than pairwise binary interactions to achieve this, it does not diminish but merely shift the need for coordination to another scale. Despite all the described mechanistic and molecular differences, the small GTPase Ran has previously been shown to regulate the assembly of both NPCs and

ALPCs alike, by local release of sequestered nucleoporins from NTRs [137]. As ALPC assembly occurs in the cytosol – without a nuclear compartment – I visualized the distribution of the two factors known to modulate Ran at the NE: Rcc1 on the nuclear side and RanGAP on the cytoplasmic side. In egg chambers, this revealed the strong Nup358-dependent co-localization of RanGAP to Nup358 granules, AL and the NE (Figure 2-18A-D'", Suppl. Figure 3) and, surprisingly, the enrichment of Rcc1 in the ooplasm but not the nurse cell cytoplasm (Figure 2-18B-B"). Upon entry of Nup358 granules into the oocyte, these opposing players could thus produce a local RanGDP-RanGTP gradient across each droplet. In contrast to the nuclear gradient however, the topology of this gradient would be inverted, with RanGDP on the inside, where ALPC assembly is set to occur, and RanGTP on the outside. This apparent discrepancy could potentially be remedied by utilizing nuclear export factors such as Embargoed (Crm1) for nucleoporin chaperoning instead of Ketel (Imp ß). Such an involvement of nuclear export factors in assembly has to the best of my knowledge not been reported, but this might be explained by the prevailing focus on NPC assembly at the NE. Providing initial hints that Embargoed is indeed somehow involved in this process, shRNA mediated depletion does indeed lead to alterations in both AL assembly and Nup358 condensation status, and in some cases led to a reversal of Nup358 and oocyte-specific granule spatial distribution [351]. To test this model more directly, potential future experiments could utilize RanGDP- or RanGTP-functionalized beads that have been used extensively in the *Xenopus laev*is (*X.l.*) egg extract system, and inject them into the *D.m.* ooplasm or nurse cell cytoplasm. These could then be probed for recruitment of nucleoporin proteins or even mRNAs to their surface. In *X.l.* egg extracts, such experiments were of tremendous value during establishment of the molecular rules of NPC assembly. Transferring it to this newly established animal system of ALPC assembly, where separate compartments exhibit distinct assembly capacities, would be very exciting.

The observed reduction of GFP-Nup358 and resultant RanGAP intensity at AL as compared to Nup358 granules (Figure 2-18), would further predict a progressive shallowing of this local Ran gradient during the granule to AL transition. This could thus present an elegant in-built regulatory mechanism to sense its completion. When a Nup358 granule enters the ooplasm, large amounts of Nup358 (and potentially other nucleoporin components) are available and the Ran gradient is steep, which leads to increased assembly. Upon conversion, the Nup358 and corresponding RanGAP content decreases, the gradient shallows, and assembly comes to a halt. The reason of Nup358 reduction throughout this transition could be explained by a simple measure of binding site

availability. Whereas a liquid-like condensate, analogous to a molecular meshwork, by definition has a large number of (weak) binding sites for its protein constituents, the NPC proposedly only has four binding sites per asymmetric unit [7,23], totaling to 32 per NPC. With a packing density of ~30 NPCs/μm² within the membrane, and a stacking distance of ~160 nm between membrane planes (measured across Figure 1-4), this would result in a rough maximum grafting density of 10 μM. While quite high, liquid-like biomolecular condensates can concentrate its components in the millimolar range [352,353].

To obtain more direct evidence of the regulatory role of Ran in AL assembly, I expressed protein mutants locked either in GDP (RanT24N, Figure 2-19B,F) or GTP-bound states (RanQ69L, Figure 2-19C, G) [103] and assayed the AL and Nup358 granule content within egg chambers. This revealed a diminishing influence of RanT24N, and a promoting influence of RanQ69L on the amount of GFP-Nup358 positive structures (Figure 2-19). Surprisingly, this effect was most prominent within nurse cells, where no GFP-Nup358 positive structures were detectable upon RanT24N expression (Figure 2-19B, D, F). The occasional failure to express the mutant protein in certain mosaic egg chambers (Figure 2-19H) showed that such cells still harbored Nup358 granules, whereas they were absent in all surrounding sister cells, thus showing a direct correlation between them. In contrast, RanQ69L massively promoted Nup358 condensation (Figure 2-19D) to a point where granules covered all nuclei in what appeared to be arrested fusion events (Figure 2-19C). The question remains however where Nup358 goes in case of RanT24N expression, and where the excess Nup358 comes from in the latter case. Two possibilities readily come to mind. Either the total amount of Nup358 within the egg chamber changes, or it is purely the condensation state that changes from a soluble to an assembled state. As quantification of soluble GFP-Nup358 is difficult within such thick tissue, these could thus far not be distinguished. In the former scenario, this could work by regulating transcription, translation, or protein degradation. This could be addressed by smFISH to visualize a potential increase in *nup358* transcripts, or by fluorescence correlation spectroscopy (FCS) to accurately measure the soluble protein pool. In the latter scenario, the effect of Ran on condensation behavior could be based on release from NTR-chaperoning as discussed earlier, the modification of post-translational modifications, or a variety of other mechanisms. In either case, such a pronounced effect of a regulatory protein on biomolecular condensation will be of interest for future researchers as only a few such examples have been reported thus far [332,333,354] despite the growing awareness of phase separation in biological research. This further opens up an intriguing entry point for pathological research into the effects of Ran (or other factors) on

biomolecular condensation behavior – especially in the context of NPC assembly and nucleoplasmic transport. Alterations of the nucleoplasmic transport and the permeability barrier, as is suggested by this molecular phenotype has unsurprisingly already been recognized in both aging and many diseases [48,355,356]. Within oocytes, AL aggregated at the nurse cell-oocyte border (Figure 2-19G, red arrowheads), their point of entry. This molecular phenotype was reversed by concurrent depolymerization of microtubules (Figure 2-20). This underscores that both the fine tuning of the nucleoporin assembly state by Ran and the facilitated interactions by MTs are important and work in the same direction.

3.4 Summary and model

In this study, I report the initial description of molecular events involved in Annulate Lamellae biosynthesis during *Drosophila melanogaster* oogenesis. This involves the local translation of *nup153*, *nup358*, *ketel*, and *moleskin* mRNAs around NE, AL, and newly identified nucleoporin granules in both nurse cell and oocyte compartments. RNA enrichment is independent of the MT network, but dependent on active translation and polysomes integrity, and diminishes gradually upon ribosome run-off. It is thus likely a consequence of ribosome-nascent chain mediated anchoring to the surface of such nucleoporin structures (Figure 3-1A). One prominent class of nucleoporin granule (entitled Nup358 granule) contains large amounts of Nup358 within a spherical zone most notably marked by exclusion of ribosomes, and often smaller adjacent or internal granules consisting of FG-nucleoporins and the scaffold nucleoporin Nup107 (Figure 3-1B). These display characteristics of biomolecular condensation and are predominantly situated with nurse cells. They are further transported into the oocyte via MT-dependent directed transport, where they establish frequent contact with other oocyte-specific condensates of distinct nucleoporin contents, occasionally resulting in fusion (Figure 3-1B). These interactions are also facilitated via MT-dependent movements (Figure 3-1). Over time, these likely progress into Annulate Lamellae by recruiting membrane and constructing ALPC complexes. Both the condensation behavior and the construction of AL are subject to regulation by the small GTPase Ran (Figure 3-1C), potentially controlled via distinct localizations of RanGAP to granules and Rcc1 to the ooplasm.

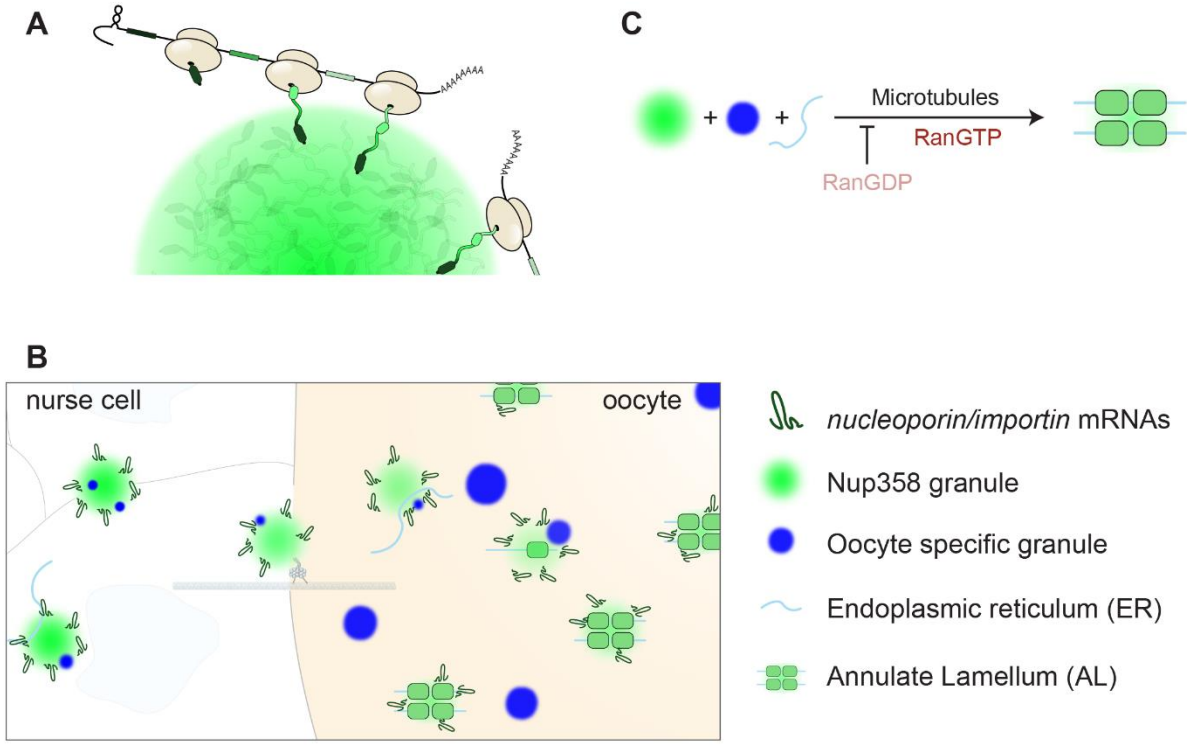

Figure 3-1: A summarizing model for AL biogenesis and RNA localization
(A) *nucleoporin/importin* mRNAs localize to AL, the NE, and Nup granules by ribosome nascent chain-dependent tethering. Affinity of the nascent peptide towards constituents within the target structure causes its attached mRNA to become enriched. As ribosomes terminate, the mRNA-nascent chain connection is severed and its enrichment would be reduced. As active translation via polysomes constantly initiates new ribosomes however, a new nascent chain takes its place and the mRNA reaches a state of steady-state anchoring. **(B)** Nucleoporin granules travel to the oocyte, where they serve as precursors for AL. Within the nurse cells, Nup358 granules containing small accumulations of FG-nucleoporins, attached *nucleoporin/importin* mRNAs and membranes, are abundant. Via active, microtubule-dependent transport, these are eventually transported into the oocyte, where FG- and Nup107-rich oocyte-specific granules are predominant. In the oocyte, granules interact and gradually assemble ALPCs within internal membranes. Eventually all nucleoporins are converted and fully stacked AL are produced to be passed on to the embryo. **(C)** Annulate Lamellae assembly occurs via Nup358 granules, oocyte-specific granules, as well as potential other nucleoporin granules and membrane. Assembly is promoted by both RanGTP and the facilitated interactions between granules based on microtubules, and assembly is suppressed by RanGDP.

I want to finish with a speculative partial model for all NPC assembly pathways:

NPC assembly is analogous to the construction of a three-dimensional jig-saw puzzle with over 1,000 pieces. As in the absence of active targeting, proteins are typically distributed throughout the cell, they will first have to be brought in close proximity in order to enable their assembly. Recent work has shown that in addition to NTR-mediated chaperoning and release, nucleoporins can also be recruited to nascent NPC assembly sites via FG-mediated interactions [39]. Once they are locally concentrated, locally restricted diffusion

would allow them to find the correct conformation for efficient binding. A rudimentary sequence of events might thus already be encoded in the pairwise attraction of certain nucleoporins based on disordered regions, as indicated *in vitro* [350] and reflected in the multi-component condensation behavior here observed in egg chambers. Nucleating assembly within molecular condensates, coupled with local translation of critical components might thus both ensure the correct sequence of events, and prevent distribution of nucleoporins throughout the cytoplasm. This might happen in all hitherto identified assembly pathways, but only in oocytes there is enough nucleoporin mass, and sufficient time available for us to see intermediate states.

4 Materials and Methods

4.1 Materials

Table 1: List of organisms and materials used throughout this work.

Reagent	Source	Identifier
Fly lines		
D.m.: w[1118]	Bloomington Drosophila Stock Center	BDSC Cat# 3605, RRID:BDSC_3605
D.m.: emGFP::nup358 PBac{y[+mDint2]=vas-Cas9}VK00027	this work	N.A.
*D.m.: w*wg^{Sp-1}CyO; P{mGFP-Nup107.K}9.1*	Bloomington Drosophila Stock Center, [357]	BDSC Cat# 35514, RRID:BDSC_35514
*D.m.: w*wg^{Sp-1}/CyO; P{mRFP-Nup107.K}7.1*	Bloomington Drosophila Stock Center, [357]	BDSC Cat# 35518, RRID:BDSC_35518
D.m.: P[w+, sqhp> Gap43::mCherry]/Fm7; Sb/TM6 Tb	Bloomington Drosophila Stock Center	N.A.
D.m.: y[1] sc[*] v[1]; P{y[+t7.7] v[+t1.8]=TRIP.HMS00865}attP2	Bloomington Drosophila Stock Center	BDSC Cat# 34967, RRID:BDSC_34967
D.m.: P{w$^+$,UASp-HA(3).Ran}	[103]	N.A.
D.m.: P{w$^+$,UASp-HA(3).Ran^{T24N}}	[103]	N.A.
D.m.: P{w$^+$,nanosGal4:VP16}; y^{1}w^{67c23}; P{w$^+$,UASp-HA(3).Ran^{Q69L}}	[103]	N.A.
D.m.: w[*]; P{w[+mC]=UAS-ChRFP::Tub}2	Bloomington Drosophila Stock Center	BDSC Cat# 25774, RRID:BDSC_25774
Antibodies and stains		
Mouse monoclonal anti-BJ1 (Rcc1) (1:20 dilution)	[329]	BJ43
Rabbit polyclonal anti-RanGAP (1:500 dilution)	Sigma-Aldrich	Cat#ABN1674
Rabbit anti-Nup153 (1:500 dilution)	[358]	N.A.
Rabbit anti-Nup214 (1:500 dilution)	[359]	N.A.
Mouse monoclonal anti-Gp210 (1:50 dilution)	Developmental Studies Hybridoma Bank	DSHB Cat# agp26.10, RRID:AB_528270

Mouse monoclonal anti-Nuclear Pore Complex Proteins mAb414 (1:500 dilution)	BioLegend	Cat# 902907, RRID:AB_10718044
Rabbit polyclonal anti-HA (1:500 dilution)	Sigma-Aldrich	Sigma-Aldrich Cat# H6908, RRID:AB_260070
Wheat Germ Agglutinin, Alexa Fluor™ 647 conjugate (1:500 dilution)	ThermoFisher Scientific	Cat#W32466
Wheat Germ Agglutinin, Tetramethylrhodamine (TMR) conjugate (1:500 dilution)	ThermoFisher Scientific	Cat#W849
bisBenzimide H 33342 trihydrochloride (Hoechst)	Sigma-Aldrich	Cat#B2261
Chemicals/Reagents/Enzymes		
Formamide (≥99.5%)	Sigma-Aldrich	Cat#F9037
Triton-X-100	Sigma-Aldrich	Cat#T8787
Deoxyribonucleic acid sodium salt from salmon testis	Sigma-Aldrich	Cat#D1626
Vanadyl ribonucleoside complex	Sigma-Aldrich	Cat#94742
Dextran sulfate	Sigma-Aldrich	Cat#D8906
Albumin from bovine serum	Sigma-Aldrich	Cat#A7906
16% Paraformaldehyde	Science Services	Cat#E15710
Schneider's Drosophila Medium	ThermoFisher Scientific	Cat#21720001
Fetal Bovine Serum	Sigma-Aldrich	Cat# F7524
Insulin from bovine pancreas	Sigma-Aldrich	Cat#I6634
Puromycin dihydrochloride	ThermoFisher Scientific	Cat#A1113803
Cycloheximide	Sigma-Aldrich	Cat#C1988
Homoharringtonine	Sigma-Aldrich	Cat#SML1091
Colchicine	Sigma-Aldrich	Cat#C9754
Ficoll® PM 70	Sigma-Aldrich	Cat#F2878
Acetone, Glass Distilled	Electron Microscopy Sciences	Cat#10015
Lowicryl® HM20 Non-polar, Hydrophobic, -70ºC Embedding Kit	Polysciences	Cat# 15924-1
Durcupan™ ACM	Sigma-Aldrich	Cat#44613
Uranyl Acetate	Agar scientific	Cat#AGR1260A

Osmium tetroxide	SERVA	Cat#31251.03
Amino-11-ddUTP	Lumiprobe	Cat# A5040
Atto 565 NHS-ester	ATTO-TEC	Cat#AD565-31
Atto 633 NHS-ester	ATTO-TEC	Cat#AD633-31
Dimethyl sulfoxide (DMSO)	Sigma-Aldrich	Cat#67-68-5
Terminal deoxynucleotidyl transferase (TdT)	ThermoFisher Scientific	Cat#EP0162
Linear Acrylamide	ThermoFisher Scientific	Cat# AM9520
Sodium acetate	Sigma-Aldrich	Cat#S2889
ProLong Diamond mounting medium	Life Technologies	Cat#P36961
Oligonucleotides		
AS375 (sgRNA fwd primer): CTTCGTTTACAACGCGAAAAGAAG	Sigma-Aldrich	N.A.
AS376 (sgRNA rev primer): AAACCTTCTTTTCGCGTTGTAAAC	Sigma-Aldrich	N.A.
smFISH probe oligonucleotides (see Table S1 in [351])	Sigma-Aldrich	N.A.
Plasmids		
pAS095 (pUC19-nup358_homology-loxP-GMR-3P3-EGFP-tubulin3'UTR-loxP-emGFP-nup358_homology)	This work	N.A.
pUC19	Addgene	RRID:Addgene_50005
pU6-BbsI-chiRNA	Addgene; [360]	RRID:Addgene_45946

4.2 Methods

Correlative light and electron microscopy (CLEM)

For CLEM, *D.m.* egg chambers of young flies were dissected in S2 Schneider's *Drosophila* medium + 10% FCS, 0.4 mg/ml insulin by holding onto the torso with a pair of fine forceps (DUMONT #5) and pulling from the distal tip of the abdomen with the other pair. Individual ovarioles and then egg chambers were separated with a pair of tungsten needles. Egg chambers were subjected to high pressure freezing (HPM010, AbraFluid) in the same medium supplemented with 20% Ficoll (70 kDa). Freeze substitution with 0.1% uranyl acetate in acetone was performed at -90°C for 48 h (EM-AFS2, Leica Microsystems). Temperature was increased to -45°C at a rate of 3.5°C/h at which it remained for another 5 h. Samples were rinsed in acetone and infiltrated with Lowicryl HM20 resin during slow heating to -25°C and polymerized using UV light for 48 h, followed by slow heating to + 20°C at 5°C/h. The block was trimmed with a razorblade and sections of 200 – 300 nm thickness were cut on a microtome (Ultracut UCT, Leica) with a diamond knife, and picked up onto carbon-coated copper 200 mesh grids. For widefield fluorescence microscopy, the grid was placed onto a ~30 µl drop of water on a #1.5 coverslip and covered with another coverslip, separated by a layer of vacuum grease. Imaging in GFP and or RFP channels was performed on an Olympus IX81 microscope equipped with an Olympus PlanApo 100x 1.4 NA oil immersion objective.

After imaging, the grid was recovered, dried and subjected to post-staining with Reynolds lead citrate and Uranyl acetate. The fluorescence map was loaded into the SerialEM software [361] and desired positions acquired first in low magnification and subsequently as high magnification (15,500x) tilt series on a FEI Tecnai F30 TEM microscope. Tomograms were reconstructed using etomo in the IMOD software package [362]. Correlation was performed using common cellular markers, such as mitochondria or lipid droplets between fluorescent and electron images via rigid, linear transformation in ec-CLEM [363] in the bioimaging platform Icy [364]. The 2D fluorescence image was then overlaid with a central slice of the acquired 3D tomogram.

Focused ion beam milling coupled to scanning electron microscopy (FIB-SEM)

D.m. egg chambers were dissected and high pressure frozen as described above, and freeze-substitution was performed with 1% osmium tetroxide, 0.2% uranyl acetate and 5% water dissolved in acetone at -90°C for 64 h. The sample was heated to -30°C at a rate of 5°C/h and remained at 4 h, before heating to +20°C at 5°C/h and again incubated for 5 h. Samples were washed in acetone and incubated in 0.1% thiocarbonohydrazide and 10% water in acetone at room temperature for 20 min. Samples were washed in acetone and incubated with 2% osmium tetroxide in acetone in a microwave processor (PELCO Biowave Pro, Ted Pella Inc.). Samples were embedded in Durcupan ACM epoxy resin. The polymerized resin block was pre-trimmed in an ultramicrotome (UC7, Leica Microsystems) to expose the ooplasm and a 12 µm x 12 µm area was acquired at 5 nm resolution up to a depth of ~11 µm on a Zeiss Crossbeam 540 FIB-SEM instrument. Individual images were aligned using a custom script within the EMCF for cross-correlation between regions across image planes. Automatic AL identification and segmentation was performed using a Trainable Weka Deep Segmentation plugin [365] in FIJI [366]. Segmentation of multi-sheet AL was performed in IMOD [362].

Fly husbandry

All Drosophila melanogaster fly stocks were kept on standard cornmeal agar at 23°C in round bottom vials. For extended storage, flies were kept at 18°C and for enhanced growth at 25°C. 24 h prior to an experiment, a desired amount of young females (<7 days) and roughly half the amount of males were transferred to a fresh vial, and freshly prepared yeast paste was added.

Culturing and live cell imaging of *D.m.* egg chambers

Flies were dissected as described above and placed into a 15 µl drop of S2 Schneider's *Drosophila* medium + 10% FCS, 0.4 mg/ml insulin on a coverslip. A drop of Voltalef 10S was placed next to the medium, forming an interface between them. A single ovariole was pulled into the oil using fine tungsten needles, thus forming a small enclosed volume of medium constricting the egg chamber. For live imaging of FG-Nups, 100 µg/ml WGA-Alexa647 was microinjected into individual egg chambers under oil. The coverslip was then placed onto an inverted fluorescence confocal microscope (Leica SP8 or Zeiss

LSM780) equipped with a 63x/1.4 NA oil immersion objective and images or time series were acquired.

For *ex vivo* squash preparations, either the oocyte or the nurse cells were squeezed out under the oil using the tungsten needles.

For colchicine treatment, flies were selected 24 h before and placed into a fresh, empty round bottom vial for 8 h to induce starvation. Flies were then placed over night into a fresh vial with cornmeal agar and either regular yeast paste, or yeast paste supplemented with 100 µg/mL colchicine in 1% Sucrose for 16 h.

For 1,6-hexanediol treatment, dissected egg chambers were imaged in 100 µl S2 Schneider's *Drosophila* medium + 10% FCS, 0.4 mg/ml insulin within a MATEK imaging dish, covered by a coverslip thus creating a small cavity between the two coverslips. Medium was gently removed from the side and replaced with medium supplemented with 5% 1,6-hexanediol during imaging.

smFISH probe synthesis

smFISH probes were designed using the Stellaris® online probe designer against transcript regions common to all transcript isoforms if possible. 18 – 22 nt long ssDNA oligonucleotides were purchased in plates from Sigma-Aldrich at 250 µM dissolved in water and all oligos per transcript were pooled. Atto dye-conjugated ddUTP was produced via combination of two-fold molar excess of dye-NHS-ester (Atto 565 NHS-ester or Atto 633 NHS-ester) over Amino-11-ddUTP and 100 mM $NaHCO_3$ (pH 8.3). The mixture was incubated for 3 h at room temperature in the absence of light. 10 mM Tris-HCl (pH 7.4) was added and the concentration was adjusted by addition of ddH_2O to 5 mM. An enzymatic labeling reaction was prepared with 1 nmol ssDNA oligonucleotides, 5x molar excess of Atto565-ddUTP or 3x molar excess of Atto633-ddUTP, 1x TdT reaction buffer, and 6 – 12 mU Terminal deoxynucleotidyl transferase (TdT) per pmol of oligonucleotides. The mixture was incubated at 37°C overnight and purified via ethanol precipitation. The labeled DNA pellet was resuspended in 25 µl ddH_2O and the degree of labeling and concentration was determined by UV/Vis absorption measurements at the wavelength of the dye (565 nm and 633 nm respectively) and of the DNA (260 nm). Calculations are described in [220].

smFISH hybridization and imaging

All steps were performed in 1.5 ml reaction tubes. Dissection of ovaries was performed as described above, but were left intact and either directly transferred into fixation buffer (2% PFA, 0.05% Triton X-100 in PBS) for 20 min, or incuated in S2 Schneider's *Drosophila* medium + 10% FCS, 0.4 mg/ml insulin supplemented with 200 µM puromycin, 100 µg/ml cycloheximide, 5 µM homoharringtonine for 15 min on an orbital shaker for perturbation experiments, followed by fixation. Colchicine treatment of flies was performed as described above. After fixation, ovaries were washed 3x in PBSTX (PBS, 0.1% Triton X-100) for 5 min, and pre-hybridized in 100 µl hybridization buffer (2x SSC, 10% formamide, 0.1% Tween-20, 2 mM vanadyl ribonucleoside complex, 100 µg/ml salmon sperm DNA, 10% dextran sulfate, 20 µg/ml BSA) at 37°C. smFISH probes were added to 100 µl hybridization buffer to a final concentration of 1 nM per individual probe and pre-heated to 37°C for 20 min. Pre-hybridization buffer was removed, hybridization buffer + smFISH probes were added and incubated at 37°C overnight in the dark. Hybridization buffer was removed and samples were rinsed once and washed twice for 30 min with 500 µl of pre-heated wash buffer (2x SSC, 10% formamide, 0.1% Tween-20). For concurrent staining, WGA-Alexa647 was added at 2 µg/ml during the last wash step. Wash buffer was removed, samples were transferred to room temperature and rinsed 4x with PBSTX. Ovaries were mounted in 50 µl ProLong Diamond mounting medium. Images were acquired on a Leica SP8 confocal microscope equipped with hybrid detectors, 488 nm, 561 nm and 633 nm laser lines and a 63x/1.4NA oil immersion objective. Stimulated emission depletion (STED) microscopy was performed on a Abberior STED/RESOLFT microscope equipped with a 60x 1.3NA water objective.

Generation of *GFP::Nup358* transgenic fly line

Transgenic flies were constructed by insertion of emeraldGFP in-frame into the endogenous *nup358* locus (*GFP::Nup358*) as described in [235]. For this, *D.m. w[1118]; PBac{y[+mDint2]=vas-Cas9}VK00027* flies were injected with a pU6-BbsI-chiRNA plasmid carrying an sgRNA (gTTTACAACGCGAAAAGAAGTGG) displaying complementarity against a region across the *nup358* start codon. sgRNA expression was under control of a U6 promoter and was cloned by annealing commercial oligonucleotides (AS375/AS376), digestion of nucleotides and plasmid via BbsI, and ligation via T4 DNA ligase. The guide RNA was designed via the flyCRISPR Target Finder tool (http://flycrispr.molbio.wisc.edu). Homologous recombination was enabled by co-injection

of pAS95 carrying a loxP-GMR-3P3-EGFP-tubulin3'UTR-loxP-emGFP cassette with 600 bp homologous sequences flanking the insert. Sequences were homologous to 600 bp up- and downstream of the start codon to result in in-frame insertion of emeraldGFP. Genomic amplification and subsequent sequencing of *GFP::Nup358* flies revealed in-frame insertion with a small deletion of one codon, which translates to Lys6. Hatched flies were first crossed to *w[1118]* flies and to double balancer, and the marker cassette was later removed by Cre-mediated recombination. Flies were ultimately crossed to become homozygous and displayed no obvious phenotypes.

Immunofluorescence staining and imaging of *D.m.* egg chambers

For immunofluorescence, flies were dissected as described under *smFISH hybridization and imaging*. Ovaries were fixed in fixation buffer (2% PFA, 0.05% Triton X-100 in PBS) for 20 min, washed 3x 5 min in PBSTX, and incubated in 2x SSC, 0.1% Triton X-100, 0.2 mg/ml BSA at 37°C overnight. The sample was then incubated with primary antibody in the same buffer for 3 h at room temperature under constant shaking. Primary antibody was removed and washed 2x 10 min, followed by secondary antibody incubation for 1 – 2 h in the same buffer. In case of WGA staining, WGA-Alexa647 was added at 2 µg/ml during this incubation. Ovaries were rinsed 3x and washed 3x 10 min in the same buffer and mounted in 50 µl ProLong Diamond. Antibodies and concentrations used are listed under Materials. Sample imaging was identical as stated above and either performed on a Leica SP8 or Zeiss LSM780 confocal microscope.

Selective plane illumination microscopy (SPIM) of *GFP::Nup358* egg chambers

SPIM imaging of live *GFP::Nup358* egg chambers was performed in collaboration with Dimitri Kromm (Hufnagel group, EMBL) on their custom built MuVi-SPIM setup [367]. This consists of two 20x, water dripping, 1.0 NA (XLUMPLFLN20XW) detection objectives, as well as two 10x, water dipping, 0.3 NA (CFI Plan Fluor 10X W) illumination objectives. Time series was acquired at 0.195 µm pixel size and 1.5 µm z-spacing with a 30 sec frame rate over ~6 h in confocal mode [368]. Egg chambers were mounted in thin transparent plastic tubing in S2 Schneider's *Drosophila* medium + 10% FCS, 0.4 mg/ml insulin.

Fluorescence recovery after photobleaching (FRAP)

For live egg chamber FRAP, *GFP::Nup358* egg chambers were dissected and prepared under oil as described above, and mounted on an inverted Olympus FV3000 confocal microscope with a 60x/1.3 NA silicone objective. For *ex vivo* oocyte squash recordings, samples were prepared as described above. Imaging of GFP-Nup358 signal was performed with a 488 nm excitation laser at low dose, with a frame rate of 260 ms for *in vivo* recordings and 140 ms for *ex vivo* recordings. To initiate bleaching, the laser was set to maximum power within one pixel, which resulted in bleaching of a diffraction-limited area inside granules. Bleaching was performed for one frame without interruption of imaging. Prior to bleaching, 10 frames were acquired to avoid/estimate adverse effects of recording, and after bleaching, recording was continued for a total of 200 - 300 frames. Due to the relatively quick movements of granules both *in vivo* and *ex vivo*, it was difficult to avoid disapppearance of granules throughout the entire imaging window and so I was limited to the depiction of recovery dynamics of individual granules. Recorded recovery movies were registered using the MultiStackReg plugin [369] in FIJI [366].

Image analysis and quantification

Image quantification of RFP-Nup107 intensity across oogenesis

Integrated raw RFP-Nup107 signal intensity was measured within a mask covering either nurse cells or oocytes of fixed *RFP::Nup107* egg chambers in FIJI [366]. The analysis resulted from maximum z projection of several confocal slices, collectively covering ~5 µm. Plotted is the raw integrated intensity (± SD) in the respective compartments across indicated developmental stages.

Quantification of AL and nucleoporin granule abundances

For quantification of granule/AL proportions across oogenesis and the embryo, *GFP::Nup358; RFP::Nup107* transgenic egg chambers were dissected, fixed and stained with WGA-Alexa647 as described above. Foci were classified according to their relative staining intensities, with Nup358 granules representing bright, round GFP-Nup358 positive foci with limited or no RFP-Nup107/FG-Nup signal, oocyte-specific granules showing strong RFP-Nup107 and/or FG-Nup signal and no GFP-Nup358 signal, and AL consisting of all three components. For stages 5 - 11, foci were counted in both compartments and counting was limited to the oocyte/embryo in late stages as nurse cells underwent cell death (N.D.)

Intensity line profiles

Intensity line profiles were produced in FIJI by averaging 18 pixels for smFISH analysis in Figure 2-5A and 10 pixels in Figure 2-18F', G', H'. For smFISH intensities, intensities of both non-overlapping subsets were summed as displayed in panel B. The line profile was centered at the nurse cell – oocyte border and represents the distance in 100 µm major ticks along the x axis, and the measured fluorescence intensity in arbitrary units from 0 to 130 on the y-axis. As moleskin showed significantly higher peak intensities as all other transcripts, its y-axis was capped at 130 for improved comparison and overall visualization. Areas for line profiles were chosen in representative egg chambers of roughly the same stage and performed at similar z heights. Lines were chosen to cross one nurse cell nucleus. Microscope settings, laser lines and objectives, as well as dyes were kept constant but labeling efficiency, number of probes and background might vary between probe sets. smFISH oligos used are listed in Table S1 in [351].

Quantification of GFP-Nup358 volume fraction within egg chambers

GFP::Nup358; mat-Gal4 transgenic flies were crossed into either *UASp-HA::Ran*, *UASp-HA::RanT24N* or *UASp-HA::RanQ69L* transgenic flies described in [103]. Ovaries of female offspring of the correct genotype were dissected and subjected to immunofluorescence and imaging as described above. The resultant confocal volumes were used to train a machine learning automatic segmentation model via the pixel classification modality in Ilastik (version 1.3.2) [370]. The model was trained on a single *GFP::Nup358; mat-Gal4; UASp-HA::RanQ69L* stage 10 egg chamber to segment cytoplasmic GFP-Nup358 signal but not nuclear signal and then transferred in batch mode to all other egg chambers of all genotypes. The quality of segmentation was compared to manual segmentation and found to be of excellent quality. The resultant semantic segmentation was converted to instance segmentation using the MorphoLibJ plugin [371] and the volume of all combined granules was measured in via the 'Analyze Regions 3D' option. The volume fraction of all granules was calculated as the combined volume of cytoplasmic GFP-Nup358 signal divided by the total cytoplasmic volume of nurse cells and oocyte (excluding nuclei and follicle cells). Bars represent mean ± SD and p-value was calculated using the unpaired t-test in GraphPad Prism.

Temporal projections

To display movements of granules across time series, movies were subjected to temporal projection via the 'Temporal-Color Code' command in FIJI [366] using the Rainbow LUT.

smFISH image quantification

Co-localization analysis

Co-localization analysis to verify each probe set used in this study was performed by concurrent smFISH hybridization of two non-overlapping probe sets (labeled with Atto 565 and Atto 633 respectively) targeting the same transcript within the same sample as described above. The resultant image stacks covered a volume of ~50 µm x 50 µm x 3.3 µm with 18 z slices for both channels. Image stacks were subjected to deconvolution (via the Huygens Essential Software package) with calculated PSF based on microscope specifications. Individual smFISH spots were detected by automatic segmentation using the _xsPT FIJI plugin [220,372] via Gaussian fitting of 2D signal intensities and tracking in the z-direction. Particles were filtered based on their appearance within at least three consecutive imaging planes. Objects were then analyzed in R using ggplot2 library [373]. For every 3D particle identified in the reference channel, its intensity as well as the corresponding intensity in the target channel was measured and displayed as a single point on a scatter plot. The reference and target channels were then reversed and this procedure was repeated. This typically resulted in a linear relationship between the two channel intensities.

Quantification of shRNA-mediated *nup358* depletion

smFISH hybridization and imaging in egg chambers expressing shRNAs targeting *nup358* or *white* was performed as described above and smFISH objects were automatically identified as above. The number of identified smFISH objects was normalized to 1,000 μm^3 volume and plotted as single data points separately for each compartment. Bars represent mean ± SD. The knockdown efficiency was calculated as fraction of the mean number of objects in *nup358* vs *white* shRNAs for each compartment and p-value was calculated using the unpaired t-test in GraphPad Prism.

Calculation of RNA enrichment scores

To calculate RNA enrichment scores, smFISH hybridization and imaging was performed in *GFP::Nup107* egg chambers as described above. The resulting image stacks were then binned by maximum z projection of four consecutive confocal slices covering 0.72 µm. The GFP channel was used for thresholding in FIJI, followed by manual selection of relevant structures either at the NE, or cytoplasmic foci. The selection was evenly dilated by 400 nm in all directions except at the NE, where dilation was only performed towards the cytosol. Within this selection, the integrated fluorescence intensity of all smFISH

channels was measured and normalized to the measured area. The selection was inverted to cover the remaining cytosol and repeated. Non-cytoplasmic regions such as follicle cells and nuclei were excluded. Enrichment was calculated as the average intensity within the first selection divided by the average intensity within the second selection and plotted for each transcript. Corresponding bars represent mean ± SD. Each data point corresponds to the average enrichment score for an entire volume averaged over several foci.

For HHT-induced ribosome run-off assay, each enrichment score at indicated time points was further normalized to the average enrichment score of that transcript at t = 0. Values were displayed as mean ± SD.

List of Figures

Publications

The following publication was based on this study

*these authors contributed equally

Hampoelz, B.*, Schwarz, A.*, Ronchi, P., Bragulat-Teixidor, H., Tischer, C., Gaspar, I., Ephrussi, A., Schwab, Y. and Beck, M., 2019. Nuclear Pores Assemble from Nucleoporin Condensates During Oogenesis. *Cell*, 179(3), pp.671-686.

Other publications

Schwarz, A. and Beck, M., 2019. The Benefits of Cotranslational Assembly: A Structural Perspective. *Trends in cell biology*. 29, 791–803

5 Supplemental Data

5.1 Supplemental Figures

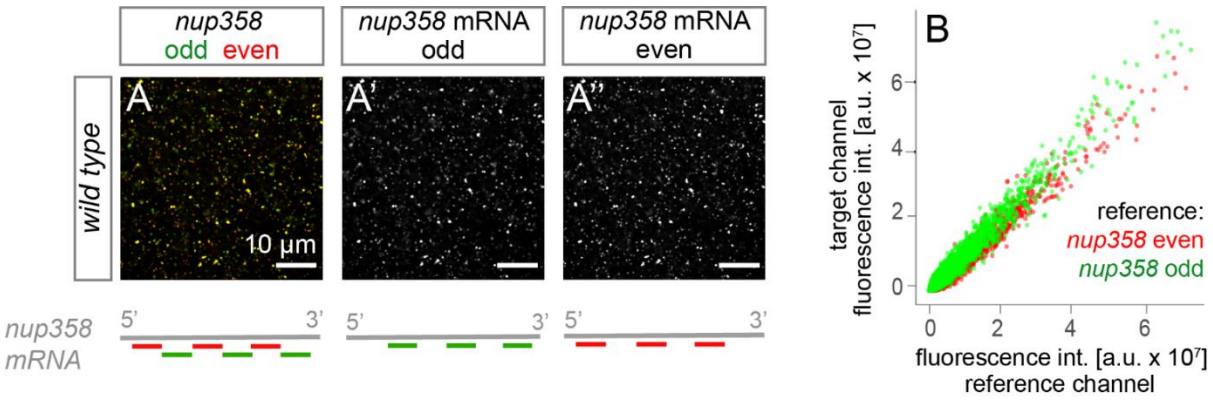

Suppl. Figure 1: smFISH probe validation
(A-A") Single channel and composite high magnification confocal images of smFISH hybridization in *GFP::Nup107* egg chambers. Each probe set targeting a certain mRNA was split into two non-overlapping subsets (odd/even corresponding to green/red in the accompanying schematic), labeled with Atto633 and Atto565 respectively, and hybridized to the same specimen. Both independent sub-sets show a high co-localization that is confirmed by intensity comparison of automatically detected smFISH foci (B). For each identified smFISH spot detected in a reference channel, its intensity is displayed as a function of the corresponding signal intensity in the target channel. Ideal probe sets show both a high level of co-localization and a high degree of linearity between respective channel intensities.

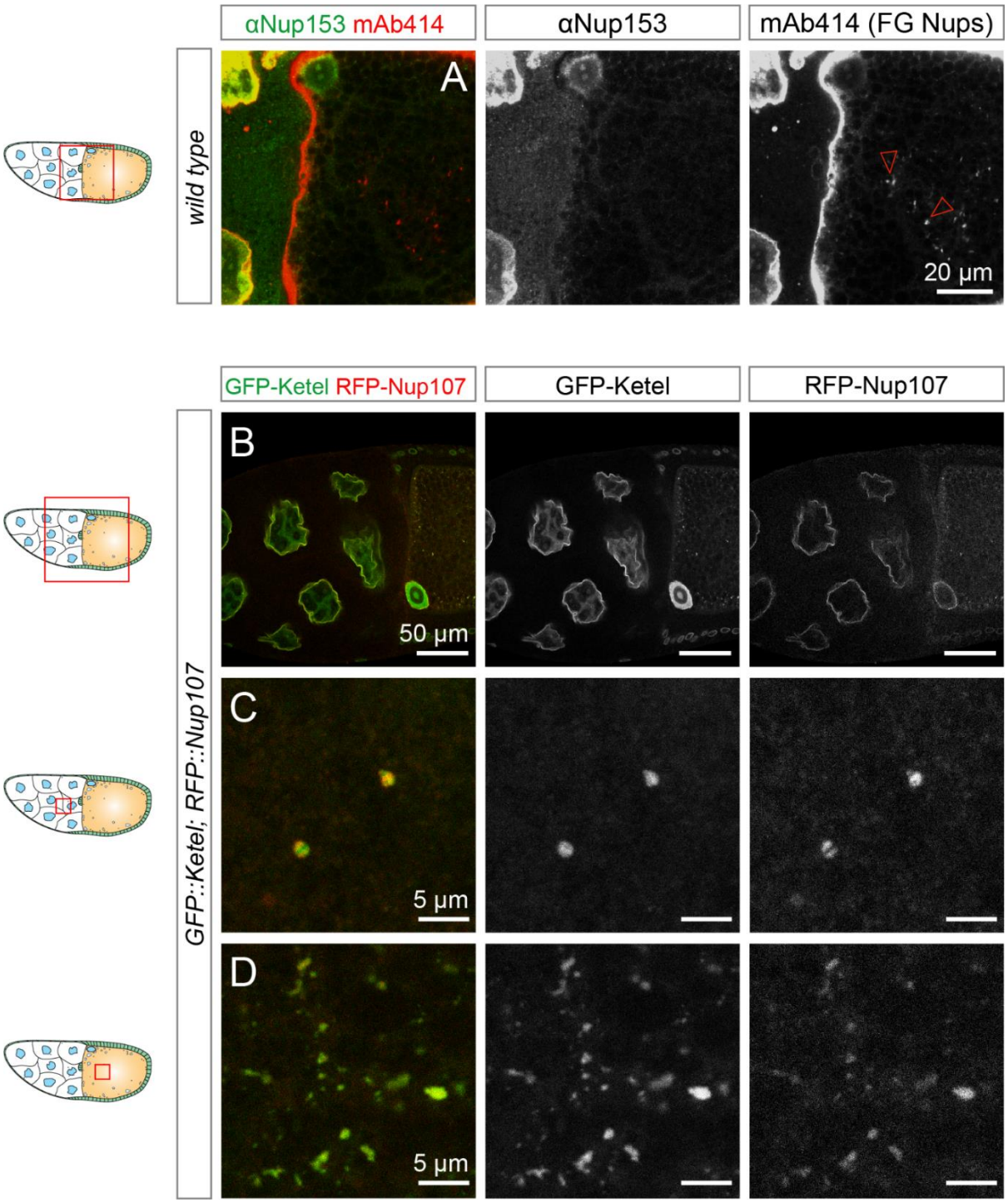

Suppl. Figure 2: Nup153 and Ketel localization throughout the egg chamber
(A) Nup153 localizes to the NE but not the cytosol. Single confocal images of a fixed stage 10 *wild type* egg chamber subjected to immunofluorescence via rabbit anti-Nup153 and mouse mAB414 (targeting FG-nucleoporins) antibodies. Nup153 is localized at the NE in nurse cells, but not at mAB414 positive cytoplasmic foci in either the nurse cell or oocyte cytoplasm (red arrowheads). **(B-D)** Ketel co-localizes with RFP-Nup107 throughout the egg chamber. Single confocal images of a fixed stage 10 *GFP::Ketel; RFP::Nup107* egg chamber. GFP-Ketel is localized at the NE as well as the nuclear interior in nurse cells (B), and strongly enriched in a shell-like architecture within the oocyte nucleus (B). In addition, GFP-Ketel is located at RFP-Nup107 positive, round foci in nurse cells (C) and at several structures throughout the oocyte (D), likely representing AL. Data for panel A was acquired by Dr. Bernhard Hampoelz.

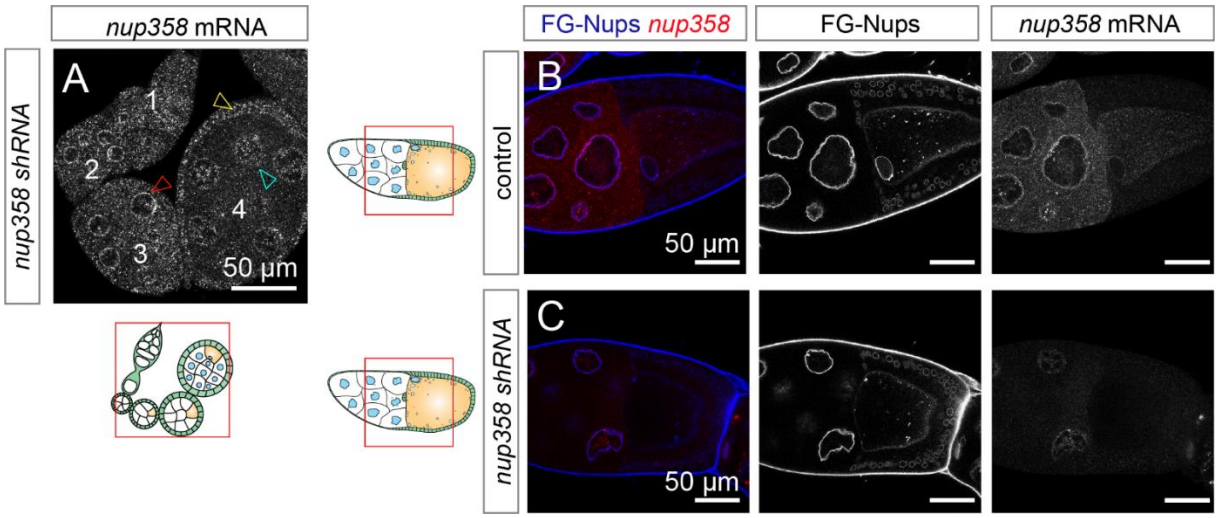

Suppl. Figure 3: shRNA-mediated knockdown of *nup358*
(A) Efficient *nup358* depletion is only achieved from stage 4 onwards. Single confocal images of *nup358* smFISH hybridization in egg chambers expressing *nup358* targeting shRNA in the germline. Surrounding follicle cells were unaffected by germline restricted shRNA depletion. Efficient knockdown was achieved in the cytoplasm (but not the nucleoplasm) of egg chambers starting at stage 4. **(B-C)** *nup358* depletion in stage 10 egg chambers. Example confocal images of *nup358* smFISH hybridization in egg chambers expressing *nup358* targeting shRNA or control egg chambers. Total amount of smFISH signal was significantly reduced in both nurse cell and oocyte cytoplasm, but not in the nuclear interior (for quantification refer to Figure 2-18C)

6 Bibliography

1 Hooke, R. (1665) *Micrographia : or some physiological descriptions of minute bodies made by magnifying glasses. With observations and inquiries thereupon.*, London : Printed by Jo. Martyn, and Ja. Allestry.

2 Schrödinger, E. What is Life? The Physical Aspect of the Living Cell. . (1944)

3 Alberts, B. *et al.* (2008) *Molecular biology of the cell*, Garland Science.

4 Ali, M.H. and Imperiali, B. (2005) Protein oligomerization: How and why. *Bioorg. Med. Chem.* 13, 5013–5020

5 Marsh, J.A. and Teichmann, S.A. (2015) Structure, Dynamics, Assembly, and Evolution of Protein Complexes. *Annu. Rev. Biochem.* 84, 551–575

6 Reichelt, R. *et al.* (1990) Correlation between structure and mass distribution of the nuclear pore complex and of distinct pore complex components. *J. Cell Biol.* 110, 883–894

7 Ori, A. *et al.* (2013) Cell type-specific nuclear pores: a case in point for context-dependent stoichiometry of molecular machines. *Mol. Syst. Biol.* 9,

8 Ishii, K. *et al.* (2002) Chromatin boundaries in budding yeast: The nuclear pore connection. *Cell* 109, 551–562

9 Galy, V. *et al.* (2000) Nuclear pore complexes in the organization of silent telomeric chromatin. *Nature* 403, 108–112

10 Heun, P. *et al.* (2001) Chromosome dynamics in the yeast interphase nucleus. *Science (80-.).* 294, 2181–2186

11 Menon, B.B. *et al.* (2005) Reverse recruitment: The Nup84 nuclear pore subcomplex mediates Rap1/Gcr1/Gcr2 transcriptional activation. *Proc. Natl. Acad. Sci. U. S. A.* 102, 5749–5754

12 Raices, M. *et al.* (2017) Nuclear pore complexes and regulation of gene expression. *Curr. Opin. Cell Biol.* 46, 26–32

13 Goldberg, M.W. Nuclear pore complex tethers to the cytoskeleton. , *Seminars in Cell and Developmental Biology*, 68. 01-Aug-(2017) , Elsevier Ltd, 52–58

14 CALLAN, H.G. and TOMLIN, S.G. (1950) Experimental studies on amphibian oocyte nuclei I. Investigation of the structure of the nuclear membrane by means of the electron microscope. *Proc. R. Soc. London. Ser. B - Biol. Sci.* 137, 367–378

15 Gall, J.G. (1967) Octagonal nuclear pores. *J. Cell Biol.* 32, 391–399

16 Unwin, P.N.T. and Milligan, R.A. (1982) A large particle associated with the perimeter of the nuclear pore complex. *J. Cell Biol.* 93, 63–75

17 Huy Bui, K. *et al.* (2013) Integrated Structural Analysis of the Human Nuclear Pore Complex Scaffold. *Cell* 155, 1233–1243

18 Kosinski, J. *et al.* (2016) Molecular architecture of the inner ring scaffold of the human nuclear pore complex. *Science (80-.).* 352, 363–365

19 Rout, M.P. *et al.* (2000) The Yeast Nuclear Pore Complex. *J. Cell Biol.* 148, 635–652

20 Cronshaw, J.M. *et al.* (2002) Proteomic analysis of the mammalian nuclear pore complex. *J. Cell Biol.* 158, 915–927

21 DeGrasse, J.A. *et al.* (2009) Evidence for a Shared Nuclear Pore Complex Architecture That Is Conserved from the Last Common Eukaryotic Ancestor. *Mol. Cell. Proteomics* 8, 2119–2130

22 Neumann, N. *et al.* (2010) Comparative Genomic Evidence for a Complete Nuclear Pore Complex in the Last Eukaryotic Common Ancestor. *PLoS One* 5, e13241

23 von Appen, A. *et al.* (2015) In situ structural analysis of the human nuclear pore complex. *Nature* 526, 140–143

24 Devos, D. *et al.* (2004) Components of Coated Vesicles and Nuclear Pore Complexes Share a Common Molecular Architecture. *PLoS Biol.* 2, e380

25 Beck, M. *et al.* (2018) From the resolution revolution to evolution: structural insights into the evolutionary relationships between vesicle coats and the nuclear pore. *Curr. Opin. Struct. Biol.* 52, 32–40

26 Madrid, A.S. *et al.* (2006) The role of the integral membrane nucleoporins Ndc1p and Pom152p in nuclear pore complex assembly and function. *J. Cell Biol.* 173, 361–371

27 Rothballer, A. and Kutay, U. (2013) Poring over pores: nuclear pore complex insertion into the nuclear envelope. *Trends Biochem. Sci.* 38, 292–301

28 Vollmer, B. *et al.* (2012) Dimerization and direct membrane interaction of Nup53 contribute to nuclear pore complex assembly. *EMBO J.* 31, 4072–4084

29 Drin, G. *et al.* (2007) A general amphipathic α-helical motif for sensing membrane curvature. *Nat. Struct. Mol. Biol.* 14, 138–146

30 Marelli, M. *et al.* (2001) A link between the synthesis of nucleoporins and the biogenesis of the nuclear envelope. *J. Cell Biol.* 153, 709–723

31 Liu, H.-L. *et al.* (2009) The Three Fungal Transmembrane Nuclear Pore Complex Proteins of Aspergillus nidulans Are Dispensable in the Presence of an Intact An-Nup84-120 Complex. *Mol. Biol. Cell* 20, 616–630

32 Fischer, J. *et al.* (2015) Linker Nups connect the nuclear pore complex inner ring with the outer ring and transport channel. *Nat. Publ. Gr.* 22, 774–781

33 Amlacher, S. *et al.* (2011) Insight into Structure and Assembly of the Nuclear Pore Complex by Utilizing the Genome of a Eukaryotic Thermophile. *Cell* 146, 277–289

34 Teimer, R. *et al.* (2017) A short linear motif in scaffold Nup145C connects Y-complex with pre-Assembled outer ring Nup82 complex. *Nat. Commun.* 8,

35 Lin, D.H. *et al.* (2016) Architecture of the symmetric core of the nuclear pore. *Science (80-.).* 352, aaf1015–aaf1015

36 Laurell, E. *et al.* (2011) Phosphorylation of Nup98 by Multiple Kinases Is Crucial for NPC Disassembly during Mitotic Entry. *Cell* 144, 539–550

37 Mosalaganti, S. *et al.* (2018) In situ architecture of the algal nuclear pore complex. *Nat. Commun.* 9,

38 Mahamid, J. *et al.* (2016) Visualizing the molecular sociology at the HeLa cell nuclear periphery. *Science (80-.).* 351,

39 Onischenko, E. *et al.* (2017) Natively Unfolded FG Repeats Stabilize the Structure of the Nuclear

Pore Complex. *Cell* 0,

40 Davis, L.I. and Fink, G.R. (1990) The NUP1 gene encodes an essential component of the yeast nuclear pore complex. *Cell* 61, 965–978

41 Starr, C.M. *et al.* (1990) Primary sequence and heterologous expression of nuclear pore glycoprotein p62. *J. Cell Biol.* 110, 1861–1871

42 Hurt, E.C. (1988) A novel nucleoskeletal-like protein located at the nuclear periphery is required for the life cycle of Saccharomyces cerevisiae. *EMBO J.* 7, 4323–4334

43 Finlay, D.R. *et al.* (1987) Inhibition of in vitro nuclear transport by a lectin that binds to nuclear pores. *J. Cell Biol.* 104, 189–200

44 Finlay, D.R. and Forbes, D.J. (1990) Reconstitution of biochemically altered nuclear pores: Transport can be eliminated and restored. *Cell* 60, 17–29

45 Denning, D.P. *et al.* (2003) Disorder in the nuclear pore complex: The FG repeat regions of nucleoporins are natively unfolded. *Proc. Natl. Acad. Sci.* 100, 2450–2455

46 Kim, S.J. *et al.* (2018) Integrative structure and functional anatomy of a nuclear pore complex. *Nature* 555, 475–482

47 Lin, D.H. and Hoelz, A. (2019) The Structure of the Nuclear Pore Complex (An Update). *Annu. Rev. Biochem.* 88, 725–783

48 Schmidt, H.B. and Görlich, D. (2016) Transport Selectivity of Nuclear Pores, Phase Separation, and Membraneless Organelles. *Trends Biochem. Sci.* DOI: 10.1016/j.tibs.2015.11.001

49 Melčák, I. *et al.* (2007) Structure of Nup58/45 suggests flexible nuclear pore diameter by intermolecular sliding. *Science (80-.).* 315, 1729–1732

50 Lim, R.Y.H. *et al.* (2007) Nanomechanical Basis of Selective Gating by the Nuclear Pore Complex. *Science (80-.).* 318, 640–643

51 Rout, M.P. *et al.* (2003) Virtual gating and nuclear transport: The hole picture. *Trends Cell Biol.* 13, 622–628

52 Kapinos, L.E. *et al.* (2014) Karyopherin-centric control of nuclear pores based on molecular occupancy and kinetic analysis of multivalent binding with FG nucleoporins. *Biophys. J.* 106, 1751–1762

53 Yamada, J. *et al.* (2010) A Bimodal Distribution of Two Distinct Categories of Intrinsically Disordered Structures with Separate Functions in FG Nucleoporins. *Mol. Cell. Proteomics* 9, 2205–2224

54 Ribbeck, K. and Görlich, D. (2001) Kinetic analysis of translocation through nuclear pore complexes. *EMBO J.* 20, 1320–1330

55 Schmidt, H.B. and Görlich, D. (2015) Nup98 FG domains from diverse species spontaneously phase-separate into particles with nuclear pore-like permselectivity. *Elife* 4,

56 Shin, Y. and Brangwynne, C.P. (2017) Liquid phase condensation in cell physiology and disease. *Science (80-.).* 357, eaaf4382

57 Semenov, A.N. and Rubinstein, M. (1998) Thermoreversible Gelation in Solutions of Associative Polymers. 1. Statics. *Macromolecules* 31, 1373–1385

58 Banani, S.F. *et al.* (2016) Compositional Control of Phase-Separated Cellular Bodies. *Cell* 166, 651–663

59 Ader, C. *et al.* (2010) Amyloid-like interactions within nucleoporin FG hydrogels. *Proc. Natl. Acad. Sci.* 107, 6281–6285

60 Milles, S. *et al.* (2013) Facilitated aggregation of FG nucleoporins under molecular crowding conditions. *EMBO Rep.* 14, 178–183

61 Frey, S. *et al.* (2006) FG-rich repeats of nuclear pore proteins form a three-dimensional meshwork with hydrogel-like properties. *Science* 314, 815–7

62 Frey, S. and Görlich, D. (2009) FG/FxFG as well as GLFG repeats form a selective permeability barrier with self-healing properties. *EMBO J.* 28, 2554–2567

63 Frey, S. and Görlich, D. (2007) A Saturated FG-Repeat Hydrogel Can Reproduce the Permeability Properties of Nuclear Pore Complexes. *Cell* 130, 512–523

64 Tanaka, F. (2011) *Polymer Physics Applications to Molecular Association and Thermoreversible Gelation-Polymer Physics: Applications to Molecular Association and Thermoreversible Gelation Fumihiko Tanaka Frontmatter More information*,

65 Celetti, G. *et al.* (2020) The liquid state of FG-nucleoporins mimics permeability barrier properties of nuclear pore complexes. *J. Cell Biol.* 219, jcb.201907157

66 Frey, S. *et al.* (2018) Surface Properties Determining Passage Rates of Proteins through Nuclear Pores. *Cell* 174, 202-217.e9

67 Hülsmann, B.B. *et al.* (2012) The Permeability of Reconstituted Nuclear Pores Provides Direct Evidence for the Selective Phase Model. *Cell* 150, 738–751

68 Ribbeck, K. and Görlich, D. (2002) The permeability barrier of nuclear pore complexes appears to operate via hydrophobic exclusion. *EMBO J.* 21, 2664–71

69 Patel, S.S. *et al.* (2007) Natively Unfolded Nucleoporins Gate Protein Diffusion across the Nuclear Pore Complex. *Cell* 129, 83–96

70 Uversky, V.N. *et al.* (2000) Why are "natively unfolded" proteins unstructured under physiologic conditions? *Proteins Struct. Funct. Genet.* 41, 415–427

71 Voronina, E. and Seydoux, G. (2010) The C. elegans homolog of nucleoporin Nup98 is required for the integrity and function of germline P granules. *Development* 137, 1441–1450

72 Zhang, K. *et al.* (2018) Stress Granule Assembly Disrupts Nucleocytoplasmic Transport. *Cell* 173, 958-971.e17

73 Chopra, K. *et al.* (2019) Evolutionary divergence of the nuclear pore complex from fungi to metazoans. *Protein Sci.* 28, 571–586

74 Shen, Q. *et al.* (2019) RanBP2/Nup358 enhances RNAi activity by sumoylating and stabilizing Argonaute 1. *bioRxiv* DOI: 10.1101/555896

75 Sahoo, M.R. *et al.* (2017) Nup358 binds to AGO proteins through its SUMO -interacting motifs and promotes the association of target mRNA with miRISC . *EMBO Rep.* 18, 241–263

76 Mahadevan, K. *et al.* (2013) RanBP2/Nup358 Potentiates the Translation of a Subset of mRNAs Encoding Secretory Proteins. *PLoS Biol.* 11, e1001545

77 Murawala, P. *et al.* (2009) Nup358 interacts with APC and plays a role in cell polarization. *J. Cell Sci.* 122, 3113–3122

78 Magre, I. *et al.* (2019) Nup358 regulates microridge length by controlling SUMOylation-dependent activity of aPKC in zebrafish epidermis. *J. Cell Sci.* 132, jcs224501

79 Sakin, V. *et al.* (2015) Sumoylation of the GTPase Ran by the RanBP2 SUMO E3 Ligase Complex. *J. Biol. Chem.* 290, 23589–23602

80 Bichel, K. *et al.* (2013) HIV-1 capsid undergoes coupled binding and isomerization by the nuclear pore protein NUP358. *Retrovirology* 10,

81 Strunze, S. *et al.* (2011) Kinesin-1-Mediated Capsid Disassembly and Disruption of the Nuclear Pore Complex Promote Virus Infection. *Cell Host Microbe* 10, 210–223

82 Khalaf, B. *et al.* (2019) Ankyrin-G induces nucleoporin RanBP2/Nup358 to associate with the axon initial segment of neurons. *J. Cell Sci.* DOI: 10.1242/jcs.222802

83 Salina, D. *et al.* (2003) Nup358 integrates nuclear envelope breakdown with kinetochore assembly. *J. Cell Biol.* 162, 991–1001

84 Hampoelz, B. *et al.* (2016) Pre-assembled Nuclear Pores Insert into the Nuclear Envelope during Early Development. *Cell* 166, 664–678

85 Bernad, R. *et al.* (2004) Nup358/RanBP2 Attaches to the Nuclear Pore Complex via Association with Nup88 and Nup214/CAN and Plays a Supporting Role in CRM1-Mediated Nuclear Protein Export. *Mol. Cell. Biol.* 24, 2373–2384

86 Walther, T.C. *et al.* (2002) The cytoplasmic filaments of the nuclear pore complex are dispensable for selective nuclear protein import. *J. Cell Biol.* 158, 63–77

87 Partridge, J.R. and Schwartz, T.U. (2009) Crystallographic and Biochemical Analysis of the Ran-binding Zinc Finger Domain. *J. Mol. Biol.* 391, 375–389

88 Pichler, A. *et al.* (2002) The Nucleoporin RanBP2 Has SUMO1 E3 Ligase Activity. *Cell* 108, 109–120

89 Saitoh, H. *et al.* (1997) RanBP2 associates with Ubc9p and a modified form of RanGAP1. *Proc. Natl. Acad. Sci.* 94, 3736–3741

90 Mahajan, R. *et al.* (1997) A Small Ubiquitin-Related Polypeptide Involved in Targeting RanGAP1 to Nuclear Pore Complex Protein RanBP2. *Cell* 88, 97–107

91 Werner, A. *et al.* (2012) The RanBP2/RanGAP1 *SUMO1/Ubc9 Complex Is a Multisubunit SUMO E3 Ligase. *Mol. Cell* 46, 287–298

92 Matunis, M.J. *et al.* (1998) SUMO-1 Modification and Its Role in Targeting the Ran GTPase-activating Protein, RanGAP1, to the Nuclear Pore Complex. *J. Cell Biol.* 140, 499–509

93 Lin, D.H. *et al.* (2013) Structural and Functional Analysis of the C-Terminal Domain of Nup358/RanBP2. *J. Mol. Biol.* 425, 1318–1329

94 Forler, D. *et al.* (2004) RanBP2/Nup358 Provides a Major Binding Site for NXF1-p15 Dimers at the Nuclear Pore Complex and Functions in Nuclear mRNA Export. *Mol. Cell. Biol.* 24, 1155–1167

95 Singh, B.B. *et al.* (1999) The Zinc Finger Cluster Domain of RanBP2 Is a Specific Docking Site for the Nuclear Export Factor, Exportin-1. *J. Biol. Chem.* 274, 37370–37378

96 Ben-Efraim, I. and Gerace, L. (2001) Gradient of Increasing Affinity of Importin β for Nucleoporins along the Pathway of Nuclear Import. *J. Cell Biol.* 152, 411–418

97 Yi, H. *et al.* (2007) The Cyclophilin-like Domain of Ran-binding Protein-2 Modulates Selectively the Activity of the Ubiquitin-Proteasome System and Protein Biogenesis. *J. Biol. Chem.* 282, 34770–34778

98 Splinter, D. *et al.* (2010) Bicaudal D2, dynein, and kinesin-1 associate with nuclear pore complexes and regulate centrosome and nuclear positioning during mitotic entry. *PLoS Biol.* 8, e1000350

99 Cui, H. *et al.* (2019) Adapter Proteins for Opposing Motors Interact Simultaneously with Nuclear Pore Protein Nup358. *Biochemistry* 58, 5085–5097

100 Cho, K. *et al.* (2007) Association of the Kinesin-Binding Domain of RanBP2 to KIF5B and KIF5C Determines Mitochondria Localization and Function. *Traffic* 8, 1722–1735

101 Hopper, A.K. *et al.* (1990) The yeast RNA1 gene product necessary for RNA processing is located in the cytosol and apparently excluded from the nucleus. *J. Cell Biol.* 111, 309–321

102 Rose, A. and Meier, I. (2001) A domain unique to plant RanGAP is responsible for its targeting to the plant nuclear rim. *Proc. Natl. Acad. Sci.* 98, 15377–15382

103 Cesario, J. and McKim, K.S. (2011) RanGTP is required for meiotic spindle organization and the initiation of embryonic development in Drosophila. *J. Cell Sci.* 124, 3797–810

104 Yang, W. *et al.* (2004) Imaging of single-molecule translocation through nuclear pore complexes. *Proc. Natl. Acad. Sci.* 101, 12887–12892

105 Timney, B.L. *et al.* (2006) Simple kinetic relationships and nonspecific competition govern nuclear import rates in vivo. *J. Cell Biol.* 175, 579–593

106 Naim, B. *et al.* (2009) Cargo surface hydrophobicity is sufficient to overcome the nuclear pore complex selectivity barrier. *EMBO J.* 28, 2697–2705

107 Colwell, L.J. *et al.* (2010) Charge as a selection criterion for translocation through the nuclear pore complex. *PLoS Comput. Biol.* 6,

108 Isgro, T.A. and Schulten, K. (2005) Binding Dynamics of Isolated Nucleoporin Repeat Regions to Importin-β. *Structure* 13, 1869–1879

109 Port, S.A. *et al.* (2015) Structural and Functional Characterization of CRM1-Nup214 Interactions Reveals Multiple FG-Binding Sites Involved in Nuclear Export. *Cell Rep.* 13, 690–702

110 Hayama, R. *et al.* (2018) Thermodynamic characterization of the multivalent interactions underlying rapid and selective translocation through the nuclear pore complex. *J. Biol. Chem.* 293, 4555–4563

111 Moore, M.S. and Blobel, G. (1993) The GTP-binding protein Ran/TC4 is required for protein import into the nucleus. *Nature* 365, 661–663

112 Lee, S.J. *et al.* (2005) Structural basis for nuclear import complex dissociation by RanGTP. *Nature* 435, 693–696

113 Otsuka, S. *et al.* (2008) Individual binding pockets of importin- for FG-nucleoporins have different binding properties and different sensitivities to RanGTP. *Proc. Natl. Acad. Sci.* 105, 16101–16106

114 Melchior, F. *et al.* (1993) Inhibition of nuclear protein import by nonhydrolyzable analogues of GTP and identification of the small GTPase Ran/TC4 as an essential transport factor. *J. Cell Biol.* 123, 1649–1659

115 Rexach, M. and Blobel, G. (1995) Protein import into nuclei: association and dissociation reactions involving transport substrate, transport factors, and nucleoporins. *Cell* 83, 683–692

116 Kutay, U. *et al.* (1997) Export of Importin α from the Nucleus Is Mediated by a Specific Nuclear Transport Factor. *Cell* 90, 1061–1071

117 Ribbeck, K. *et al.* (1998) NTF2 mediates nuclear import of Ran. *EMBO J.* 17, 6587–6598

118 Smith, A. *et al.* (1998) Nuclear import of Ran:GDP is mediated by NTF2. *Curr. Biol.* 8, 1403–1406

119 Paraskeva, E. *et al.* (1999) CRM1-mediated Recycling of Snurportin 1 to the Cytoplasm. *J. Cell Biol.* 145, 255–264

120 Dong, X. *et al.* (2009) Structural basis for assembly and disassembly of the CRM1 nuclear export complex. *Nat. Struct. Mol. Biol.* 16, 558–560

121 Clouse, K.N. *et al.* (2001) A Ran-independent pathway for export of spliced mRNA. *Nat. Cell Biol.* 3, 97–99

122 Katahira, J. *et al.* (1999) The Mex67p-mediated nuclear mRNA export pathway is conserved from yeast to human. *EMBO J.* 18, 2593–2609

123 Mackmull, M. *et al.* (2017) Landscape of nuclear transport receptor cargo specificity. *Mol. Syst. Biol.* 13, 962

124 Miyamoto, Y. *et al.* (2016) Importin α: a key molecule in nuclear transport and non-transport functions. *J. Biochem.* 160, 69–75

125 Conti, E. and Izaurralde, E. Nucleocytoplasmic transport enters the atomic age. , *Current Opinion in Cell Biology*, 13. 01-Jun-(2001) , Elsevier Ltd, 310–319

126 Wente, S.R. and Rout, M.P. (2010) The Nuclear Pore Complex and Nuclear Transport. *Cold Spring Harb. Perspect. Biol.* 2, a000562–a000562

127 Andersen, K.R. *et al.* (2013) Scaffold nucleoporins Nup188 and Nup192 share structural and functional properties with nuclear transport receptors. *Elife* 2,

128 Yoshida, K. and Blobel, G. (2001) The Karyopherin Kap142p/Msn5p Mediates Nuclear Import and Nuclear Export of Different Cargo Proteins. *J. Cell Biol.* 152, 729–740

129 Ganguly, A. *et al.* (2018) Importin-β Directly Regulates the Motor Activity and Turnover of a Kinesin-4. *Dev. Cell* 0, 642-651.e5

130 Roth, D.M. *et al.* (2011) Mechanism of Microtubule-facilitated “Fast Track” Nuclear Import. *J. Biol. Chem.* 286, 14335–14351

131 Campbell, E.M. and Hope, T.J. Role of the cytoskeleton in nuclear import. , *Advanced Drug Delivery Reviews*, 55. 16-Jun-(2003) , Elsevier, 761–771

132 Roth, D.M. *et al.* (2007) A Microtubule-Facilitated Nuclear Import Pathway for Cancer Regulatory Proteins. *Traffic* 8, 673–686

133 Yudin, D. *et al.* (2008) Localized regulation of axonal RanGTPase controls retrograde injury signaling in peripheral nerve. *Neuron* 59, 241–52

134 Hanz, S. *et al.* (2003) Axoplasmic Importins Enable Retrograde Injury Signaling in Lesioned Nerve. *Neuron* 40, 1095–1104

135 Jäkel, S. *et al.* (2002) Importins fulfil a dual function as nuclear import receptors and cytoplasmic chaperones for exposed basic domains. *EMBO J.* 21, 377–386

136 Harel, A. and Forbes, D.J. Importin beta: Conducting a much larger cellular symphony. , *Molecular Cell*, 16. (2004) , 319–330

137 Walther, T.C. *et al.* (2003) RanGTP mediates nuclear pore complex assembly. *Nature* 424, 689–694

138 Guo, L. *et al.* (2018) Nuclear-Import Receptors Reverse Aberrant Phase Transitions of RNA-Binding Proteins with Prion-like Domains. *Cell* 173, 677-692.e20

139 Yoshizawa, T. *et al.* (2018) Nuclear Import Receptor Inhibits Phase Separation of FUS through Binding to Multiple Sites. *Cell* 173, 693-705.e22

140 Qamar, S. *et al.* (2018) FUS Phase Separation Is Modulated by a Molecular Chaperone and Methylation of Arginine Cation-π Interactions. *Cell* 173, 720-734.e15

141 Rousseau, A. and Bertolotti, A. (2018) Regulation of proteasome assembly and activity in health and disease. *Nat. Rev. Mol. Cell Biol.* 19, 697–712

142 Bard, J.A.M. *et al.* (2018) Structure and Function of the 26S Proteasome. *Annu. Rev. Biochem.* 87, 697–724

143 Doucet, C.M. *et al.* (2010) Cell Cycle-Dependent Differences in Nuclear Pore Complex Assembly in Metazoa. *Cell* 141, 1030–1041

144 Ungricht, R. and Kutay, U. (2017) Mechanisms and functions of nuclear envelope remodelling. *Nat. Rev. Mol. Cell Biol.* 18, 229–245

145 Linder, M.I. *et al.* (2017) Mitotic Disassembly of Nuclear Pore Complexes Involves CDK1- and PLK1-Mediated Phosphorylation of Key Interconnecting Nucleoporins. *Dev. Cell* 43, 141-156.e7

146 Dultz, E. *et al.* (2008) Systematic kinetic analysis of mitotic dis- and reassembly of the nuclear pore in living cells. *J. Cell Biol.* 180, 857–865

147 Martino, L. *et al.* (2017) Channel Nucleoporins Recruit PLK-1 to Nuclear Pore Complexes to Direct Nuclear Envelope Breakdown in C. elegans. *Dev. Cell* 43, 157-171.e7

148 Forbes, D.J. *et al.* (2015) Nuclear transport factors: global regulation of mitosis. *Curr. Opin. Cell Biol.* 35, 78–90

149 Hampoelz, B. *et al.* (2019) Structure and Assembly of the Nuclear Pore Complex. *Annu. Rev. Biophys.* 48, 515–536

150 Onischenko, E.A. *et al.* (2005) Cdk1 and okadaic acid-sensitive phosphatases control assembly of nuclear pore complexes in Drosophila embryos. *Mol. Biol. Cell* 16, 5152–62

151 Hattersley, N. *et al.* (2016) A Nucleoporin Docks Protein Phosphatase 1 to Direct Meiotic Chromosome Segregation and Nuclear Assembly. *Dev. Cell* 38, 463–477

152 Schellhaus, A.K. *et al.* (2016) Nuclear Reformation at the End of Mitosis. *J. Mol. Biol.* 428, 1962–1985

153 Perry, R.B.T. and Fainzilber, M. Nuclear transport factors in neuronal function. , *Seminars in Cell and Developmental Biology*, 20. 01-Jul-(2009) , Academic Press, 600–606

154 Lau, C.K. *et al.* (2009) Transportin Regulates Major Mitotic Assembly Events: From Spindle to Nuclear Pore Assembly. *Mol. Biol. Cell* 20, 4043–4058

155 Zierhut, C. *et al.* (2014) Nucleosomal regulation of chromatin composition and nuclear assembly revealed by histone depletion. *Nat. Struct. Mol. Biol.* 21, 617–625

156 Franz, C. *et al.* (2007) MEL-28/ELYS is required for the recruitment of nucleoporins to chromatin and postmitotic nuclear pore complex assembly. *EMBO Rep.* 8, 165–72

157 Rasala, B.A. *et al.* (2008) Capture of AT-rich Chromatin by ELYS Recruits POM121 and NDC1 to Initiate Nuclear Pore Assembly. *Mol. Biol. Cell* 19, 3982–3996

158 Mansfeld, J. *et al.* (2006) The Conserved Transmembrane Nucleoporin NDC1 Is Required for

Nuclear Pore Complex Assembly in Vertebrate Cells. *Mol. Cell* 22, 93–103

159 Eisenhardt, N. *et al.* (2014) Interaction of Nup53 with Ndc1 and Nup155 is required for nuclear pore complex assembly. *J. Cell Sci.* 127, 908–921

160 Mitchell, J.M. *et al.* (2010) Pom121 links two essential subcomplexes of the nuclear pore complex core to the membrane. *J. Cell Biol.* 191, 505–521

161 Hawryluk-Gara, L.A. *et al.* (2005) Vertebrate Nup53 interacts with the nuclear lamina and is required for the assembly of a Nup93-containing complex. *Mol. Biol. Cell* 16, 2382–94

162 Sachdev, R. *et al.* (2012) The C-terminal domain of Nup93 is essential for assembly of the structural backbone of nuclear pore complexes. *Mol. Biol. Cell* 23, 740–749

163 Dultz, E. *et al.* (2009) Formation of the nuclear envelope permeability barrier studied by sequential photoswitching and flux analysis. *Biophys. J.* 97, 1891–1897

164 Schooley, A. *et al.* Building a nuclear envelope at the end of mitosis: Coordinating membrane reorganization, nuclear pore complex assembly, and chromatin de-condensation. , *Chromosoma*, 121. Dec-(2012) , 539–554

165 Otsuka, S. *et al.* (2018) Postmitotic nuclear pore assembly proceeds by radial dilation of small membrane openings. *Nat. Struct. Mol. Biol.* 25, 21–28

166 Belgareh, N. *et al.* (2001) An evolutionarily conserved NPC subcomplex, which redistributes in part to kinetochores in mammalian cells. *J. Cell Biol.* 154, 1147–1160

167 D'Angelo, M. a *et al.* (2006) Nuclear pores form de novo from both sides of the nuclear envelope. *Science (80-.).* 312, 440–443

168 McCloskey, A. *et al.* (2018) Tpr regulates the total number of nuclear pore complexes per cell nucleus. *Genes Dev.* 32, 1321–1331

169 Walther, T.C. *et al.* (2001) The nucleoporin Nup153 is required for nuclear pore basket formation, nuclear pore complex anchoring and import of a subset of nuclear proteins. *EMBO J.* 20, 5703–5714

170 Vollmer, B. *et al.* (2015) Nup153 Recruits the Nup107-160 Complex to the Inner Nuclear Membrane for Interphasic Nuclear Pore Complex Assembly. *Dev. Cell* 33, 717–728

171 Otsuka, S. and Ellenberg, J. (2018) Mechanisms of nuclear pore complex assembly – two different ways of building one molecular machine. *FEBS Lett.* 592, 475–488

172 Funakoshi, T. *et al.* (2011) Localization of Pom121 to the inner nuclear membrane is required for an early step of interphase nuclear pore complex assembly. *Mol. Biol. Cell* 22, 1058–1069

173 Dultz, E. and Ellenberg, J. (2010) Live imaging of single nuclear pores reveals unique assembly kinetics and mechanism in interphase. *J. Cell Biol.* 191, 15–22

174 Thaller, D.J. and Patrick Lusk, C. (2018) Fantastic nuclear envelope herniations and where to find them. *Biochem. Soc. Trans.* 46, 877–889

175 Otsuka, S. *et al.* (2016) Nuclear pore assembly proceeds by an inside-out extrusion of the nuclear envelope. *Elife* 5, 76

176 Talamas, J.A. and Hetzer, M.W. (2011) POM121 and Sun1 play a role in early steps of interphase NPC assembly. *J. Cell Biol.* 194, 27–37

177 Kessel, R.G. (1992) Annulate Lamellae: A Last Frontier in Cellular Organelles. *Int. Rev. Cytol.* 133, 43–120

178 Stafstrom, J.P. and Staehelin, L.A. (1984) Are annulate lamellae in the Drosophila embryo the result of overproduction of nuclear pore components? *J. Cell Biol.* 98, 699–708

179 Spindler, M. and Hemleben, C. (1982) Formation and possible function of annulate lamellae in a planktic foraminifer. *J. Ultrastruct. Res.* 81, 341–350

180 Sutovsky, P. *et al.* (1998) Assembly of nuclear pore complexes and annulate lamellae promotes normal pronuclear development in fertilized mammalian oocytes. *J. Cell Sci.* 111, 2841–54

181 Kessel, R.G. and Beams, H.W. (1969) ANNULATE LAMELLAE AND "YOLK NUCLEI" IN OOCYTES OF THE DRAGONFLY, LIBELLULA PULCHELLA. *J. Cell Biol.* 42, 185–201

182 Krishan, A. *et al.* (1968) Hypertrophy of granular endoplasmic reticulum and annulate lamellae in Earle's L cells exposed to vinblastine sulfate. *J. Cell Biol.* 39, 211–216

183 Kessel, R.G. The annulate lamellae-From obscurity to spotlight. , *Electron Microscopy Reviews*, 2. (1989) , 257–348

184 Onischenko, E.A. *et al.* (2004) Annulate lamellae play only a minor role in the storage of excess nucleoporins in Drosophila embryos. *Traffic* 5, 152–164

185 Ren, H. *et al.* (2019) Postmitotic annulate lamellae assembly contributes to nuclear envelope reconstitution in daughter cells. *J. Biol. Chem.* 294, 10383–10391

186 Dabauvalle, M.C. *et al.* (1991) Spontaneous assembly of pore complex-containing membranes ("annulate lamellae") in Xenopus egg extract in the absence of chromatin. *J. Cell Biol.* 112, 1073–1082

187 Ewald, A. *et al.* (1997) Preassembly of annulate lamellae in egg extracts inhibits nuclear pore complex formation, but not nuclear membrane assembly. *Eur. J. Cell Biol.* 73, 259–69

188 Kessel, R.G. (1963) ELECTRON MICROSCOPE STUDIES ON THE ORIGIN OF ANNULATE LAMELLAE IN OOCYTES OF NECTURUS. *J. Cell Biol.* 19, 391–414

189 Baca, M. and Zamboni, L. (1967) The fine structure of human follicular oocytes. *J. Ultrastruct. Res.* 19, 354–381

190 Scheer, U. and Franke, W.W. (1972) Annulate lamellae in plant cells: Formation during microsporogenesis and pollen development in Canna generalis Bailey. *Planta* 107, 145–159

191 Kessel, R.G. (1981) Origin, differentiation, distribution and possible functional role of annulate lamellae during spermatogenesis in Drosophila melanogaster. *J. Ultrasructure Res.* 75, 72–96

192 Brangwynne, C.P. *et al.* (2009) Germline P Granules Are Liquid Droplets That Localize by Controlled Dissolution/Condensation. *Science (80-.).* 324, 1729–1732

193 Pitt, J.N. *et al.* (2000) P granules in the germ cells of Caenorhabditis elegans adults are associated with clusters of nuclear pores and contain RNA. *Dev. Biol.* 219, 315–33

194 Sheth, U. *et al.* (2010) Perinuclear P granules are the principal sites of mRNA export in adult C. elegans germ cells. *Development* 137, 1305–1314

195 Owji, H. *et al.* (2018) A comprehensive review of signal peptides: Structure, roles, and applications. *Eur. J. Cell Biol.* 97, 422–441

196 Lécuyer, E. *et al.* (2007) Global Analysis of mRNA Localization Reveals a Prominent Role in Organizing Cellular Architecture and Function. *Cell* 131, 174–187

197 Wilk, R. *et al.* (2016) Diverse and pervasive subcellular distributions for both coding and long noncoding RNAs. *Genes Dev.* 30, 594–609

198 Jambor, H. *et al.* (2015) Systematic imaging reveals features and changing localization of mRNAs in Drosophila development. *Elife* 2015, 1–22

199 Carlevaro-Fita, J. and Johnson, R. (2019) Global Positioning System: Understanding Long Noncoding RNAs through Subcellular Localization. *Mol. Cell* 73, 869–883

200 Wang, B. and Bao, L. (2017) Axonal microRNAs: localization, function and regulatory mechanism during axon development. *J. Mol. Cell Biol.* 9, 82–90

201 Lawrence, J.B. and Singer, R.H. (1986) Intracellular localization of messenger RNAs for cytoskeletal proteins. *Cell* 45, 407–15

202 Jeffery, W.R. and Wilson, L.J. (1983) Localization of messenger RNA in the cortex of Chaetopterus eggs and early embryos. *Development* 75,

203 Chin, A. and Lécuyer, E. (2017) RNA localization: Making its way to the center stage. *Biochim. Biophys. Acta - Gen. Subj.* 1861, 2956–2970

204 Bovaird, S. *et al.* (2018) Biological functions, regulatory mechanisms, and disease relevance of RNA localization pathways. *FEBS Lett.* 592, 2948–2972

205 Lahtvee, P.-J. *et al.* (2017) Absolute Quantification of Protein and mRNA Abundances Demonstrate Variability in Gene-Specific Translation Efficiency in Yeast. *Cell Syst.* 4, 495-504.e5

206 Shieh, Y.-W. *et al.* (2015) Operon structure and cotranslational subunit association direct protein assembly in bacteria. *Science (80-.).* 350, 678–680

207 Wells, J.N. *et al.* (2016) Operon Gene Order Is Optimized for Ordered Protein Complex Assembly. *Cell Rep.* 14, 679–685

208 Keene, J.D. (2007) RNA regulons: coordination of post-transcriptional events. *Nat. Rev. Genet.* 8, 533–543

209 Prasad, A. *et al.* (2016) The PUF binding landscape in metazoan germ cells. *RNA* 22, 1–18

210 Saint-Georges, Y. *et al.* (2008) Yeast mitochondrial biogenesis: A role for the PUF RNA-binding protein puf3p in mRNA localization. *PLoS One* 3,

211 Tsuruyama, T. (2018) Non-Linear Kinetic Analysis of Protein Assembly Based on Center Manifold Theory. In *Kinetic Theory* InTech

212 Weatheritt, R.J. *et al.* (2014) Asymmetric mRNA localization contributes to fidelity and sensitivity of spatially localized systems. *Nat. Struct. Mol. Biol.* 21, 833–839

213 Biedermann, B. *et al.* (2009) Translational Repression of Cyclin E Prevents Precocious Mitosis and Embryonic Gene Activation during C. elegans Meiosis. *Dev. Cell* 17, 355–364

214 Ephrussi, A. and Lehmann, R. (1992) Induction of germ cell formation by oskar. *Nature* 358, 387–392

215 Hachet, O. and Ephrussi, A. (2004) Splicing of oskar RNA in the nucleus is coupled to its cytoplasmic localization. *Nature* 428, 959–963

216 Kress, T.L. *et al.* (2004) Nuclear RNP complex assembly initiates cytoplasmic RNA localization. *J. Cell Biol.* 165, 203–211

217 Viphakone, N. *et al.* (2019) Co-transcriptional Loading of RNA Export Factors Shapes the Human Transcriptome. *Mol. Cell* 75, 310-323.e8

218 Grünwald, D. *et al.* (2011) Nuclear export dynamics of RNA–protein complexes. *Nature* 475, 333–341

219 Daneholt, B. (2001) Assembly and transport of a premessenger RNP particle. *Proc. Natl. Acad. Sci.* 98, 7012–7017

220 Gaspar, I. *et al.* (2017) Enzymatic production of single-molecule FISH and RNA capture probes. *RNA* 23, 1582–1591

221 Tran, E.J. *et al.* (2007) The DEAD-Box Protein Dbp5 Controls mRNA Export by Triggering Specific RNA:Protein Remodeling Events. *Mol. Cell* 28, 850–859

222 Soheilypour, M. and Mofrad, M.R.K. (2018) Quality control of mRNAs at the entry of the nuclear pore: Cooperation in a complex molecular system. *Nucleus* 9, 202–211

223 Jansen, R.-P. (2001) mRNA localization: message on the move. *Nat. Rev. Mol. Cell Biol.* 2, 247–256

224 Mofatteh, M. and Bullock, S.L. (2017) SnapShot: Subcellular mRNA Localization. *Cell* 169, 178-178.e1

225 Long, R.M. *et al.* (1997) Mating type switching in yeast controlled by asymmetric localization of ASH1 mRNA. *Science (80-.).* 277, 383–387

226 Takizawa, P.A. *et al.* (1997) Actin-dependent localization of an RNA encoding a cell-fate determinant in yeast. *Nature* 389, 90–93

227 Tiruchinapalli, D.M. *et al.* (2003) Activity-Dependent Trafficking and Dynamic Localization of Zipcode Binding Protein 1 and β-Actin mRNA in Dendrites and Spines of Hippocampal Neurons. *J. Neurosci.* 23, 3251–3261

228 Rebagliati, M.R. *et al.* (1985) Identification and cloning of localized maternal RNAs from xenopus eggs. *Cell* 42, 769–777

229 Ephrussi, A. *et al.* (1991) oskar organizes the germ plasm and directs localization of the posterior determinant nanos. *Cell* 66, 37–50

230 Clark, A. *et al.* (2007) A Dynein-dependent shortcut rapidly delivers axis determination transcripts into the Drosophila oocyte. *Development* 134, 1955–1965

231 Jambor, H. *et al.* (2014) A stem-loop structure directs oskar mRNA to microtubule minus ends. *RNA* 20, 429–439

232 Palacios, I.M. and St Johnston, D. (2002) Kinesin light chain-independent function of the Kinesin heavy chain in cytoplasmic streaming and posterior localisation in the Drosophila oocyte. *Development* 129, 5473–5485

233 Duncan, J.E. and Warrior, R. (2002) The Cytoplasmic Dynein and Kinesin Motors Have Interdependent Roles in Patterning the Drosophila Oocyte. *Curr. Biol.* 12, 1982–1991

234 Brendza, R.P. *et al.* (2002) Posterior Localization of Dynein and Dorsal-Ventral Axis Formation Depend on Kinesin in Drosophila Oocytes. *Curr. Biol.* 12, 1541–1545

235 Gáspár, I. *et al.* (2017) An RNA -binding atypical tropomyosin recruits kinesin-1 dynamically to oskar mRNP s. *EMBO J.* 36, 319–333

236 Zimyanin, V.L. *et al.* (2008) In Vivo Imaging of oskar mRNA Transport Reveals the Mechanism of Posterior Localization. *Cell* 134, 843–853

237 Parton, R.M. *et al.* (2011) A PAR-1–dependent orientation gradient of dynamic microtubules directs posterior cargo transport in the Drosophila oocyte. *J. Cell Biol.* 194, 121–135

238 Vijayakumar, J. *et al.* (2019) The prion-like domain of Drosophila Imp promotes axonal

transport of RNP granules in vivo. *Nat. Commun.* 10, 2593

239 Leung, K.-M. *et al.* (2018) Cue-Polarized Transport of β-actin mRNA Depends on 3'UTR and Microtubules in Live Growth Cones. *Front. Cell. Neurosci.* 12,

240 Castagnetti, S. *et al.* (2000) Control of oskar mRNA translation by Bruno in a novel cell-free system from Drosophila ovaries. *Development* 127, 1063–1068

241 Besse, F. *et al.* (2009) Drosophila PTB promotes formation of high-order RNP particles and represses oskar translation. *Genes Dev.* 23, 195–207

242 Besse, F. and Ephrussi, A. (2008) Translational control of localized mRNAs: restricting protein synthesis in space and time. *Nat. Rev. Mol. Cell Biol.* 9, 971–980

243 Babu, K. *et al.* (2004) Roles of Bifocal, Homer, and F-actin in anchoring Oskar to the posterior cortex of Drosophila oocytes. *Genes Dev.* 18, 138–143

244 Vanzo, N. *et al.* (2007) Stimulation of Endocytosis and Actin Dynamics by Oskar Polarizes the Drosophila Oocyte. *Dev. Cell* 12, 543–555

245 Sinsimer, K.S. *et al.* (2013) Germ Plasm Anchoring Is a Dynamic State that Requires Persistent Trafficking. *Cell Rep.* 5, 1169–1177

246 Zappulo, A. *et al.* (2017) RNA localization is a key determinant of neurite-enriched proteome. *Nat. Commun.* 8, 583

247 Béthune, J. *et al.* (2019) Membrane-Associated RNA-Binding Proteins Orchestrate Organelle-Coupled Translation. *Trends Cell Biol.* 29, 178–188

248 Baumann, S. *et al.* (2012) Kinesin-3 and dynein mediate microtubule-dependent co-transport of mRNPs and endosomes. *J. Cell Sci.* 125, 2740–2752

249 Todd, A.G. *et al.* (2013) COPI transport complexes bind to specific RNAs in neuronal cells. *Hum. Mol. Genet.* 22, 729–736

250 Zabezhinsky, D. *et al.* (2016) An Essential Role for COPI in mRNA Localization to Mitochondria and Mitochondrial Function. *Cell Rep.* 15, 540–549

251 Schmid, M. *et al.* (2006) Coordination of Endoplasmic Reticulum and mRNA Localization to the Yeast Bud. *Curr. Biol.* 16, 1538–1543

252 Liao, Y.-C. *et al.* (2019) RNA Granules Hitchhike on Lysosomes for Long-Distance Transport, Using Annexin A11 as a Molecular Tether. *Cell* 179, 147-164.e20

253 Cioni, J.-M.M. *et al.* (2019) Late Endosomes Act as mRNA Translation Platforms and Sustain Mitochondria in Axons. *Cell* 176, 56-72.e15

254 Salogiannis, J. and Reck-Peterson, S.L. Hitchhiking: A Non-Canonical Mode of Microtubule-Based Transport. , *Trends in Cell Biology*, 27. 01-Feb-(2017) , Elsevier Ltd, 141–150

255 Cohen, R.S. (2005) The role of membranes and membrane trafficking in RNA localization. *Biol. Cell* 97, 5–18

256 Knowles, R.B. *et al.* (1996) Translocation of RNA granules in living neurons. *J. Neurosci.* 16, 7812–7820

257 Bauer, K.E. *et al.* (2019) Live cell imaging reveals 3'-UTR dependent mRNA sorting to synapses. *Nat. Commun.* 10,

258 Turner-Bridger, B. *et al.* (2018) Single-molecule analysis of endogenous β-actin mRNA trafficking reveals a mechanism for compartmentalized mRNA localization in axons. *Proc. Natl.*

Acad. Sci. U. S. A. 115, E9697–E9706

259 Fu, M. and Holzbaur, E.L.F. (2014) Integrated regulation of motor-driven organelle transport by scaffolding proteins. *Trends Cell Biol.* 24, 564–574

260 König, J. *et al.* (2009) The fungal RNA-binding protein Rrm4 mediates long-distance transport of ubi1 and rho3 mRNAs. *EMBO J.* 28, 1855–1866

261 Pohlmann, T. *et al.* (2015) A FYVE zinc finger domain protein specifically links mRNA transport to endosome trafficking. *Elife* 4,

262 Gerber, A.P. *et al.* (2004) Extensive association of functionally and cytotopically related mRNAs with Puf family RNA-binding proteins in yeast. *PLoS Biol.* 2, e79

263 Olgeiser, L. *et al.* (2019) The key protein of endosomal mRNP transport Rrm4 binds translational landmark sites of cargo mRNAs. *EMBO Rep.* 20,

264 Konopacki, F.A. *et al.* (2016) ESCRT-II controls retinal axon growth by regulating DCC receptor levels and local protein synthesis. *Open Biol.* 6, 150218

265 Higuchi, Y. *et al.* (2014) Early endosome motility spatially organizes polysome distribution. *J. Cell Biol.* 204, 343–357

266 Zander, S. *et al.* (2016) Endosomal assembly and transport of heteromeric septin complexes promote septin cytoskeleton formation. *J. Cell Sci.* 129, 2778–2792

267 Schwarz, A. and Beck, M. (2019) The Benefits of Cotranslational Assembly: A Structural Perspective. *Trends Cell Biol.* 29, 791–803

268 Chang, P. *et al.* (2004) Localization of RNAs to the Mitochondrial Cloud in Xenopus Oocytes through Entrapment and Association with Endoplasmic Reticulum. *Mol. Biol. Cell* 15, 4669–4681

269 Forrest, K.M. and Gavis, E.R. (2003) Live Imaging of Endogenous RNA Reveals a Diffusion and Entrapment Mechanism for nanos mRNA Localization in Drosophila. *Curr. Biol.* 13, 1159–1168

270 Trovisco, V. *et al.* (2016) bicoid mRNA localises to the Drosophila oocyte anterior by random Dynein-mediated transport and anchoring. *Elife* 5, e17537

271 St Johnston, D. (2005) Moving messages: the intracellular localization of mRNAs. *Nat. Rev. Mol. Cell Biol.* 6, 363–75

272 Weil, T.T. *et al.* (2006) Localization of bicoid mRNA in Late Oocytes Is Maintained by Continual Active Transport. *Dev. Cell* 11, 251–262

273 Weil, T.T. *et al.* (2012) Drosophila patterning is established by differential association of mRNAs with P bodies. *Nat. Cell Biol.* 14, 1305–1313

274 Blower, M.D. (2013) Molecular Insights into Intracellular RNA Localization. In *International Review of Cell and Molecular Biology* 302pp. 1–39, Elsevier Inc.

275 Ding, D. *et al.* (1993) Dynamic Hsp83 RNA localization during Drosophila oogenesis and embryogenesis. *Mol. Cell. Biol.* 13, 3773–3781

276 Bashirullah, A. *et al.* (1999) Joint action of two RNA degradation pathways controls the timing of maternal transcript elimination at the midblastula transition in Drosophila melanogaster. *EMBO J.* 18, 2610–2620

277 Pyhtila, B. *et al.* (2008) Signal sequence- and translation-independent mRNA localization to the endoplasmic reticulum. *RNA* 14, 445–453

278 Hermesh, O. and Jansen, R.-P. (2013) Take the (RN)A-train: Localization of mRNA to the endoplasmic reticulum. *Biochim. Biophys. Acta - Mol. Cell Res.* 1833, 2519–2525

279 Liao, G. *et al.* (2011) An RNA-zipcode-independent mechanism that localizes Dia1 mRNA to the perinuclear ER through interactions between Dia1 nascent peptide and Rho-GTP. *J. Cell Sci.* 124, 589–599

280 Voigt, F. *et al.* (2017) Single-Molecule Quantification of Translation-Dependent Association of mRNAs with the Endoplasmic Reticulum. *Cell Rep.* 21, 3740–3753

281 Eliyahu, E. *et al.* (2012) The protein chaperone Ssa1 affects mRNA localization to the mitochondria. *FEBS Lett.* 586, 64–69

282 Eliyahu, E. *et al.* (2010) Tom20 Mediates Localization of mRNAs to Mitochondria in a Translation-Dependent Manner. *Mol. Cell. Biol.* 30, 284–294

283 Katsafanas, G.C. and Moss, B. (2019) Specific Anchoring and Local Translation of Poxviral ATI mRNA at Cytoplasmic Inclusion Bodies. *J. Virol.* 94,

284 Sepulveda, G. *et al.* (2018) Co-translational protein targeting facilitates centrosomal recruitment of PCNT during centrosome maturation in vertebrates. *Elife* 7, e34959

285 Kilchert, C. and Spang, A. (2011) Cotranslational transport of ABP140 mRNA to the distal pole of S. cerevisiae. *EMBO J.* 30, 3567–3580

286 Raab-Graham, K.F. *et al.* (2006) Activity- and mTOR-Dependent Suppression of Kv1.1 Channel mRNA Translation in Dendrites. *Science (80-.).* 314, 144–148

287 Mata, J. (2010) Genome-wide mapping of myosin protein-RNA networks suggests the existence of specialized protein production sites. *FASEB J.* 24, 479–484

288 Morisaki, T. *et al.* (2016) Real-time quantification of single RNA translation dynamics in living cells. *Science (80-.).* 352, 1425–1429

289 Pichon, X. *et al.* (2016) Visualization of single endogenous polysomes reveals the dynamics of translation in live human cells. *J. Cell Biol.* 214, 769–781

290 Eichel, C.A. *et al.* (2019) A microtranslatome coordinately regulates sodium and potassium currents in the human heart. *Elife* 8,

291 Panasenko, O.O. *et al.* (2019) Co-translational assembly of proteasome subunits in NOT1-containing assemblysomes. *Nat. Struct. Mol. Biol.* 26, 110–120

292 Kamenova, I. *et al.* (2019) Co-translational assembly of mammalian nuclear multisubunit complexes. *Nat. Commun.* 10, 1740

293 Willett, M. *et al.* (2013) mRNA encoding WAVE-Arp2/3-associated proteins is co-localized with foci of active protein synthesis at the leading edge of MRC5 fibroblasts during cell migration. *Biochem. J.* 452, 45–55

294 Zimmerman, S.B. and Trach, S.O. (1991) Estimation of macromolecule concentrations and excluded volume effects for the cytoplasm of Escherichia coli. *J. Mol. Biol.* 222, 599–620

295 Hardy, S.J. *et al.* (1988) Coordinated assembly of multisubunit proteins: oligomerization of bacterial enterotoxins in vivo and in vitro. *Proc. Natl. Acad. Sci.* 85, 7109–7113

296 Ellis, R.J. (2013) Assembly chaperones: a perspective. *Philos. Trans. R. Soc. B Biol. Sci.* 368, 20110398

297 Huizar, R.L. *et al.* (2018) A liquid-like organelle at the root of motile ciliopathy. *Elife* 7,

298 Klinge, S. and Woolford, J.L. (2019) Ribosome assembly coming into focus. *Nat. Rev. Mol. Cell Biol.* 20, 116–131

299 Zipser, D. (1963) Studies on the ribosome-bound β-galactosidase of Escherichia coli. *J. Mol. Biol.* 7, 739–751

300 Fulton, A.B. and L'Ecuyer, T. (1993) Cotranslational assembly of some cytoskeletal proteins: implications and prospects. *J. Cell Sci.* 105, 867–71

301 Lu, J. *et al.* (2001) T1−T1 Interactions Occur in ER Membranes while Nascent Kv Peptides Are Still Attached to Ribosomes. *Biochemistry* 40, 10934–10946

302 Deal, K. *et al.* (1994) The brain Kv1.1 potassium channel: in vitro and in vivo studies on subunit assembly and posttranslational processing. *J. Neurosci.* 14, 1666–1676

303 Duncan, C.D.S. and Mata, J. (2011) Widespread Cotranslational Formation of Protein Complexes. *PLoS Genet.* 7, e1002398

304 Shiber, A. *et al.* (2018) Cotranslational assembly of protein complexes in eukaryotes revealed by ribosome profiling. *Nature* 561, 268–272

305 Halbach, A. *et al.* (2009) Cotranslational assembly of the yeast SET1C histone methyltransferase complex. *EMBO J.* 28, 2959–70

306 Williams, N.K. and Dichtl, B. (2018) Co-translational control of protein complex formation: a fundamental pathway of cellular organization? *Biochem. Soc. Trans.* 46, 197–206

307 Sakahira, H. and Nagata, S. (2002) Co-translational Folding of Caspase-activated DNase with Hsp70, Hsp40, and Inhibitor of Caspase-activated DNase. *J. Biol. Chem.* 277, 3364–3370

308 Kassem, S. *et al.* (2017) Not5-dependent co-translational assembly of Ada2 and Spt20 is essential for functional integrity of SAGA. *Nucleic Acids Res.* 45, 1186–1199

309 Pal, K. *et al.* (2017) Structural Basis of TPR-Mediated Oligomerization and Activation of Oncogenic Fusion Kinases. *Structure* 25, 867-877.e3

310 McLaughlin, J.M. and Bratu, D.P. (2015) Drosophila melanogaster Oogenesis: An Overview. In *Methods in Molecular Biology* 1328pp. 1–20, Humana Press Inc.

311 Hudson, A.M. *et al.* (2008) Mononuclear muscle cells in Drosophila ovaries revealed by GFP protein traps. *Dev. Biol.* 314, 329–340

312 Huynh, J.-R. (2007) Fusome as a Cell-Cell Communication Channel of Drosophila Ovarian Cyst. In *Cell-Cell Channels* pp. 217–235, Springer New York

313 Bosco, G. and Orr-Weaver, T.L. (2002) The cell cycle during oogenesis and early embryogenesis in Drosophila. In *Advances in Developmental Biology and Biochemistry* 12pp. 107–154, Elsevier

314 Nordman, J. and Orr-Weaver, T.L. (2012) Regulation of DNA replication during development. *Development* 139, 455–464

315 Wu, X. *et al.* (2008) Drosophila follicle cells: Morphogenesis in an eggshell. *Semin. Cell Dev. Biol.* 19, 271–282

316 McCall, K. (2004) Eggs over easy: cell death in the Drosophila ovary. *Dev. Biol.* 274, 3–14

317 Avilés-Pagán, E.E. and Orr-Weaver, T.L. Activating embryonic development in Drosophila. , *Seminars in Cell and Developmental Biology*, 84. 01-Dec-(2018) , Elsevier Ltd, 100–110

318 Okada, E. and Waddington, C.H. (1959) The submicroscopic structure of the Drosophila egg. *J. Embryol. Exp. Morphol.* 7, 583–97

319 Rotem, A. *et al.* (2010) Importin B regulates the seeding of chromatin with initiation sites for nuclear pore assembly. *Mol. Biol. Cell* 20, 4031–4042

320 Harrison, M.M. and Eisen, M.B. (2015) Transcriptional Activation of the Zygotic Genome in Drosophila. In *Current Topics in Developmental Biology* 113pp. 85–112, Academic Press Inc.

321 Terasaki, M. *et al.* (2013) Stacked Endoplasmic Reticulum Sheets Are Connected by Helicoidal Membrane Motifs. *Cell* 154, 285–296

322 Austin, J.R. and Staehelin, L.A. (2011) Three-Dimensional Architecture of Grana and Stroma Thylakoids of Higher Plants as Determined by Electron Tomography. *Plant Physiol.* 155, 1601–1611

323 Clark, I. *et al.* (1994) Transient posterior localization of a kinesin fusion protein reflects anteroposterior polarity of the Drosophila oocyte. *Curr. Biol.* 4, 289–300

324 Ingolia, N.T. *et al.* (2011) Ribosome Profiling of Mouse Embryonic Stem Cells Reveals the Complexity and Dynamics of Mammalian Proteomes. *Cell* 147, 789–802

325 Yan, X. *et al.* (2016) Dynamics of Translation of Single mRNA Molecules In Vivo. *Cell* 165, 976–989

326 Lester, G.R. (1961) Contact angles of liquids at deformable solid surfaces. *J. Colloid Sci.* 16, 315–326

327 Bergeron-Sandoval, L.-P. *et al.* (2016) Mechanisms and Consequences of Macromolecular Phase Separation. *Cell* 165, 1067–1079

328 Alberti, S. (2017) Phase separation in biology. *Curr. Biol.* 27, R1097–R1102

329 Frasch, M. (1991) The maternally expressed Drosophila gene encoding the chromatin-binding protein BJ1 is a homolog of the vertebrate gene Regulator of Chromatin Condensation, RCC1. *EMBO J.* 10, 1225–36

330 Brand, A.H. and Perrimon, N. (1993) Targeted gene expression as a means of altering cell fates and generating dominant phenotypes. *Development* 118, 401–15

331 Petrella, L.N. *et al.* (2007) The Ovhts polyprotein is cleaved to produce fusome and ring canal proteins required for Drosophila oogenesis. *Development* 134, 703–712

332 Hondele, M. *et al.* (2019) DEAD-box ATPases are global regulators of phase-separated organelles. *Nature* 573, 144–148

333 Rai, A.K. *et al.* (2018) Kinase-controlled phase transition of membraneless organelles in mitosis. *Nature* 559, 211–216

334 Cordes, V.C. *et al.* (1996) Cytoplasmic annulate lamellae in cultured cells: composition, distribution, and mitotic behavior. *Cell Tissue Res.* 284, 177–191

335 Kessel, R.G. (1989) Fibrogranular Material , Annulate Lamellae and Microtubules During Spermiogenesis in Drosophila melanogaster. *Acta Zool.* 70, 95–103

336 Kessel, R.G. (1985) The Relationships of Annulate Lamellae , Fibrogranular Bodies , Nucleolus , and Polyribosomes during Spermatogenesis in Drosophila melanogaster. *J. Ultrasructure Res.* 191, 183–191

337 Volland, S. *et al.* (2015) Three-dimensional organization of nascent rod outer segment disk membranes. *Proc. Natl. Acad. Sci. U. S. A.* 112, 14870–14875

338 Lehmann, R. (2016) Germ Plasm Biogenesis-An Oskar-Centric Perspective. In *Current Topics in*

Developmental Biology 116pp. 679–707, Academic Press Inc.

339 Pestka, S. (1971) Inhibitors of Ribosome Functions. *Annu. Rev. Microbiol.* 25, 487–562

340 Enarson, P. *et al.* (1998) Amino-terminal sequences that direct nucleoporin Nup153 to the inner surface of the nuclear envelope. *Chromosoma* 107, 228–236

341 Wells, J.N. *et al.* (2015) Co-translational assembly of protein complexes. *Biochem. Soc. Trans.* 43, 1221–1226

342 Liu, F. *et al.* (2016) Cotranslational association of mRNA encoding subunits of heteromeric ion channels. *Proc. Natl. Acad. Sci.* 113, 4859–4864

343 Kassube, S.A. *et al.* (2012) Crystal structure of the N-terminal domain of Nup358/RanBP2. *J. Mol. Biol.* 423, 752–765

344 Cingolani, G. *et al.* Structure of importin-β bound to the IBB domain of importin-α. , *Nature*, 399. 20-May-(1999) , Nature Publishing Group, 221–229

345 Lowe, A.R. *et al.* (2015) Importin-β modulates the permeability of the nuclear pore complex in a Ran-dependent manner. *Elife* 2015, 1–24

346 Kapinos, L.E. *et al.* (2017) Karyopherins regulate nuclear pore complex barrier and transport function. *J. Cell Biol.* 216, 3609–3624

347 Gaspar, I. (2011) Microtubule-based motor-mediated mRNA localization in Drosophila oocytes and embryos. *Biochem. Soc. Trans.* 39, 1197–1201

348 Takano, Y. and Sakanishi, A. (1988) Effects of viscoelasticity of cytoplasm on the complex viscosity of red blood cell suspensions. *Biorheology* 25, 123–128

349 Hu, J. *et al.* (2017) Size- and speed-dependent mechanical behavior in living mammalian cytoplasm. *Proc. Natl. Acad. Sci.* 114, 9529–9534

350 Konishi, H.A. and Yoshimura, S.H. (2020) Interactions between non-structured domains of FG- and non-FG-nucleoporins coordinate the ordered assembly of the nuclear pore complex in mitosis. *FASEB J.* 34, 1532–1545

351 Hampoelz, B. *et al.* (2019) Nuclear Pores Assemble from Nucleoporin Condensates During Oogenesis. *Cell* 179, 671-686.e17

352 Zeng, M. *et al.* (2018) Reconstituted Postsynaptic Density as a Molecular Platform for Understanding Synapse Formation and Plasticity. *Cell* 174, 1172-1187.e16

353 Wu, X. *et al.* (2019) RIM and RIM-BP Form Presynaptic Active-Zone-like Condensates via Phase Separation. *Mol. Cell* 0,

354 Wippich, F. *et al.* (2013) Dual Specificity Kinase DYRK3 Couples Stress Granule Condensation/Dissolution to mTORC1 Signaling. *Cell* 152, 791–805

355 Ando, D. *et al.* (2017) Cooperative Interactions between Different Classes of Disordered Proteins Play a Functional Role in the Nuclear Pore Complex of Baker's Yeast. *PLoS One* 12, e0169455

356 Sakuma, S. and D'Angelo, M.A. (2017) The roles of the nuclear pore complex in cellular dysfunction, aging and disease. *Semin. Cell Dev. Biol.* 68, 72–84

357 Katsani, K.R. *et al.* (2008) In vivo dynamics of Drosophila nuclear envelope components. *Mol. Biol. Cell* 19, 3652–66

358 Mendjan, S. *et al.* (2006) Nuclear Pore Components Are Involved in the Transcriptional

Regulation of Dosage Compensation in Drosophila. *Mol. Cell* 21, 811–823

359 Roth, P. *et al.* (2003) The Drosophila nucleoporin DNup88 localizes DNup214 and CRM1 on the nuclear envelope and attenuates NES-mediated nuclear export. *J. Cell Biol.* 163, 701–706

360 Gratz, S.J. *et al.* Genome engineering of Drosophila with the CRISPR RNA-guided Cas9 nuclease. , *Genetics*, 194. 01-Aug-(2013) , 1029–1035

361 Mastronarde, D.N. (2003) SerialEM: A Program for Automated Tilt Series Acquisition on Tecnai Microscopes Using Prediction of Specimen Position. *Microsc. Microanal.* 9, 1182–1183

362 Kremer, J.R. *et al.* (1996) Computer visualization of three-dimensional image data using IMOD. *J. Struct. Biol.* DOI: 10.1006/jsbi.1996.0013

363 Paul-Gilloteaux, P. *et al.* (2017) eC-CLEM: flexible multidimensional registration software for correlative microscopies. *Nat. Methods* 14, 102–103

364 de Chaumont, F. *et al.* (2012) Icy: an open bioimage informatics platform for extended reproducible research. *Nat. Methods* 9, 690–696

365 Arganda-Carreras, I. *et al.* (2017) Trainable Weka Segmentation: a machine learning tool for microscopy pixel classification. *Bioinformatics* 33, 2424–2426

366 Schindelin, J. *et al.* (2012) Fiji: an open-source platform for biological-image analysis. *Nat. Methods* 9, 676–682

367 Krzic, U. *et al.* (2012) Multiview light-sheet microscope for rapid in toto imaging. *Nat. Methods* 9, 730–733

368 Medeiros, G. De *et al.* (2015) Confocal multiview light-sheet microscopy. *Nat. Commun.* 6, 8881

369 Thévenaz, P. *et al.* (1998) A pyramid approach to subpixel registration based on intensity. *IEEE Trans. Image Process.* 7, 27–41

370 Sommer, C. *et al.* (2011) , Ilastik: Interactive learning and segmentation toolkit. , in *Proceedings - International Symposium on Biomedical Imaging*

371 Legland, D. *et al.* (2016) MorphoLibJ: Integrated library and plugins for mathematical morphology with ImageJ. *Bioinformatics* DOI: 10.1093/bioinformatics/btw413

372 Gáspár, I. *et al.* (2018) Terminal Deoxynucleotidyl Transferase Mediated Production of Labeled Probes for Single-molecule FISH or RNA Capture. *BIO-PROTOCOL* 8,

373 Wickham, H. (2009) Introduction. In *ggplot2* pp. 1–7, Springer New York